Julius-Maximilians-
UNIVERSITÄT
WÜRZBURG

UNIVERSITÄT WÜRZBURG
PHYSIKALISCHES INSTITUT
epVI

Field Dependence of Charge Carrier Generation in Organic Bulk Heterojunction Solar Cells

Dissertation zur Erlangung des
naturwissenschaftlichen Doktorgrades
der Julius-Maximilians-Universität Würzburg

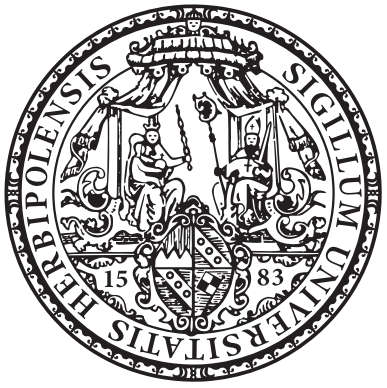

vorgelegt von

Julia Kern

aus Würzburg

Würzburg 2013

Eingereicht am: 30.10.2013
bei der Fakultät für Physik und Astronomie

1. Gutachter: Prof. Dr. Vladimir Dyakonov
2. Gutachter: Prof. Dr. Jean Geurts
der Dissertation.

1. Prüfer: Prof. Dr. Vladimir Dyakonov
2. Prüfer: Prof. Dr. Jean Geurts
3. Prüfer: Prof. Dr. Reiner Kümmel
im Promotionskolloquium.

Tag des Promotionskolloquiums: 12.02.2014

Doktorurkunde ausgehändigt am:

I'D PUT MY MONEY ON THE SUN AND SOLAR ENERGY.
WHAT A SOURCE OF POWER! I HOPE WE DON'T HAVE TO
WAIT 'TIL OIL AND COAL RUN OUT BEFORE WE TACKLE THAT.

Thomas Alva Edison (1847-1931)

Abstract

In the field of organic photovoltaics, one of the most intensely researched topics to date is the charge carrier photogeneration in organic bulk heterojunction solar cells whose thorough understanding is crucial for achieving higher power conversion efficiencies. In particular, the mechanism of singlet exciton dissociation at the polymer–fullerene interface is still controversially debated.

This work addresses the dissociation pathway via relaxed charge transfer states (CTS) by investigating its field dependence for reference material systems consisting of MDMO-PPV and one of the fullerene derivatives $PC_{61}BM$, bisPCBM and $PC_{71}BM$. Field dependent photoluminescence (PL(F)) and transient absorption (TA(F)) measurements give insight into the recombination of charge transfer excitons (CTE) and the generation of polarons, respectively. Optically detected magnetic resonance and atomic force microscopy are used to characterize the morphology of the samples.

The comparison of the experimental field dependent exciton recombination recorded by PL(F) and the theoretical exciton dissociation probability given by the Onsager–Braun model yields the exciton binding energy as one of the key parameters determining the dissociation efficiency. The binding energies of both the singlet exciton in neat MDMO-PPV and the CTE in MDMO-PPV:$PC_{61}BM$ 1:1 are extracted, the latter turning out to be significantly reduced with respect to the one of the singlet exciton.

Based on these results, the field dependence of CTE dissociation is evaluated for MDMO-PPV:$PC_{61}BM$ blends with varying fullerene loads by PL(F) and TA(F). For higher $PC_{61}BM$ contents, the CTE binding energies decrease notably. This behavior is ascribed to a larger effective dielectric constant for well-intermixed blends and to an interplay between dielectric constant and CTE delocalization length for phase separated morphologies, emphasizing the importance of high dielectric constants for the charge carrier photogeneration process.

Finally, the CTE binding energies are determined for MDMO-PPV blends with different fullerene derivatives, focusing on the influence of the acceptor LUMO energy. Here, the experimental results suggest the latter having no or at least no significant impact on the binding energy of the CTE. Variations of this binding energy are rather related to different trap levels in the acceptors which seem to be involved in CTS formation.

Kurzfassung

Einer der aktuellen Forschungsschwerpunkte im Bereich der organischen Photovoltaik ist die Ladungsträgergenerierung in „Bulk Heterojunction-Solarzellen“, deren Verständnis für das Erreichen höherer Wirkungsgrade essentiell ist. In diesem Zusammenhang wird derzeit vor allem der Dissoziationsmechanismus der Singulett-Exzitonen an der Donator–Akzeptor-Grenzfläche kontrovers diskutiert.
Die vorliegende Arbeit adressiert die Dissoziation über relaxierte Ladungstransferzustände (CTS) durch die Untersuchung der Feldabhängigkeit des Prozesses für Referenzsysteme aus MDMO-PPV und den Fullerenderivaten $PC_{61}BM$, bisPCBM sowie $PC_{71}BM$. Feldabhängige Photolumineszenz (PL(F)) und transiente Absorption (TA(F)) geben Aufschluss über Rekombination der Ladungstransfer-Exzitonen (CTE) bzw. Polaronengenerierung, während die Morphologie der Proben durch optisch detektierte Magnetresonanz und Rasterkraftmikroskopie charakterisiert wird.
Durch den Vergleich der experimentellen feldabhängigen Exzitonenrekombination mit der theoretischen Dissoziationswahrscheinlichkeit nach dem Onsager–Braun-Modell lässt sich die Bindungsenergie der Exzitonen ermitteln, welche die Dissoziationseffizienz entscheidend beeinflusst. Diese Bindungsenergie wird sowohl für das Singulett-Exziton in reinem MDMO-PPV als auch für das CTE in MDMO-PPV:$PC_{61}BM$ 1:1 bestimmt, wobei letztere deutlich geringer als die des Singulett-Exzitons ist.
Ausgehend von diesen Ergebnissen wird die Feldabhängigkeit der CTE-Dissoziation für MDMO-PPV:$PC_{61}BM$-Gemische mit unterschiedlichen Fullerenanteilen durch PL(F) und TA(F) untersucht. Für höhere $PC_{61}BM$-Konzentrationen nimmt die CTE-Bindungsenergie merklich ab. Dieses Verhalten ist für gut durchmischte Systeme einer höheren dielektrischen Konstante und für phasenseparierte Systeme dem Zusammenspiel zwischen Dielektrizitätskonstante und Delokalisation der CTE zuzuschreiben.
Schließlich werden die CTE-Bindungsenergien für Gemische aus MDMO-PPV und unterschiedlichen Fullerenderivaten bestimmt, wobei der Einfluss des LUMO-Niveaus der Akzeptoren im Fokus steht. Dieses scheint jedoch keine oder nur eine geringe Bedeutung für die CTE-Bindungsenergie zu besitzen. Die beobachteten Variationen der Bindungsenergie sind vielmehr auf die Fallenzustände der Akzeptoren zurückzuführen, welche offenbar an der Ausbildung der CTS beteiligt sind.

Contents

1 Introduction

Living in an age characterized by the rising awareness of the tension between the increasing global energy demand on the one hand and the limitations and tremendous risks of conventional energy production on the other hand, the need for sustainable, environmentally friendly energy sources is undisputed. Thus, it is not surprising that more than 100 countries worldwide promote the development of renewable energy technologies with support policies such as feed-in tariffs, renewable portfolio standards or quota systems [1]. In Germany, a feed-in tariff was already introduced in 1991 [2], being restructured as the German Renewable Energy Act ("Erneuerbare-Energien-Gesetz", EEG) in 2000 [3] which led to a boost of the renewable energy market. In the last few years, one of the biggest beneficiaries of the German EEG was the photovoltaics (PV) sector: In 2012 alone, plants and modules with a capacity of 7.6 GW were newly installed, cumulating in a total capacity of 32.6 GW. The electricity generation via PV was increased by 45 % with respect to the previous year, amounting to 28 billion kWh or 4.7 % of the German gross electricity consumption [4]. As a recent reaction to the observed explosive growth of PV installations, the PV feed-in tariffs were reduced by a 2012 amendment to the EEG [5] — a measure which indicates the approaching maturity of the PV market and the expectation of its future subsidiary-free growth.

Coming to speak of the actual technology behind this story of success, the working principle of solar cells is based on the photovoltaic effect which was first observed by Alexandre Edmond Becquerel in 1892 [6]. If a semiconducting material is irradiated with e.g. sunlight, the absorption of photons leads to the excitation of electrons from valence to conduction band and the subsequent generation of a photocurrent. This process was first employed for the fabrication of a crystalline silicon solar cell by Daryl Chapin, Calvin Fuller and Gerald Pearson in the Bell Laboratories in 1954 [7], reaching a power conversion efficiency of $\eta = 6$ %. Since then, the efficiency of silicon based photovoltaics has steadily improved, with state-of-the-art monocrystalline silicon (c-Si) cells featuring values of up to 25 % [8] which are already close to the theoretical maximum given by the Shockley–Queisser limit [9] of roughly 30 % for this type of solar cells. However, the production of these well-performing c-Si cells involves high

temperature processing steps which increase the overall production costs significantly. Multicrystalline silicon (mc-Si) solar cells are less expensive in the production process, but also less efficient, with record values of $\eta \approx 20$ % being reached to date [8]. Besides, these two market-dominating technologies require active layer thicknesses of about 180 µm [10], leading to a high material demand which also increases costs. As an alternative approach, thin film technologies such as copper indium gallium (di)selenide (CIGS) cells ($\eta \approx 20$ % [8]), CdTe cells ($\eta \approx 18$ % [8]) or amorphous (a-Si) and nanocrystalline (nc-Si) silicon cells ($\eta \approx 10$ % [8]) have entered the market.

Apart from these inorganic thin film technologies, solar cells fabricated from organic semiconductors have recently gained a lot of attention in the photovoltaics community, indicated by an increase of new publications on the topic from ~ 80 in 2007 to ~ 550 in 2012 [11]. This so-called third generation photovoltaics technology is based on the discovery of conductive polymers in 1977 [12] and — over the last couple of years — has strongly profited from the expertise of the related but already more established sectors of organic light emitting diodes (OLEDs) and organic field effect transistors (OFETs). The major advantage of organic photovoltaics (OPV) with respect to conventional photovoltaics is given by the facile processing of the cells via roll-to-roll printing or vacuum deposition techniques which do not require high temperatures. Upscaling of the process would allow for the production of large areas on short timescales, with volumes of about 10000 m^2/h [13]. Such a fast and cheap fabrication offers the potential to compete with the steadily decreasing costs of silicon based modules which are currently of the order of 1 €/Wp (Watt-peak) [10, 14], making OPV suitable for large-scale on-grid energy generation as well as for off-grid applications in emerging markets which only require a basic supply of energy [15]. Yet, OPV is suffering from mainly two drawbacks which are detrimental to the above mentioned applications. First, efficiencies are still trailing behind, with record efficiencies on a laboratory scale just hitting the 12 % mark [16]. Second, the degradation of the organic semiconductors due to moisture and oxygen leads to short lifetimes of the solar cells. Both issues, however, play a less important role for applications of OPV which focus on the unique features of organic semiconductors. For instance, organic solar cells can be processed on flexible substrates, allowing for e.g. easily storable mobile modules for outdoor applications or solar cells printed on bags or backpacks. Moreover, organic semiconductors are available in a large variety of colors and can be tuned to be semi- or even fully transparent in the visible range of the optical spectrum, offering unprecedented freedom of design for e.g. building-integrated PV on windows or facades. Since the latter scenarios do not necessarily demand high efficiencies or standardized module lifetimes but rather depend on a long-term color stability of the utilized materials, they are currently regarded

as a future key application of OPV for which costs will be calculated in €/m^2 rather than in €/Wp.

Nevertheless, the enhancement of power conversion efficiencies is still the primary striving of OPV research today. Reaching new, competitive record efficiencies is not viable without carefully chosen design rules for the synthesis of high-performing organic semiconductors. In turn, such design rules require a complete and thorough understanding of the underlying physical processes. In this context, the presented thesis aims at gaining a deeper insight into photoinduced charge carrier generation in organic polymer–fullerene bulk heterojunction (BHJ) solar cells, being one of the few processes which is not understood in every detail yet. Most importantly, the dissociation pathways of the photogenerated singlet exciton to free charge carriers — be it via an intermediate charge transfer exciton (CTE) or via direct dissociation — is still under controversial discussion. Here, the dissociation route via relaxed CTE is investigated mainly by means of field dependent photoluminescence (PL(F)) on OPV reference material systems consisting of the well-known polymer poly[2-methoxy-5-(3',7'-dimethyloctyloxy)-1,4-phenylenevinylene] (MDMO-PPV) in combination with various fullerene derivatives such as [6,6]-phenyl-C61 butyric acid methyl ester ($PC_{61}BM$). In this way, information on the magnitude and the relevance of the CTE binding energy as one of the crucial parameters governing singlet exciton dissociation is extracted. Starting with a brief overview of the fundamental properties of organic semiconductors and the working principles of organic BHJ solar cells in Chapter 2, the currently debated photophysical models of charge carrier generation are introduced in Chapter 3. Also, the basics of charge transfer states (CTS) are presented alongside a short review on the Onsager–Braun model used for describing the field dependence of charge carrier photogeneration. Chapter 4 lists the utilized organic materials and the different processing steps for device fabrication while Chapter 5 is dedicated to the description of the applied experimental techniques. The first experimental results on the binding energy of the CTE in MDMO-PPV:$PC_{61}BM$ 1:1 in comparison to the one of the singlet exciton in neat MDMO-PPV are presented in Chapter 6. Based on these findings, the role of blend morphology and dielectric constant on field dependent charge carrier photogeneration is investigated in Chapter 7 by systematically changing the polymer-to-fullerene ratio in the active layer blends. Finally, Chapter 8 elucidates the influence of acceptor LUMO levels and trap states on the CTE binding energy.

2 Organic Photovoltaics

In this chapter, some of the basic properties of organic semiconductors are introduced, representing the very foundations of the feasibility of organic photovoltaics. Moreover, the working principles of the bulk heterojunction solar cells used in this work are described. Naturally, the scope of this thesis only allows for giving a brief overview on these extensive topics. For a more in-depth discussion, review articles such as Deibel et al. [13] and Brabec et al. [17] or textbooks on this subject [18, 19] may be consulted. The listed publications also serve as the basis for this chapter.

2.1 Organic Semiconductors

Organic semiconductors are carbon compounds that can mainly be divided into the two classes of small molecules (e.g. copper phthalocyanine) and conjugated polymers (e.g. poly(p-phenylene vinylene), PPV). A major difference between these classes is their processibility: While small molecules are commonly deposited from the gas phase by sublimation or evaporation [18], conjugated polymers are processed from solution by spin-coating or role-to-role printing. The different processing techniques result in mostly well-ordered, crystalline films in the case of the small molecules and comparatively disordered, amorphous films in the case of the conjugated polymers. Yet, for both classes, their semiconducting character is based on a π-conjugated system with alternating single and double bonds between the carbon atoms and a delocalized π-electron cloud. The conjugation is related to the sp^2-hybridization of the carbon atoms. In its ground state, a free carbon atom has an electronic configuration of $1s^2 2s^2 2p^2$. Upon the bonding of two carbon atoms, one 2s- and the $2p_x$- and $2p_y$-orbitals build out three degenerate sp^2-orbitals with a coplanar orientation, separated by an angle of 120°. While these hybrid orbitals form localized σ-bonds constituting the backbone of the molecules, the p_z-orbitals which are oriented perpendicular to the hybrid orbital plane develop weak π-bonds (see Figure 2.1). The corresponding delocalized electrons can move quasi-freely along the molecule and are responsible for the conductivity in organic semiconductors.

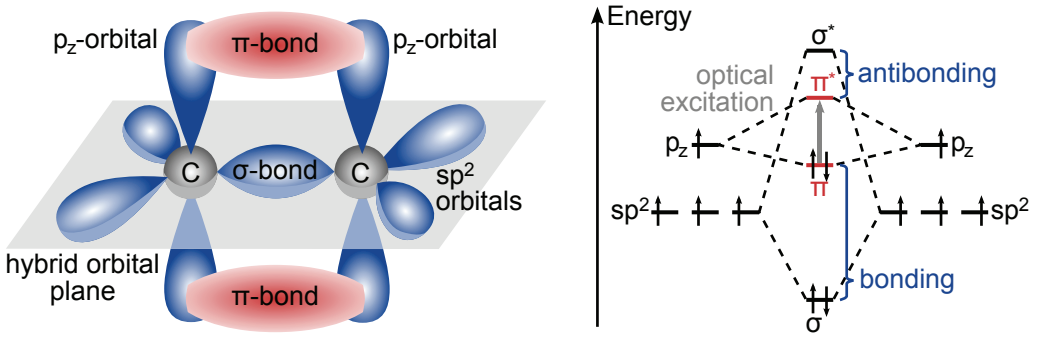

Figure 2.1: sp^2-hybridization and energy levels of a π-conjugated molecule. The left viewgraph shows the formation of σ- and π-bonds between two neighboring carbon atoms. The corresponding energy diagram on the right side illustrates the energetics of the atomic orbitals of sp^2-hybridized carbon and the splitting of the orbitals in bonding ( ) and antibonding (*) σ- and π-orbitals. The lowest optical excitation takes place between the π- and the π*-orbital (adopted from [18] and [20]).

In the conjugated system, the alternation between strong single and weak double bonds goes hand in hand with an alternation of the distances between the carbon atoms. Due to the resulting Peierls instability [21], the p$_z$-orbitals of the interacting carbon atoms split into bonding π- and antibonding π*-orbitals (see Figure 2.1). The π-orbitals correspond to the HOMO (i.e., the highest occupied molecular orbital) and the π*-orbitals to the LUMO (i.e., the lowest unoccupied molecular orbital) of the respective organic semiconductor. Since the π-bonding is significantly weaker than the σ-bonding, the lowest electronic excitations of the conjugated molecules are the π–π*-transitions with excitation energies in the range of 1 eV to 3 eV. This HOMO–LUMO bandgap (also referred to as optical bandgap $E_{g,opt}$) is controlled by the degree of conjugation and leads to the molecules absorbing and emitting in the visible, near infrared and near ultraviolet spectral region, making them suitable for photovoltaic applications.

In the presented work, the focus was set on photovoltaic devices deploying conjugated polymers. Polymers are long chains consisting of repeating units called monomers. For instance, the most simple linear conjugated polymer polyacetylene is set up from repeating C–H monomer units which can be expressed as (CH)$_x$. The conjugation length of such polymers which is crucial for the electronic delocalization is generally limited by structural or chemical defects. Accordingly, for a certain polymer, the conjugation lengths of different molecules are not constant, leading to an energetic distribution of the HOMO and LUMO levels and a changing local environment. While the carbon atoms in a polymer chain are bound covalently by sharing electrons as stated above, the intermolecular bonding of multiple polymer chains is achieved by van der Waals forces. Thus, the electronic interactions between neighboring chains are weak com-

pared to inorganic semiconductors such as Si or GaAs. This not only leads to different mechanical and thermodynamic properties (e.g. reduced hardnesses and melting points), but also to a significantly weaker delocalization of the electronic wavefunctions between adjacent chains.

Owing to this weak delocalization, optical excitations of the polymers are usually localized on one molecule. Such so-called Frenkel excitons, which can be envisioned as electrically neutral, coulombically bound electron–hole pairs in an approximative approach, require an excitation energy which is smaller than the one needed to excite a separated electron–hole pair. Thus, the primary photoexcitations in conjugated polymers are singlet excitons (i.e., with a total spin of $S = 0$) which can be roughly described as the electron residing in the LUMO and the hole in the HOMO level. This corresponds to an excitation of the singlet exciton ground state S_0 to the first excited state S_1 as shown in Figure 2.2. Excitations to higher excited states are also possible, but neglected here for reasons of simplicity.

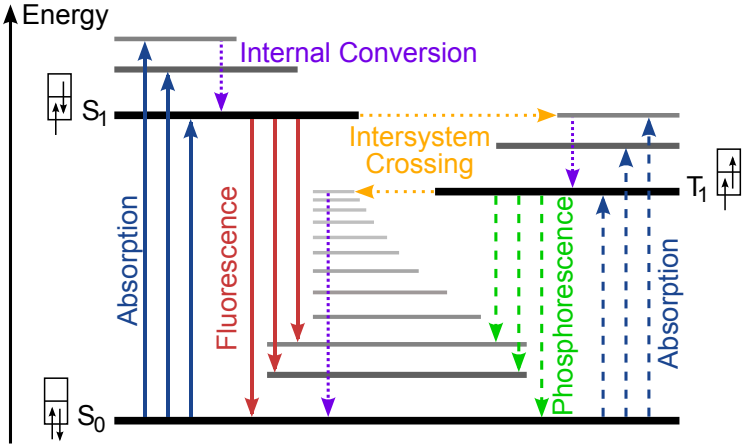

Figure 2.2: Simplified energy level scheme of a conjugated polymer. The processes most relevant for this thesis are the photoexcitation from the ground state of the singlet exciton S_0 to the first excited state S_1 and the subsequent internal conversion and radiative decay back to the ground state. The excited singlet exciton may alternatively undergo intersystem crossing to the triplet state T_1 (adopted from [18]).

If higher vibronic levels are excited, they relax by a non-radiative process called internal conversion within a pico- to femtosecond-timeframe [22] to the S_1 state. This state possesses typical lifetimes in the nanosecond region and can decay radiatively by emitting fluorescence. Alternatively, the exciton can undergo intersystem crossing from the S_1 state to the lower lying triplet state T_1 which is characterized by a total spin of $S = 1$. As the transition of the triplet to the ground state is spin-forbidden, triplet excitons experience comparatively long lifetimes of up to milliseconds. For some organic semiconductors used for OLED applications, triplet absorption from the ground state and a subsequent radiative decay called phosphorescence can be observed which

— like the fluorescence — is a form of photoluminescence (PL). However, since these processes are not relevant for the presented work, the term "photoluminescence" is used to describe the fluorescence from singlet excitons throughout this thesis.

2.2 Organic Bulk Heterojunction Solar Cells

As mentioned above, the singlet excitons are usually localized on one molecule, associated with a comparatively short electron–hole distance. In addition to this, the dielectric constant of organic semiconductors is significantly lower ($\epsilon_r \approx 3-4$) than the one of their inorganic counterparts ($\epsilon_r \geq 10$) [23]. These conditions lead to considerable singlet exciton binding energies of 0.5 eV to 1 eV which exceed the thermal energy at room temperature of about 25 meV by far. Thus, in a photovoltaic device, this binding energy has to be overcome by an additional driving force in order to generate free charge carriers.

2.2.1 The Bulk Heterojunction Concept

As a result of the strong Frenkel exciton binding energies, the first organic solar cells, which possessed a single active layer placed between two electrodes with different work functions, displayed poor power conversion efficiencies of less than 1 % [24]. In such devices, exciton dissociation mainly takes place at the contacts [23]. Starting in the 1980s [25], efficiencies were improved by coating the active layer with a second, more electronegative organic semiconductor, both materials usually belonging to the class of small molecules. In this second approach, a charge transfer (CT) of the electron from the LUMO of the light-absorber to the lower lying LUMO of the electron accepting material takes place. This CT process between donor and acceptor provides the energy required for exciton dissociation. However, a major drawback of this concept is the relatively short diffusion length of excitons in organic semiconductors of approximately 10 nm. This value is significantly smaller than the absorption length of typical donor materials which is about 100 nm and — in order to ensure maximal absorption of the incident light — sets the limit for the active layer thickness. In this picture, only about 10 % of the generated excitons can reach the heterointerface between donor and acceptor within their lifetime and be separated. The remaining 90 % are bound to recombine, therefore being lost to photocurrent generation and limiting the device efficiency. This issue was resolved in the 1990s by mixing the donor and acceptor material, setting a milestone on the way to better device performances. In the so-called bulk heterojunction (BHJ) solar cell concept [26], the crucial donor–acceptor

interface is no longer planar, but spatially distributed over the whole bulk of the active layer (see Figure 2.3).

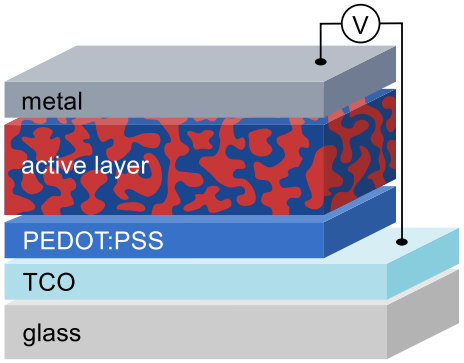

Figure 2.3: Typical device structure of an organic bulk heterojunction solar cell. The active layer, consisting of an intermixed donor–acceptor blend, is sandwiched in between two electrodes. A metal layer is deployed as cathode while a transparent conductive oxide (TCO), covering a glass substrate, serves as anode. Illumination of the photoactive blend is achieved through the glass/TCO layers. On top of the TCO, a thin film of poly(3,4-ethylenedioxythiophene):poly(styrenesulfonate) (PEDOT:PSS) is usually deposited as electron-blocking layer and in order to smooth the rough TCO surface, helping to avoid shunts.

The benefits of such an interpenetrated donor–acceptor network are obvious: While the active layer thickness can be chosen to match the absorption length, the singlet excitons which are generated in the donor material throughout the bulk generally encounter an interface within their diffusion length if the device morphology is designed accordingly. Thus, almost all photogenerated excitons can be separated, constituting the prerequisite for high internal quantum efficiencies close to unity. For the polymer–fullerene BHJ cells investigated in this thesis, the intermixing of donor and acceptor is usually accomplished by spin-casting a blend of the respective organic semiconductors, with a wide range of suitable materials being available. Commonly employed donor polymers vary from established OPV work horses such as PPV or poly(3-hexylthiophene) (P3HT) to high-performing low-bandgap copolymers [27, 28, 29], offering the advantage of extended absorption spectra. As for the acceptors, the highest efficiencies are usually achieved with soluble derivatives of the buckminsterfullerene C_{60} like $PC_{61}BM$ or a close relative, the [6,6]-phenyl-C71 butyric acid methyl ester ($PC_{71}BM$). More detailed information on the materials chosen for the presented work can be found in Chapter 4. For a given donor–acceptor combination, the device performance can be optimized by e.g. varying the blend ratio. For example, the ideal blend ratio was found to be 1:4 for MDMO-PPV and $PC_{61}BM$ [30, 31] while solar cells made from P3HT and $PC_{61}BM$ yield highest efficiencies for blends of about 1:1 [32]. The optimal blend ratio as well as the overall device efficiency are closely related to the

underlying nanomorphology of the bulk [30]. Only considering the process of exciton dissociation, a small domain size of the phase separated donor and acceptor materials would be desirable. Yet, sufficient percolation pathways for the transport of charge carriers to the electrodes have to be provided, demanding a rather coarse phase segregation. Hence, a tradeoff between the two basic requirements has to be made for each individual material combination. The morphology can be controlled by the choice of solvents [30], thermal and voltage annealing of the active layer [33] or the use of additives [28, 34]. For instance, a rise in efficiency from 0.4 % to 3.5 % by post-production treatment was reported for P3HT:PC_{61}BM solar cells [33].

2.2.2 Working Principles

The basic purpose of any solar cell is the conversion of solar radiation into electrical energy by the generation of a photocurrent. For an organic polymer–fullerene BHJ solar cell, the main steps on the road to this objective are presented in Figure 2.4 from a device physical and from an energetic point of view. They consist of singlet exciton generation (i) and diffusion to the interface (ii), CT (iii) and charge carrier pair dissociation (iv), subsequent transport of the charge carriers (v) and, finally, their extraction at the contacts (vi).

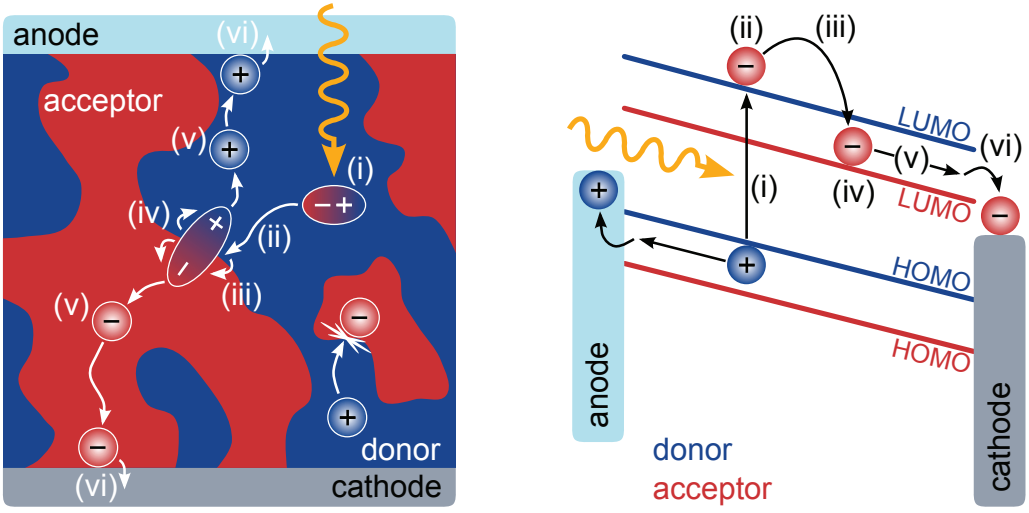

Figure 2.4: The path to photocurrent generation in an organic BHJ cell from a device physical (left side) and an energetic (right side) perspective. Through the absorption of incident light, a singlet exciton is generated (i). Following the diffusion of the exciton to the donor–acceptor interface (ii), a CT of the electron to the acceptor material takes place (iii). After the splitting of the charge carrier pair (iv), the charge carriers are transported in their respective media (v) to the contacts where they can be extracted (vi) and contribute to the photocurrent (modified from [13] and [35]).

(i) Singlet Exciton Generation by Light Absorption

In organic BHJ solar cells, the absorption of incident light mainly takes place in the donor material, i.e., in the conjugated polymer domains. While the polymers used for photovoltaic applications possess high absorption coefficients of more than 10^7 m^{-1}, their spectral absorption range is usually limited to the visible optical spectrum [36, 37, 38] if no specially designed polymers offering a spectrally extended absorption are used [27, 28, 29, 39, 40]. It should be noted that light is also absorbed to a lesser degree by the fullerene derivatives used as acceptors. Since this process also contributes to the photovoltaic performance [41, 42], the choice of an acceptor with a wide absorption spectrum such as $PC_{71}BM$ is favorable [41, 43]. However, in order to enable a simplified reasoning, the following descriptions are focused on photoexcitation in the donor. Upon light absorption, strongly bound singlet excitons as the primary photoexcitations in organic photovoltaics are generated. These Frenkel excitons are usually situated on one polymer chain segment and are therefore also termed intrachain excitons [44]. As already mentioned, the considerable binding energy of these neutral excitations demands an electronegative acceptor material for exciton splitting.

(ii) Diffusion to the Donor–Acceptor Interface

In order to be separated, the exciton has to diffuse towards the donor–acceptor interface within its lifetime [45, 46]. In the case that the exciton is generated in a distance from the heterojunction which is greater than its diffusion length, it recombines in a generally radiative process and is lost for photocurrent generation. The diffusion length of e.g. P3HT has been determined as 4 nm to 8 nm [47, 48] while for MDMO-PPV, a value of 12 nm was reported [49]. As the exciton approaches the interface, it is influenced by the change of environment as compared to the bulk which may result in a slightly red-shifted PL emission [50, 51, 52].

(iii) Charge Transfer of the Electron

Upon reaching the donor–acceptor interface, the singlet exciton can transfer the electron from the donor host material to the electronegative acceptor in an ultrafast process of the order of tens of femtoseconds [53, 54]. The fast timescale of the CT makes it more efficient than the slower competing loss mechanisms such as PL or intersystem crossing from the singlet to the triplet state. However, the exciton only dissociates when the corresponding energy gain is larger than its binding energy, i.e., in the case that its energy exceeds the one of the electron–hole pair after the CT process which is known under the expressions polaron pair, charge transfer complex or charge transfer

exciton in literature [52, 55, 56, 57]. As for the nomenclature, a polaron is defined as the entity of a charge and the induced distortion of its surroundings. In organic semiconductors, a charge which is situated on a molecule can cause a deformation of the latter, resulting in a lower mobility and an aggravated charge transport. Consequently, a polaron pair consists of a positive and a negative polaron which are coulombically bound. This polaron pair can either reside on a single molecule, similar to a singlet exciton but with a larger electron–hole distance and thus a reduced binding energy, or on different molecules in the blend, with the electron sitting on the donor and the hole on the acceptor material. Thus, polaron pairs can be regarded as intermediates between excitons and free polarons [52, 58, 59]. In order to distinguish between the different types of polaron pairs, the ones which are located in either donor or acceptor material are denominated polaron pairs while those which are spread across the interface are termed charge transfer excitons (CTE) throughout this thesis.

(iv) Charge Carrier Pair Dissociation

As already mentioned, the dissociation of photogenerated singlet excitons at the donor–acceptor interface leads to still coulombically bound CTE which have to be dissociated as well in order to obtain free charge carriers. For this second dissociation, several alternative mechanisms have been suggested in literature which will be discussed in detail in Chapter 3. Those CTE which are not separated at the interface recombine. The underlying process is called geminate recombination since the participating electron and hole originate from the same precursor state. This monomolecular loss mechanism which is proportional to the CTE concentration either takes place non-radiatively or with a low emission cross section [60]. However, for some polymer–fullerene blends, a detectable PL originating from the recombination of CTE is reported [50, 61, 62, 63, 64, 65]. Apart from CTE dissociation and recombination, a third possible process is electron back transfer from the acceptor LUMO to a triplet state of the donor [66]. However, this is only feasible if the energy of the donor triplet is lower than the energy of the charge transfer state (CTS) which is occupied by the CTE [56].

(v) Charge Carrier Transport

After the dissociation of the CTE, the generated charge carriers have to be transported to the electrodes. In contrast to crystalline inorganic semiconductors where electrons can move almost freely in the conduction band, organic semiconductors are disordered materials. The inherent lack of a long-range order results in a transport mechanism where charge carriers hop from one localized state to the next. Since hole trans-

port predominantly takes place in the donor while electrons are conducted in the acceptor, percolation paths are required in order to carry the polarons to their respective contacts. Separated islands, however, are detrimental to this aim. For the description of the hopping transport, various models have been proposed which are reviewed in detail in Reference [13]. A particularly well-established approach is the one introduced by Bässler [67] where the localized states are distributed in a Gaussian density of states (DOS) with the energetic width σ. The parameter σ reflects the disorder of the system and is usually in the range of 50 meV to 100 meV [68, 69, 70]. Under steady-state conditions, the charge carrier density — not to be confused with the DOS of the LUMO level — thermalizes to about σ^2/kT below the center of the DOS for a given thermal energy kT (see Figure 2.5). However, the charge transport takes place by upward and downward hops around the so-called transport energy [71, 72, 73]. Localized states below the transport energy do not participate in the conduction process and act as traps [35, 74].

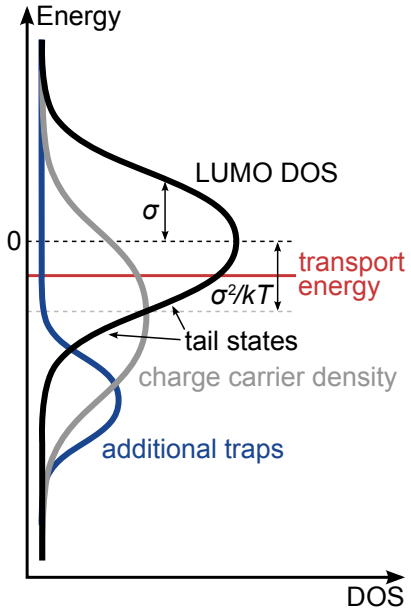

Figure 2.5: Density of states for an organic semiconductor. For steady state conditions, the charge carrier density distribution is shifted to smaller energies with respect to the LUMO DOS. States below the transport energy act as traps (modified from [13] and [35]).

Thus, the lower energetic tail states of the LUMO DOS can be considered as trap states. Additionally, traps are generated by e.g. impurities and structural defects. In the case of PCBM derivatives which possess several isomers with different LUMO levels, the lower LUMO states may act as traps as well. Trap states of any kind have a strong impact on the charge carrier mobility: Once a charge carrier has been trapped, it first has to be released again in order to take part in the conduction process. Thus, trap states lower the mobility, negatively affecting the device efficiency. [35, 74]

Besides, the traps may also act as recombination centers. In general, while the separated charge carriers are transported to their respective electrodes, recombination may occur between two oppositely charged polarons. These charge carriers may either have been generated by the dissociation of two different CTE or injected into the device through the contacts. In any case, since the recombination partners do not originate from the same precursor, the recombination is called non-geminate.
One of the crucial parameters for the description of charge carrier transport is the mobility μ. Macroscopically defined as the fraction between the carrier drift velocity v and the applied electric field F, $\mu = v/F$, the mobility in amorphous organic semiconductors with low charge carrier concentrations is limited by the hopping transport to values $\leq 10^{-3}$ cm^2/Vs (which is orders of magnitude below the ones for inorganic crystals) and experiences both a temperature and a field dependence. However, on a meso- or microscopic scale with a higher order, increased mobilities can be observed for e.g. the movement of charge carriers along a polymer chain. Such local mobilities can be experimentally determined by time-resolved microwave conductivity measurements (TRMC) [75, 76, 77] and represent the intrinsic mobility without the limitations of traps or defects.

(vi) Charge Carrier Extraction

Charge carriers which do not recombine or get caught in deep traps during their transport can finally be extracted at the contacts. In order to contribute to the photocurrent, electrons have to leave the device via the cathode whereas holes have to be extracted through the anode. The extraction of polarons at the opposite electrode, however, constitutes a further loss mechanism which can be circumvented by deploying selective hole or electron transport layers [78, 79, 80, 81, 82]. The generated photocurrent has a major impact on the characteristics of an organic solar cell which will be reviewed in the following section.

2.2.3 Device Characteristics

In general, the performance of an organic solar cell is evaluated via its current–voltage (IV) characteristics, which is schematically shown in Figure 2.6. The generated photocurrent can be extracted from the IV curves by subtracting the dark current from the one recorded under illumination. However, the most decisive figure of merit in organic photovoltaics, the power conversion efficiency η, is determined by three characteristic points in the illuminated current curve, namely the open circuit voltage V_{oc}, the short circuit current I_{sc} (or the corresponding short circuit current density j_{sc}) and the

maximum power point MPP. The specific shape of the IV curve under illumination is influenced by the shift of the energy bands for a certain applied voltage.

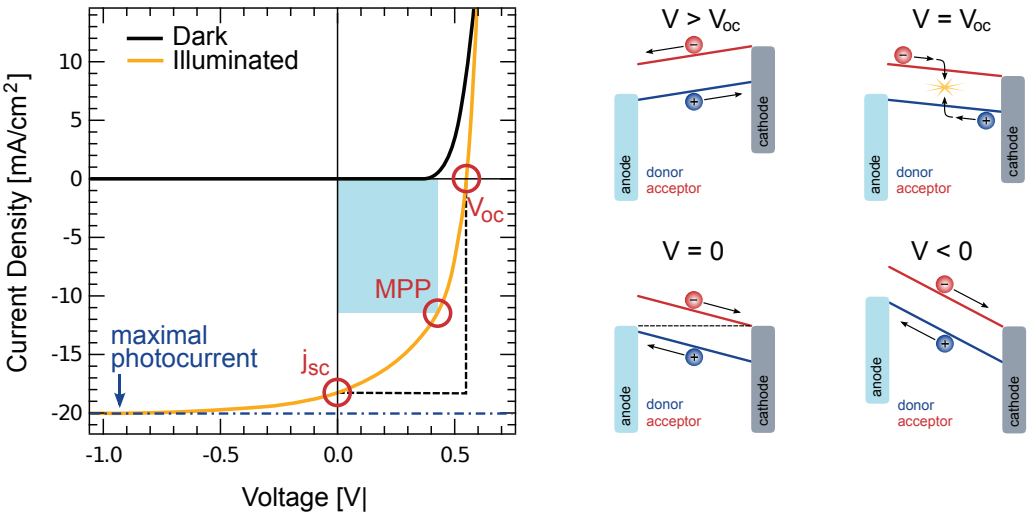

Figure 2.6: Schematic IV characteristics of an organic BHJ solar cell and corresponding band diagrams. The specific shape of the current under illumination is influenced by the configuration of the HOMO and LUMO levels. Characteristic points in the IV curve are the open circuit voltage, the short circuit current and the maximum power point (modified from [13] and [83]).

If a positive bias $V > V_{oc}$ is applied, the HOMO and LUMO levels are tilted in such a way that the injection barriers at the electrodes are lowered. As a consequence, charge carriers are injected into the device, following an approximately exponential increase for a rising voltage. For $V = V_{oc}$, no net current is flowing since in this point, charge carrier generation equals charge carrier recombination. The magnitude of V_{oc} is not determined by the optical gap of the blend constituents but rather scales with the difference between the donor HOMO and the acceptor LUMO level [84, 85]. Accordingly, good correlations between V_{oc} and the spectral position of CTE absorption [60], PL [57] and electroluminescence (EL) [86] were observed [87]. Recently, V_{oc} was found to be closely related to the energy of the CTE by Vandewal et al. [87, 88]; more specifically, the CTE energy determines the maximum achievable V_{oc}. In this scheme, the energetic losses between the CTE energy and $e \cdot V_{oc}$ which are due to both radiative and non-radiative recombination amount to about 0.5 eV to 0.6 eV [88]. If no external bias is applied, i.e., if $V = 0$, short circuit conditions are present. Here, the current flow I_{sc} is due to the difference in work functions of the electrodes. In an ideal device, the maximal photocurrent would be reached under these short circuit conditions. However, as the photocurrent in organic BHJ solar cells is field dependent, most devices reach a saturated photocurrent only for an applied negative voltage. For $V < 0$, the injection barriers at the contacts are high enough to prevent a significant injection current.

At the same time, the electric field in this regime is sufficient to extract all generated charge carriers.
As already mentioned, another characteristic point in the 4th, power-generating quadrant of the IV curve is the MPP where the product of current and voltage reaches a maximum. The MPP is used for the calculation of the fill factor FF which — simply speaking — is a measure of the "squareness" and thus the ideality of the IV curve. It is defined as the fraction to which the product of current and voltage at the MPP fills a square built by the product of I_{sc} and V_{oc}, i.e., the maximal theoretically achievable power:

$$FF = \frac{I_{MPP} \cdot V_{MPP}}{I_{sc} \cdot V_{oc}} \tag{2.1}$$

With the help of the fill factor, the power conversion efficiency of a specific device can be determined which is given by the generated power at the MPP, devided by the power of the incident light P_L:

$$\eta = \frac{I_{sc} \cdot V_{oc} \cdot FF}{P_L} \tag{2.2}$$

The theoretical maximum of the efficiency is given by the detailed balance limit of Shockley and Queisser which was originally derived for inorganic p–n junction solar cells [9]. Accurate and reliable efficiency values are determined under standard recording conditions which are defined as an illumination of 100 mW/cm^2 with an AM1.5G spectrum and a cell temperature of 25 °C. Details of these measurements have been described by Shrotriya et al. [89]. To date, efficiencies for polymer–fullerene BHJ solar cells have reached values exceeding 9 % [90]. Behind the limelight of these promising record efficiency reports, there is an ongoing, controversial discussion about the process of singlet exciton dissociation at the donor–acceptor interface. Different aspects of this mechanism will be discussed in the following chapter.

3 Photoinduced Charge Carrier Generation

On the route to photocurrent generation, the creation of polarons via the separation of the singlet exciton at the polymer–fullerene heterojunction represents a crucial step intermediating photoexcitation and photocurrent extraction. This process is strongly influenced by the presence of interfacial CTS, which will be discussed below. In addition, this chapter introduces several recently presented scenarios for the charge carrier generation mechanism and a theoretical approach for the description of its field dependence. Again, the considerations in Sections 3.1 and 3.3 are mainly based on review articles by Deibel et al. [13, 52] and Clarke et al. [59] which offer a thorough evaluation of this up-to-date research area.

3.1 Charge Transfer States

CTS are interfacial hybrid states forming out through a wavefunction overlap between donor HOMO and acceptor LUMO, schematically represented in Figure 3.1. Thus, hybrid ground and excited states can be present within the optical gap of the two blend components [91]. The CTS can be populated either by CT from a singlet exciton, directly by sub-gap absorption (although the absorption coefficient of CTS is very low compared to the one of singlet excitons) [60, 63, 92] or in a non-geminate recombination process of free polarons.
The CTS is occupied by a CTE consisting of a coulombically bound electron and hole. Here, the CTE binding energy is defined as the difference in potential energy between the CTS and the separated, relaxed charge carriers in their respective host materials. The CTE electron and hole are initially separated by roughly 1 nm which corresponds to the distance of the adjacent donor and acceptor molecules on which the charges reside. Taking into account typical dielectric constants of organic semiconductors of $\epsilon_r \approx 3-4$, this leads to CTE binding energies $E_{b,CTE}$ in the range of 0.36 eV to 0.48 eV, being significantly larger than the room temperature thermal energy of about 25 meV and thus yielding a dissociation probability of zero. For efficient CTE separation at

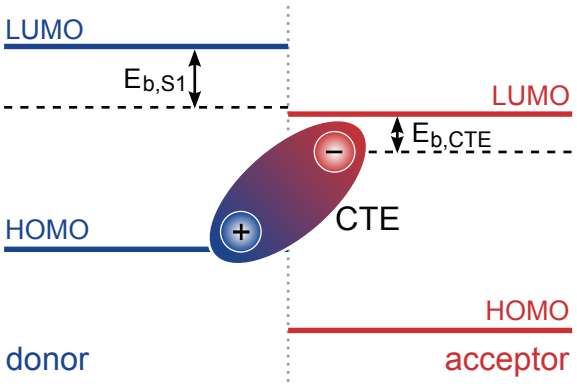

Figure 3.1: Energy level diagram illustrating the formation of an interfacial CTE. The binding energies of the singlet exciton $E_{b,S1}$ and of the CTE $E_{b,CTE}$ are depicted relative to the donor HOMO level (modified from [59]).

room temperature, the electron–hole distance would have to be greater than or equal to the Coulomb capture radius r_c (being defined as the distance where thermal energy equals Coulomb attraction) of about 14 nm to 18 nm. Nevertheless, a non-zero CTE dissociation yield is observed in organic bulk heterojunction devices, hinting at a lowered CTE binding energy. This might be achieved by e.g. the assistance of an electric field (see Section 3.3), an increased delocalization length [93], entropy effects [59] or relaxation processes in the disorder-broadened DOS [67]. Lately, there has been mounting evidence of a dissociation involving vibrationally hot CTS [59, 62, 94, 95, 96] which will be discussed in the following section. For the thermally relaxed CTE, lifetimes in the range of 1 ns to 100 ns have been reported for polymer–fullerene blends [57, 97]. If the CTE are not dissociated into free charge carriers within their lifetime, they can decay via radiative or non-radiative recombination or — as already pointed out in Section 2.2.2 — via electron back transfer. Radiative recombination of CTE results in a broad PL emission band which is red-shifted in comparison to the PL signatures of the individual blend components so that the blend PL spectrum is not merely a superposition of the neat material spectra. For some material combinations such as MDMO-PPV:$PC_{61}BM$ [98] or polyfluorene:$PC_{61}BM$ [65], distinct CTE PL bands can be detected, whereas for other blend systems such as P3HT:$PC_{61}BM$ [91], the CTE emission is only visible as a shoulder at the lower energetic side of the blend spectrum. It should be noted that experimental evidence of CTE is also obtained in polymer–fullerene blend EL spectra [86, 99, 100] which in most cases is red-shifted relative to the CTE PL band [100]. This red-shift is mainly due to EL originating from non-geminate recombination of injected charge carriers whereas the CTE PL is primarily due to geminate recombination [100].

As CTS are the result of a wavefunction overlap between donor and acceptor materials in the blend, the properties of the respective CTE are affected by the blend morphology. Thus, it has been found that an increase of the fullerene fraction in the blend leads to a red-shifting CTE PL maximum [57, 65] and a decreasing CTE PL intensity [57]. This is assumed to be an effect of an increasing effective dielectric constant and a therefore reduced CTE binding energy [57, 65].
Coming to speak of photovoltaic performance, the CTE exerts a considerable influence on both open circuit voltage and photocurrent and thus on the overall device efficiency. As already mentioned in Section 2.2.3, the CTE energy determines the maximum of V_{oc}. Concerning the photocurrent, recent investigations on a series of polythiophenes suggest that charge carrier photogeneration be not limited by the quenching of singlet excitons, but rather by the efficiency of the CTE dissociation process [55, 59]. Moreover, a correlation between a decrease of CTE PL intensity and an increase of charge carrier yield was observed [59, 101], being indicative of the importance of CTE dissociation for photocurrent generation. Accordingly, the recombination of CTE is considered to be a serious loss mechanism in most of the current photophysical models describing charge carrier generation.

3.2 Photophysical Models

During the start-up years of OPV research, the perception of the charge carrier photogeneration process was highly diverse. For instance, Moses et al. [102] suggested in 2000 that free carriers be the primary photoexcitations in conjugated polymers, meaning that their formation would not require a secondary process such as singlet exciton dissociation. In the meantime, it has become generally accepted that in fact, singlet excitons are the primary photoexcitations in organic semiconductors which have to be dissociated in order to generate free charge carriers. However, up to now, there is no consensus about the actual pathways for singlet exciton dissociation at the donor–acceptor interface [54, 59, 96, 103, 104, 105, 106]. The most commonly applied photophysical model describing this process was presented by Brédas et al. [96] and Clarke et al. [59] and is depicted in Figure 3.2. In this model, the photogenerated singlet exciton is quenched by CT of the electron from donor to acceptor and a CTE is formed. Initially, this CTE is vibrationally excited [59, 62, 94, 95, 96] and may possess a sufficient thermal energy to overcome the Coulomb binding energy [55, 59] and create free charge carriers occupying the charge separated state (CSS). Alternatively, the hot CTE can thermally relax in the CTS manifold to the relaxed CTS. Here, the electron–hole distance is also called the thermalization length a. Subsequently, the relaxed CTE can

dissociate into free charge carriers or recombine geminately to the ground state S_0. For reasons of simplicity, electron back transfer to the donor is omitted. The hot CTE experiences a kinetic competition between thermalization and separation to free charge carriers, whereas the relaxed CTE is subject to a kinetic competition between geminate recombination and its separation [59]. The relevance of the different pathways critically depends on the respective rates. According to Brédas et al. [96], two limiting scenarios can be distinguished. In the case that the charge separation rate k_{cs} dominates the thermalization rate k_{th}, i.e., $k_{cs} \gg k_{th}$, singlet exciton dissociation at the interface takes place via hot CTE separation. For $k_{cs} \ll k_{th}$, however, the hot CTE undergoes a relaxation process to its lowest vibrational state. In order for the relaxed CTE to be dissociated, the electron and hole need to overcome their Coulomb binding energy. Thus, the efficiency of this pathway is relatively low and depends on the magnitude of a as compared to r_c.

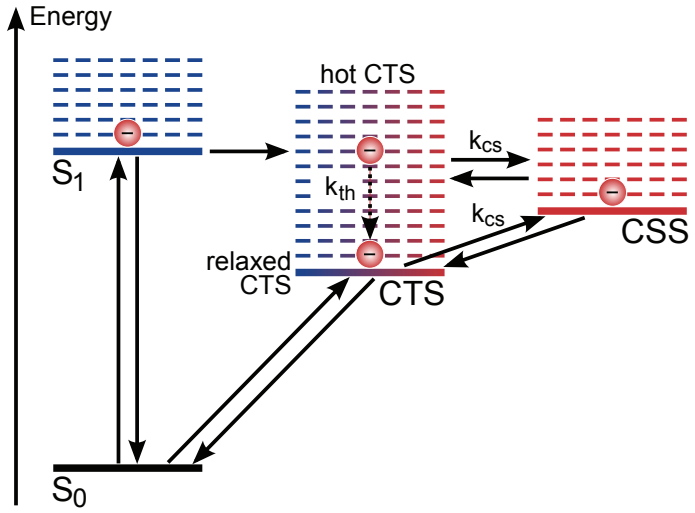

Figure 3.2: Electronic state diagram visualizing the photophysical model suggested by Brédas et al. [96] and Clarke et al. [59]. Singlet exciton separation into free charge carriers is mediated either by the dissociation via a hot CTS or by thermal relaxation of the hot CTE to the relaxed CTS and subsequent dissociation of the relaxed CTE. Triplet levels and electron backtransfer are neglected in this scheme (modified from [59] and [96]).

In an alternative approach for the description of charge carrier photogeneration, the possibility of a direct dissociation of singlet excitons at the donor–acceptor interface has been proposed [54, 103, 107]. In this scenario, free charge carriers are either generated directly from the singlet excitons without passing through any intermediate states or through the dissociation of relaxed CTS. However, the direct dissociation of singlet excitons should experimentally be hard to distinguish from a dissociation via hot CTE.

As for the question whether dissociation of relaxed CTE or dissociation of hot CTE / direct dissociation is the predominant charge carrier photogeneration pathway, controversial experimental evidence has been reported. For the reference systems MDMO-PPV:$PC_{61}BM$ and P3HT:$PC_{61}BM$, Lee et al. [108] performed external quantum efficiency measurements with above-gap and sub-gap excitation, the latter of which was assumed to directly generate relaxed CTE instead of hot CTE. Despite the different excitation energies, no change in the efficiency of charge carrier generation was observed, attributed to the absence of a hot CTE dissociation pathway. The authors concluded that for the studied material systems, charge carriers are generated via the intermediate step of relaxed CTS. In contrast, Mingebach et al. [83] who studied the same material combinations by time delayed collection field experiments came to different conclusions. While they observed a strong field and temperature dependence of the charge carrier generation in MDMO-PPV:$PC_{61}BM$ blends, only a weak dependence was found for P3HT:$PC_{61}BM$. Thus, the MDMO-PPV:$PC_{61}BM$ blends were ascribed a charge carrier dissociation via relaxed CTS, while the hot CTE / direct dissociation pathway was attributed to the P3HT:$PC_{61}BM$ blends. This example demonstrates that the complex mechanism of charge carrier photogeneration is still ambiguous and not easily accessible with the experimental techniques at hand.

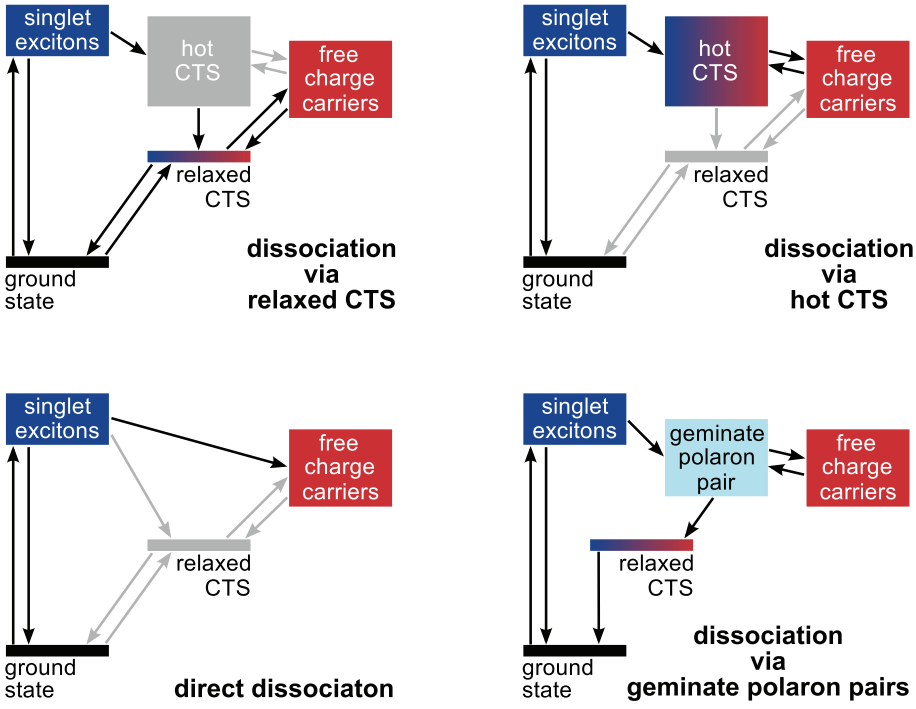

Figure 3.3: Schematic drawing of different dissociation pathways suggested in current literature. It should be noted that experimentally, no clear distinction can be made between dissociation via a hot CTS and direct dissociation. The main dissociation route considered in this thesis is the dissociation via relaxed CTS.

For the sake of completeness, yet another photophysical model has to be mentioned which was proposed by Jarzab et al. [104] and Provencher et al. [105]. From time-resolved experiments on low-bandgap copolymer–fullerene blends, the authors derive a dissociation scheme where the conversion between singlet excitons and free charge carriers is mediated by what the authors call "geminate polaron pairs". CTS may be populated via the geminate polaron pairs, but then act as interfacial defects without the possibility of separation into free charge carriers. This model as well as the other presented dissociation pathways are summarized in the schematic drawing in Figure 3.3. For this thesis, however, the focus is set on the dissociation route via relaxed CTE which is experimentally accessible through CTE PL measurements. It is assumed that singlet exciton separation via hot CTE may also be a relevant or even dominating process, but no distinction is made between the hot CTE dissociation pathway and direct dissociation.

3.3 Field Dependence of Charge Carrier Photogeneration

Proceeding with the assumption of a singlet exciton dissociation process via relaxed CTS, the respective coulombically bound CTE has to be separated in order to gain free charge carriers. As already mentioned in Section 3.1, this separation can be facilitated by an external electric field. A macroscopic theoretical description of field assisted CTE dissociation is given by the established Onsager–Braun model [109, 110], which focuses on the assumption of competing rates and will be discussed in the following.

In his original work dating back to 1938 [109], Onsager calculated the probability for a coulombically bound ion pair executing Brownian motion in an electrolyte to be dissociated. He suggested that via photoabsorption, a localized hole and a hot electron be generated, the latter of which thermalizes at the distance a from the hole (see Figure 3.4). Depending on the Coulomb attraction between electron and hole, recombination of the ion pair to the ground state is competing with dissociation. The charge carriers are considered fully separated if a is greater than the Coulomb capture radius r_c. In the case that a is smaller than r_c, the probability for the dissociation of the ion pair is given by $P(F)$ while the probability for recombination to the ground state is $1-P(F)$. Here, $P(F)$ depends on the applied electric field F, the temperature T and a. The electric field lowers the Coulomb potential barrier and thus enhances the yield of free charge carriers. [59]

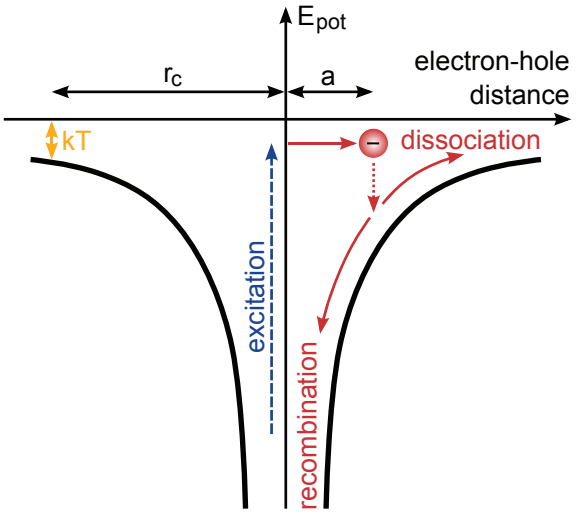

Figure 3.4: Potential energy diagram. After thermalization, the CTE can either dissociate or recombine, depending on its Coulomb binding energy. Charge carriers are considered to be fully separated when their thermalization length a exceeds the Coulomb capture radius r_c for a specific thermal energy kT (adopted from [59]).

Although delivering a reasonable description of the photogeneration process in low-mobility insulators, the Onsager framework leads to thermalization lengths of 2.5 nm to 3.5 nm when applied to the dissociation of CTS in donor–acceptor systems [110], contradictory to the actual nearest-neighbor donor–acceptor distances of about 1 nm. This issue was resolved by Braun in 1984 [110] by introducing a finite CTE lifetime to the model. Moreover, the Braun extension includes that the CTE can make several attempts to be dissociated within its lifetime while the original Onsager model only allows for one such attempt.

In the combined Onsager–Braun model, the CTE can either recombine geminately to the ground state with a constant rate k_f or dissociate into free charge carriers with a field dependent rate $k_d(F)$. The generated charge carriers may subsequently recombine to the CTS with a rate k_r. The competing rates are displayed in Figure 3.5a. The field dependent probability for a CTE to be dissociated is given by [93]

$$P(F) = \frac{k_d(F)}{k_d(F) + k_f} = \frac{\kappa_d^*(F)}{\kappa_d^*(F) + (\mu\tau)^{-1}} \tag{3.1}$$

Here, μ is the sum of electron and hole mobilities and $\tau = 1/k_f$ is the CTE lifetime. The CTE dissociation rate $k_d(F) = \mu \cdot \kappa_d^*(F)$ can be expressed as [93]

$$k_d(F) = \frac{3\gamma}{4\pi a^3} \cdot \exp\left(-\frac{E_b}{kT}\right) \cdot \frac{J_1\left(2\sqrt{-2b}\right)}{\sqrt{-2b}} \tag{3.2}$$

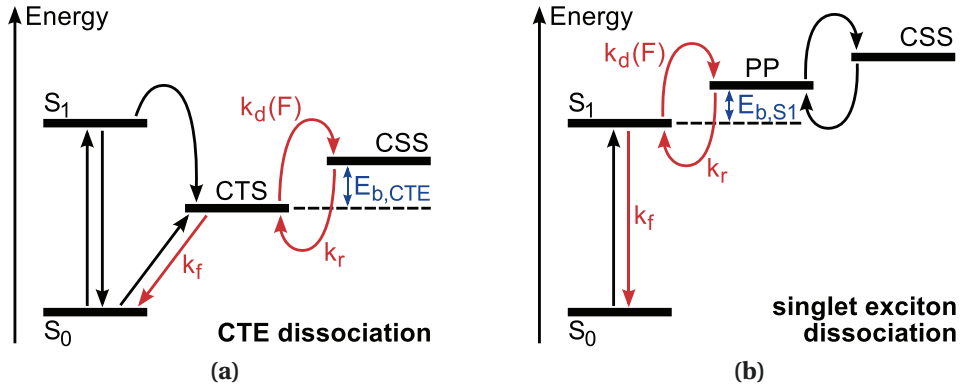

Figure 3.5: Rate model considered within the Onsager–Braun framework. The competing rates are depicted in **(a)** for the dissociation of a CTE in a donor–acceptor blend and in **(b)** for the dissociation of a singlet exciton in a neat organic semiconductor. While $E_{b,CTE}$ describes the Coulomb binding energy which has to be overcome to reach the CSS, $E_{b,S1}$ represents the energy needed for singlet exciton dissociation to a polaron pair (PP) state.

with the Langevin recombination factor $\gamma = q\mu/\epsilon_0\epsilon_r$, the electron–hole distance a, the Coulomb binding energy $E_b = e^2/(4\pi\epsilon_0\epsilon_r a)$ and the thermal energy kT. J_1 is the Bessel function of order one and $b = e^3F/\left(8\pi\epsilon_0\epsilon_r(kT)^2\right)$. Besides, e is the elementary charge, ϵ_0 is the dielectric constant in vacuum and ϵ_r is the effective relative dielectric constant in the bulk. The last factor in Equation 3.2 can be Taylor expanded to [52]

$$\frac{J_1\left(2\sqrt{-2b}\right)}{\sqrt{-2b}} \approx 1 + b + \frac{b^2}{3} + \frac{b^3}{18} + \ldots \tag{3.3}$$

The CTE dissociation rate $k_d(F)$ depends linearly on the mobility μ. Since the dissociation process of the CTE at the donor–acceptor interface is of local character, it is advisable to choose a local mobility when applying the model [52, 57].

The presented framework allows for the calculation of the CTE dissociation yield $P(F)$ for different electron–hole distances a which in turn correspond to different CTE binding energies $E_{b,CTE}$. As can be seen in Figure 3.6, an increasing external electric field leads to an enhanced CTE dissociation. However, assuming reasonable values for the parameters $\mu\tau$, T, ϵ_r and a, relatively high electric fields of the order of 10^7 V/m to 10^8 V/m have to be present for efficient CTE separation.

It should be noted that apart from CTE dissociation, the Onsager–Braun model can also be utilized for the description of singlet exciton separation in a neat organic semiconductor. Here, the conversion to free charge carriers is mediated by a polaron pair [111]. Accordingly, k_f then describes the recombination of S_1 to S_0 and $k_d(F)$ the dissociation rate from S_1 to the polaron pair, which again can recombine to the S_1 state with

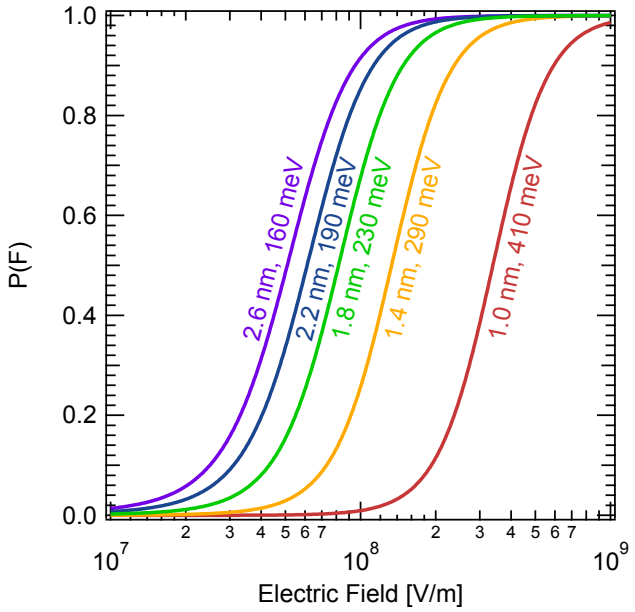

Figure 3.6: Field dependent CTE or singlet exciton dissociation probability as determined with the Onsager–Braun theory. For the calculations, a temperature of $T = 297$ K, an effective relative dielectric constant of $\epsilon_r = 3.5$ and a $\mu\tau$-product of $1.0 \cdot 10^{-17}$ m^2/V were used. The values for the electron–hole distance a and the corresponding binding energies are given in the graph.

the rate k_r (see Figure 3.5b). The singlet exciton binding energy $E_{b,S1}$ which can be determined via Onsager–Braun reflects the energy needed to create the polaron pair and is therefore smaller than the energy required for dissociation to free charge carriers.
Despite being a significant improvement over the original Onsager model by introducing a finite CTE lifetime, the extended Onsager–Braun formalism expresses some drawbacks in the description of charge carrier photogeneration. For instance, it overestimates the experimentally observed temperature dependence of the CTE dissociation process and does not consider energetic disorder or increased local mobilities along polymer chains or in nanocrystalline regions in the blend [13]. Nevertheless, to date, it is the most commonly employed model for CTE dissociation in organic bulk heterojunction solar cells [13, 112, 113, 114] and has also been found suitable for the description of the experimental results which are reported in this thesis.

4 Materials and Devices

For the investigation of charge carrier photogeneration via relaxed CTS, the use of a suitable material system displaying an easily detectable CTS emission is required. To date, one of the most commonly applied reference systems in OPV is P3HT:PCBM, with reported device efficiencies of up to 4.4 % [115]. However, as already mentioned in Section 3.1, CTS emission in this system is weak and cannot be clearly distinguished from the residual PL of the individual blend components. Although a distinct PL emission can be observed for some of the well-performing low-bandgap copolymer blends such as poly[2,1,3-benzothiadiazole-4,7-diyl[4,4-bis(2-ehtylhexyl)-4H-cyclopenta[2,1-b:3,4-b']dithiophene-2,6-diyl]] (PCPDTBT) and PCBM [104] with power conversion efficiencies of up to 5.5 % [34], this CTS PL is spectrally situated too far in the infrared region to be detected with the experimental means available for this thesis (see Chapter 5). Yet, a pronounced CTS emission within the detection range of standard Si photodiodes can be detected for another OPV work horse, namely MDMO-PPV:PCBM [98]. For this well-characterized material system, maximum power conversion efficiencies of 2.5 % to 3 % have been reported for the best-performing blend ratio of 1:4 [30, 41, 116]. The following chapter presents some of the basic properties of the used donor and acceptor materials along with the main processing steps for the fabrication of solar cell devices.

4.1 MDMO-PPV

MDMO-PPV (poly[2-methoxy-5-(3',7'-dimethyloctyloxy)-1,4-phenylenevinylene]) is an electron donating material which belongs to the class of conjugated polymers and is also known in literature under the name OC_1C_{10}-PPV. The MDMO-PPV batch used in this thesis was purchased from Sigma-Aldrich. It is based on PPV monomers consisting of a benzene ring with two carbon atoms attached to it which serve as a link between adjacent monomer units. PPV was first synthesized in 1968 [117] and gained historical significance as the material for which EL in conjugated polymers was discovered in 1990 [118]. Its derivative MDMO-PPV is extended by side chains which ensure a better solubility in common solvents (see Figure 4.1).

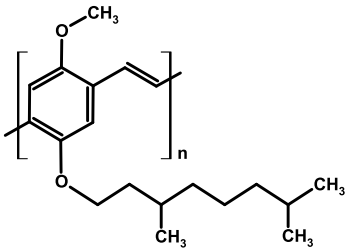

Figure 4.1: Chemical structure of MDMO-PPV. The attached side chains lead to an improved solubility as compared to PPV.

As can be seen in Figure 4.2, MDMO-PPV absorbs in the range of 350 nm to 550 nm and thus can be excited by e.g. 532 nm laser light. Different values for the HOMO and LUMO levels of this conjugated polymer can be found in literature: HOMO energies are reported in the range of 5.0 eV to 5.4 eV, while LUMO energies vary between 2.8 eV to 3.2 eV relative to the vacuum level [119, 120, 121, 122]. The optical gap has been found to be about 2.1 eV [119]. The hole mobility in neat MDMO-PPV is about $5.0 \cdot 10^{-7}$ cm^2/Vs [68] and thus comparatively low. This conjugated polymer also possesses a relatively low dielectric constant of $\epsilon_{r,PPV} = 3.0$, which has been determined from spectral impedance measurements [123] and which leads to a strong Coulomb binding of the photoinduced singlet excitons. For efficient charge carrier generation, MDMO-PPV is usually mixed with fullerene derivatives such as $PC_{61}BM$.

4.2 Fullerene Derivatives

Fullerene derivatives are electron accepting materials and — as the name already indicates — are based on fullerenes, i.e., spherical, hollow carbon cages such as the well-known buckminsterfullerene C_{60}. The different derivatives used in this thesis were purchased from Solenne BV. In general, fullerene derivatives possess several intrinsic properties which make them suitable for OPV applications. For instance, they display an ultrafast forward photoinduced electron transfer when blended with conjugated polymers. Moreover, due to their symmetry, they exhibit an isotropy in electron acceptance which is beneficial for exciton diffusion, CT and charge carrier mobility. In addition, a high exciton diffusion length of the order of 40 nm [124] as well as a high relative dielectric constant of $\epsilon_{r,C60} = 4.4$ [125] have been reported for C_{60}. [126]

However, fullerenes are hardly soluble in organic solvents [127] so that a solubility-enhancing side chain has to be added for the use in solution-processed BHJ solar cells, which was first demonstrated on $PC_{61}BM$ in 1995 [26].

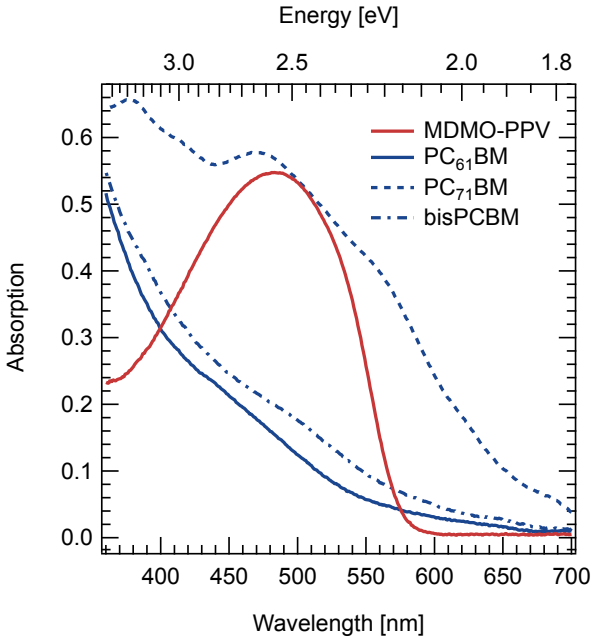

Figure 4.2: Absorption spectra of the used organic semiconductors. With respect to $PC_{61}BM$, the absorption spectrum of $PC_{71}BM$ is extended to longer wavelengths, leading to higher efficiencies in OPV devices. It should be noted that the active layer thicknesses were not accounted for in the absorption spectra (absorption data courtesy of André Thiem-Riebe, Experimental Physics VI).

$PC_{61}BM$

$PC_{61}BM$ ([6,6]-phenyl-C61 butyric acid methyl ester) is the most commonly used fullerene derivative in OPV to date. Its absorption spectrum can be seen in Figure 4.2. As for the actual energy of the HOMO and LUMO levels in $PC_{61}BM$, no consensus has been found in literature so far. Reported LUMO energies range from 3.7 eV to 4.5 eV, while HOMO energies are usually stated to be about 6.0 eV to 6.1 eV [120, 122, 126, 128]. The optical gap of this fullerene derivative is about 1.7 eV [126]. The electron mobility in neat $PC_{61}BM$ has been found to be about $2.0 \cdot 10^{-3}$ cm^2/Vs [129] which is a factor of 4000 larger than the hole mobility in neat MDMO-PPV. Besides, the relative dielectric constant of $PC_{61}BM$ has been reported as $\epsilon_{r,PCBM} = 3.9$ [129]. It is assumed that this relatively high $\epsilon_{r,PCBM}$ causes an increase of the effective dielectric constant in blends with MDMO-PPV, likely leading to a reduced exciton binding energy. Apart from $PC_{61}BM$, various other fullerene derivatives have been deployed in organic BHJ solar cells in an attempt to increase the device efficiency.

$PC_{71}BM$

The best-performing fullerene derivative so far is $PC_{71}BM$ ([6,6]-phenyl-C71 butyric acid methyl ester). The high performance can be attributed to the higher absorption

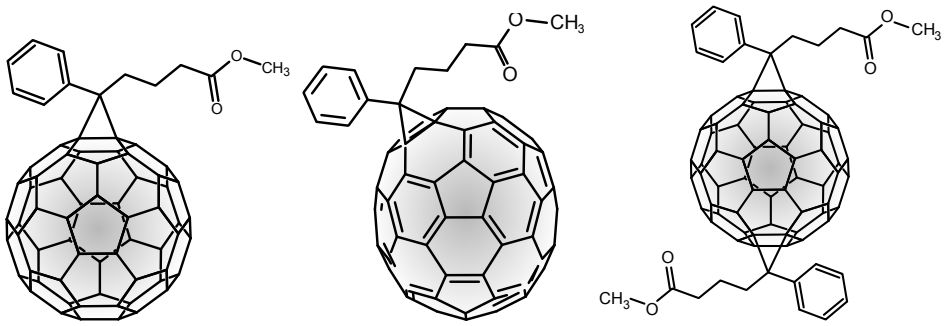

(a) **(b)** **(c)**

Figure 4.3: Chemical structure of different acceptor materials. The fullerene derivatives used in this thesis are **(a)** $PC_{61}BM$, **(b)** $PC_{71}BM$ and **(c)** bisPCBM.

coefficient at longer wavelengths as compared to $PC_{61}BM$ [41] (see Figure 4.2), thus allowing for harvesting a larger part of the solar spectrum for exciton generation. The better absorption of $PC_{71}BM$ is mainly due to the higher molecular weight [126] and the asymmetry of the C_{70} cage [41]. This asymmetry is also the cause for the existence of one major and two minor $PC_{71}BM$ regioisomers [41]. Despite these differences to $PC_{61}BM$, the LUMO level of $PC_{71}BM$ is only altered by a few meV as compared to the one of $PC_{61}BM$ [27].

bisPCBM

Another fullerene derivative which is investigated in this work is bisPCBM, the bisadduct analogue of $PC_{61}BM$ with a similar absorption spectrum (see Figure 4.2). The addition of a second side chain leads to a rise in the LUMO energy of about 0.1 eV as compared to $PC_{61}BM$, resulting in a higher V_{oc}. Due to the two side chains which can be attached to different carbon atoms of the C_{60} cage, there also exist several regioisomers of bisPCBM. [130]

All presented materials were processed in a similar way which is described in detail in the following section.

4.3 Device Fabrication

For this thesis, solution-processed BHJ solar cell devices were investigated. Active layers consisted either of a neat MDMO-PPV film or of a mixture between MDMO-PPV and a fullerene derivative in various blend ratios. For processing, the donor and acceptor materials presented in Sections 4.1 and 4.2 were each solved in chlorobenzene

which has been shown to produce a more favorable morphology and a higher power conversion efficiency for the investigated device structures than the alternative solvent toluene [30]. MDMO-PPV was solved with a concentration of 5 mg/ml, while for the fullerene derivatives, concentrations of 30 mg/ml were prepared. All solutions were kept stirring on a hotplate set to 45 °C for several hours and blended in the desired ratio about one hour prior to processing.

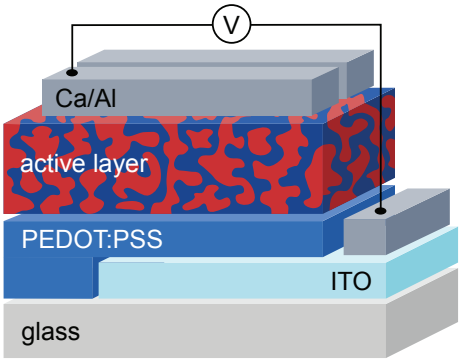

Figure 4.4: Device structure of the solar cells used in this work. The ITO layer is structured in order to avoid contact between the top Ca/Al electrodes and the bottom ITO electrode. Prior to evaporating the top contacts, part of the active and PEDOT:PSS layers are scratched away so that the ITO anode is exposed. Due to the particular geometry of the top electrodes, one sample consists of two solar cell devices.

The device structure utilized throughout this work is schematically depicted in Figure 4.4; the necessary processing steps are listed in the following.

Substrate Preparation

As substrates, 1.1 mm thick glass sheets covered with a 100 nm to 200 nm layer of transparent indium tin oxide (ITO) serving as anode were used. These substrates were purchased from Visiontek Systems Ltd. and cut into 2.54 cm × 1.27 cm pieces for further processing.
In order to avoid a later contact between top and bottom electrodes when attaching wire bonds to the samples, the ITO layer was structured by wet chemical etching. Beforehand, the samples were cleaned following the subsequent routine:

- mechanical cleaning with deionized H_2O and soap
- 10 minutes in ultrasonic bath with deionized H_2O and soap
- rinsing with deionized H_2O
- 10 minutes in ultrasonic bath with acetone
- 10 minutes in ultrasonic bath with isopropanol

Afterwards, the substrates were heated to 120 °C to evaporate any remaining isopropanol. Next, the positive photoresist AZ 1518 from MicroChemicals GmbH was spin-cast with a rotation speed of 3000 rpm, an acceleration time of 1 s and a spin-coating time of 60 s, followed by a second heating step at 100 °C for 50 s. The samples were then placed on a shadow mask and exposed to ultraviolet light for 59 s. Subsequently, the photoresist was developed by applying the MicroChemicals GmbH AZ 351B developer in a 1:3 mixture with deionized H_2O for 2 × 30 s. The developing process was stopped by deionized H_2O. Next, the ITO was etched with a mixture of H_2O, HCL and HNO_3 in a 12:12:1 ratio for 10 minutes in the ultrasonic bath. Again, the etching process was stopped with deionized H_2O. Finally, the remaining photoresist was removed with acetone.
For further processing, the structured ITO substrates were cleaned a second time following the above described routine. Additionally, all remaining impurities were removed by oxygen plasma etching for 30 s. The various cleaning steps have been found to strongly influence the work function Φ_{ITO} of ITO [131] which has been reported to vary between 4.3 eV and 4.8 eV [131, 132].

PEDOT:PSS Processing

Under ambient conditions, the structured and cleaned substrates were coated with poly(3,4-ethylenedioxythiophene):poly(styrenesulfonate) (PEDOT:PSS) from an aqueous dispersion, purchased under the name Clevios P VP AI 4083 from Heraeus. This hole transport layer not only limits recombination at the ITO anode, but also helps to smooth the rough ITO surface in order to avoid shunts. Literature values for the work function $\Phi_{PEDOT:PSS}$ range from 4.7 eV to 5.4 eV [133]. The PEDOT:PSS was spin-cast with a rotation speed of 3000 rpm, an acceleration time of 1 s and a spin-coating time of 60 s, yielding film thicknesses of 35 nm to 40 nm. Subsequently, the samples were transferred into a two-chamber glovebox system under nitrogen atmosphere where they were heated on a hotplate set to 130 °C for 10 minutes in order to remove remainders of H_2O and to improve the conductivity of the layer.

Active Layer Processing

For processing of the active layers, the samples were kept under nitrogen atmosphere for the exclusion of H_2O (< 0.5 ppm) and O_2 (< 0.2 ppm). The respective active layers — neat MDMO-PPV or MDMO-PPV blended with a fullerene derivative in different blend ratios — were spin-cast using two consecutive stages, the first one with a rotation speed of 800 rpm, an acceleration time of 1 s and a spin-coating time of 60 s, and the second

one with a higher rotation speed of 3000 rpm, an unaltered acceleration time and a reduced spin-coating time of 10 s. While the first, slower stage determines the thickness of the active layer, the second, fast one ensures the removal of residual chlorobenzene. Depending on the respective material combination, active layer thicknesses of 60 nm to 100 nm were produced which were determined with a Veeco Dektak 150 profilometer after the completion of all desired measurements on the respective sample. After the spin-coating process, part of the active layer and the underlying PEDOT:PSS layer were scratched away in order to expose the ITO anode.

Top Electrode Evaporation

After spin-coating of the active layers, the samples were transferred under nitrogen atmosphere into a thermal evaporation chamber which is included in the glovebox system. Under high vacuum ($< 10^{-6}$ mbar), the top electrodes were deposited through a shadow mask. They usually consisted of a 3 nm thick Ca layer and a 100 nm to 140 nm thick Al layer. The main purpose of the Ca layer is to reduce Al diffusion into the active layer which contributes to sample degradation. The work functions of Ca and Al are $\Phi_{Ca} = 2.9$ eV and $\Phi_{Al} = 4.3$ eV, respectively [134]. The complete energy level alignment of a finished device is shown exemplarily for a MDMO-PPV:$PC_{61}BM$ blend in Figure 4.5.

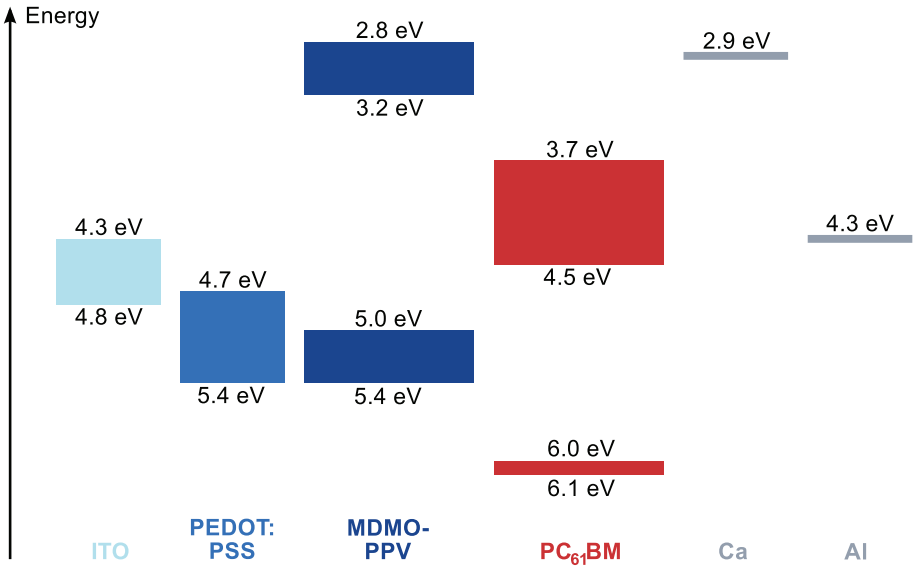

Figure 4.5: Energy level alignment for an organic solar cell device in the configuration ITO – PEDOT:PSS – MDMO-PPV:$PC_{61}BM$ – Ca – Al. The values for the work functions and HOMO and LUMO energies are extracted from literature and given relative to the vacuum level.

As predetermined by the geometry of the shadow mask, each sample was equipped with two parallel top electrodes, both sharing the ITO anode as counter electrode. The

anode was accessed via evaporation of a third Ca/Al stripe perpendicular to the two top electrodes and situated directly over the previously uncovered part of the ITO layer. Determined by the spatial overlap between top and bottom electrodes, all fabricated solar cells possessed an active layer of 0.5 cm^2.

Device Characterization and Mounting

Directly after top electrode deposition, the IV characteristics of the devices were measured inside the glovebox system, using a Keithley 237 source-measure unit (SMU) and an Oriel 81160 AM1.5G solar simulator with an irradiation of 100 mW/cm^2. Subsequently, the devices were transported under ambient conditions to the respective experimental setups (i.e., PL(F) or field dependent transient absorption TA(F) which are described in Chapter 5). Here, they were mounted on the sample holder of a coldfinger cryostat and connected to the electrical contacts with small pre-cut pieces of indium. The conduction of the various experiments which were performed on the samples is explained in the following chapter.

5 Experimental Techniques

For the investigation of the field dependence of charge carrier photogeneration in organic BHJ solar cells, the main experimental method used in this work was field dependent photoluminescence (PL(F)). It detects the radiative recombination of singlet excitons or CTE under the influence of an external electric field and thus yields information on the field dependent dissociation of the respective species. The results obtained by this technique may be complemented by additional field dependent transient absorption measurements (TA(F)). This method directly probes the generated polarons and — in combination with PL(F) — allows for the conception of the complete charge carrier photogeneration process from CTE to free polarons. PL(F) and TA(F) investigations are supported by morphological characterizations of the studied blends. In this context, both atomic force microscopy (AFM) and optically detected magnetic resonance (ODMR) are used to gain a comprehensive picture of the underlying blend morphology. All of the mentioned experimental techniques are described in the subsequent sections.

5.1 Field Dependent Photoluminescence – PL(F)

Steady-state and time-resolved PL(F) has been widely applied in literature for the investigation of the field dependence of exciton dissociation [57, 98, 101, 111, 135, 136, 137, 138]. The concept of steady-state PL(F) as applied in this thesis is rather simple: The PL originating from the recombination of singlet excitons in neat MDMO-PPV or of CTE in MDMO-PPV blended with a fullerene derivative is detected while an external electric field is applied to the device. The electric field constitutes an additional driving force for exciton dissociation. As the field increases, more and more of the singlet excitons or CTE are able to overcome their Coulomb binding energy and to dissociate into free charge carriers. As a result, the recorded PL intensity decreases. Here, it should be noted that according to Veldman et al. [57], the electric field does not alter the amount of generated CTE so that the CTE PL reduction with increasing field can be solely attributed to CTE dissociation.
The field dependent quenching may be calculated via

$$Q = \frac{[PL(0) - PL(F)]}{PL(0)} \tag{5.1}$$

where $PL(F)$ and $PL(0)$ are the PL signals at a certain electric field F and under field-free conditions, respectively. In this context, "field-free" does not mean that no external electric field is applied, but rather that the applied field corresponds to an applied voltage of V_{oc}. Under the assumption that the PL quenching Q equals the exciton dissociation probability $P(F)$ as described in Equation 3.1, the results obtained from PL(F) measurements can be used to determine the singlet exciton or CTE binding energy within the Onsager–Braun framework (see Section 3.3). This is realized by using $P(F)$ as a fit function where the fit parameter is chosen as the electron–hole distance a, being directly related to the Coulomb binding energy. As for the other input parameters, the temperature T is determined by the experimental conditions while reasonable assumptions based on literature values have to be made for the relative dielectric constant ϵ_r and the $\mu\tau$-product. The suitability of the Onsager–Braun theory for the description of PL(F) measurements has already been validated in literature [98, 111, 138] and is also proven in the presented work.
Coming to speak of the actual conduction of the PL(F) experiments, two different measurement routines were deployed for this thesis which are described in the following.

5.1.1 Measurement Routines

Due to the low PL intensities especially in the case of the CTE, lock-in amplification was used for the detection of the PL signals. In simple words, this is a phase-sensitive technique which only amplifies the part of the incoming signal which has been modulated with a certain frequency. This frequency also has to be set as the reference frequency on which the lock-in amplifier is triggered. The lock-in amplifier then acts as a narrow band pass filter, extracting the desired signal from the noise. The basic requirement for this technique is the modulation of the measurement signal, i.e., in this case of the field dependent singlet exciton or CTE PL. This can be accomplished either by modulating the excitation of the sample or by modulating the voltage which is applied to the device.

Excitation Modulation

The standard measurement routine for PL(F) experiments is excitation modulation. As in the presented work, a continuous wave (cw) laser instead of a pulsed one is used for the irradiation of the samples, a mechanical chopper wheel is utilized to achieve a modulation of the excitation, cutting the laser beam into periodic pulses. The PL re-

sponse of the excited sample follows this periodic modulation, allowing for lock-in detection. The output of the lock-in amplifier corresponds to the signal difference due to the modulation, i.e., in this case between illumination and no illumination of the sample. Under field-free conditions $PL(0)$, this signal difference is maximal and decreases for an increasing electric field. For a certain applied electric field strength, the lock-in amplifier integrates over several periods (see Figure 5.1a) in order to reach a better signal-to-noise ratio (SNR). From the recorded data, the field dependent PL quenching can be calculated via Equation 5.1. It should be noted that for this measurement routine, EL originating from injected charge carriers is not detected since it is not modulated with the frequency of the laser chopper. If not indicated otherwise, the excitation modulation technique was used for the later described PL(F) experiments in this thesis.

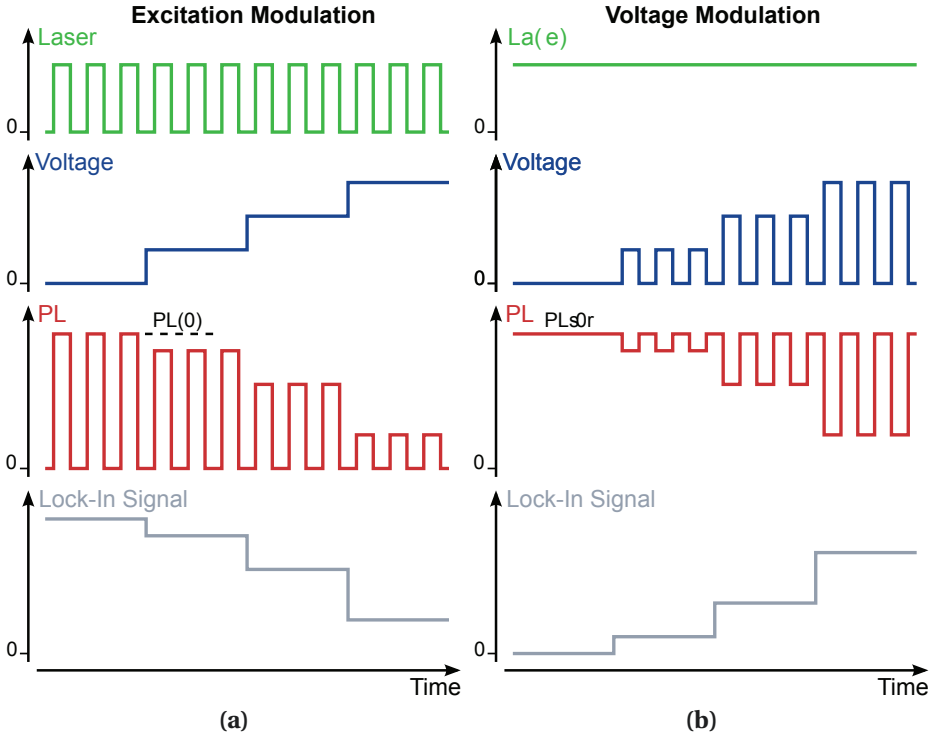

Figure 5.1: Schematic presentation of the different modulation routines. For the excitation modulation shown in **(a)**, the laser is modulated while the voltage is increased in constant steps. In the case of the voltage modulation shown in **(b)**, laser irradiation is kept constant and the voltage is modulated. The two modulation techniques cause a different PL response which also results in a different output of the lock-in amplifier.

Voltage Modulation

Some drawbacks of the above described excitation modulation method can be seen e.g. in the continuous stress which the sample is exposed to due to the constantly applied voltage. Also, this constant voltage might lead to the formation of space charges which could decrease the actually prevailing field strength. These shortcomings are circumvented by the newly developed alternative approach of voltage modulation. Here, the sample is irradiated constantly with the cw laser while the required PL signal modulation is achieved by pulsing the applied voltage via an arbitrary waveform generator. Thus, the field dependent PL is modulated with the same frequency as the external voltage and can be detected with the lock-in amplifier. If no voltage is applied to the sample, the PL signal stays constant, yielding no output of the lock-in amplifier. However, for an increasing voltage, the difference in the PL signal between an applied voltage and zero applied voltage gets larger as the PL decreases (see Figure 5.1b). Accordingly, for this measurement routine, the output of the lock-in amplifier directly reflects the field dependent PL quenching $PL(0) - PL(F)$ (not normalized to $PL(0)$, in contrast to Equation 5.1). Although the voltage modulation reduces the stress on the sample by only exposing it to short voltage pulses instead of a constant voltage, this method is also sensitive to the EL of injected charge carriers which is intrinsically modulated with the voltage frequency. Moreover, voltage modulation does not allow for a direct detection of the zero field PL signal $PL(0)$, which has to be extracted from excitation modulation measurements for the determination of exciton binding energies. Especially the latter aspect is a serious drawback of the voltage modulation technique so that for this work, it was only used as proof-of-concept and in order to validate the results obtained via the excitation modulation.

5.1.2 Experimental Setup

Both excitation modulation and voltage modulation were implemented in the same experimental setup, which is shown schematically in Figure 5.2.

In the PL(F) setup, the samples were placed inside a Janis ST-100 coldfinger cryostat which is equipped with three contacts, allowing for the simultaneous contacting of both top cathodes and the shared bottom anode. Although the cryostat gives access to temperatures in the range between 4.5 K and 300 K, all results reported in this thesis were obtained at room temperature (T = 297 K). The devices in the cryostat were set under dynamic vacuum in order to minimize degradation effects due to oxygen and water.

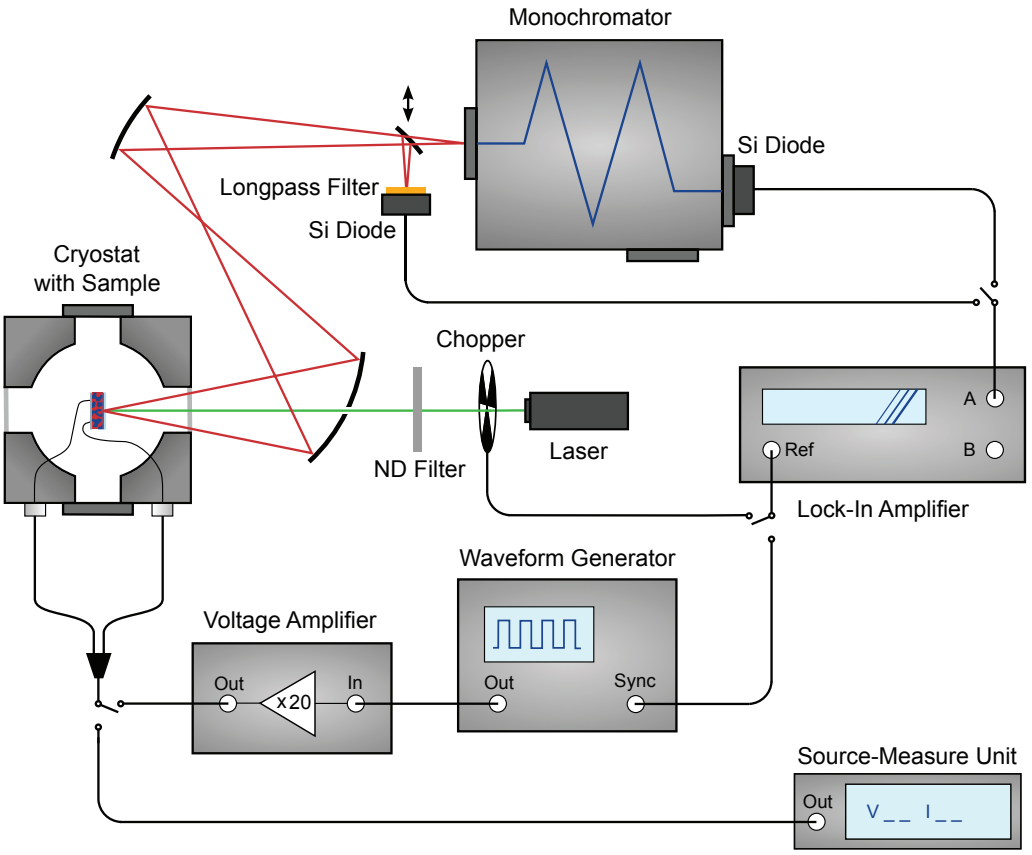

Figure 5.2: Experimental setup for PL(F) measurements. Modulation of the PL signal for lock-in amplifier detection is either achieved via excitation modulation (applying the laser chopper and the SMU for voltage supply) or via voltage modulation (using the cw laser beam and the waveform generator with subsequent voltage amplification). The modulated PL signal is either detected wavelength-resolved with the monochromator and the attached Si diode or integrally with the stand-alone Si diode.

The samples were excited through the transparent ITO anode with a diode pumped solid state (DPSS) cw laser purchased from Atelier Rieter GmbH, emitting green light with a wavelength of 532 nm and an output power of 400 mW. As an exposure to this intense radiation would instantly destroy the used organic materials, the power was reduced by several absorptive neutral density (ND) filters and an adjustable ND filter wheel to about 1 mW to 15 mW, depending on the respective sample. For excitation modulation measurements, the laser light was modulated with a frequency of about 360 Hz by a mechanical chopper wheel.

An external electric field was applied with a Keithley 237 SMU in reverse bias direction in order to minimize effects of injection (see Section 5.1.4). For voltage modulation measurements, however, the SMU was replaced by an Agilent 33250A arbitrary waveform generator, yielding a square wave voltage with a duty cycle of 50 %. Since the maximal peak-to-peak output of this waveform generator is limited to 10 V, an additional

SI Scientific Instruments A400DI two-channel high voltage amplifier with an amplification factor of 20 was used. For comparability to excitation modulation measurements, the frequency of the square wave voltage was chosen as 360 Hz as well.

The emitted PL from the active layer was collected through the ITO anode via two large spherical mirrors. As for the detection of the PL, two options were available, depending on the desired application:

- For wavelength-resolved PL(F) measurements or for the recording of PL spectra, the collected PL was focused onto the entrance slit of a Cornerstone 260 1/4 M monochromator purchased from L.O.T.-Oriel. Equipped with a triple grating turret and two output ports, this monochromator covers the wavelength range of 560 nm to 5500 nm. The visible and near-infrared part of this range was addressed with a Si diode attached to the axial monochromator exit and the diode output was preamplified with a Gigahertz-Optik P-9202-05 current-to-voltage amplifier with adjustable gain. Here, a gain of 10^5 was used for the detection of singlet excitons in MDMO-PPV, while the weak CTE emission in blend systems had to be recorded with a gain of 10^7. For higher wavelengths, a Judson Technologies InSb detector (not shown in Figure 5.2) with a fixed gain preamplifier was attached to the lateral monochromator exit slit. However, the high noise level and the non-adjustable gain of 10^5 made the infrared detector unsuitable for the detection of CTE, limiting the choice of material systems to those with CTE emission in the Si diode range. Accordingly, all PL spectra and wavelength-resolved PL(F) measurements reported in this thesis were recorded with the Si diode.

- Alternatively, the field dependent PL emitted from the samples could be detected integrally with a stand-alone Si diode, yielding a higher signal intensity and a better SNR than wavelength-resolved detection. Also, effects of a possibly shifting PL peak position due to the applied electric field (Stark shift) are reduced. An integral recording of the PL is justified as the PL spectrum is quenched uniformly with the application of an increasing electric field, as will be shown in Chapter 6. In order to exclusively capture the desired singlet exciton or CTE PL signal and to avoid an offset originating from collected laser stray light, several longpass filters were mounted directly in front of the Si diode. Here, the cut-on wavelength was chosen as 550 nm for singlet excitons in MDMO-PPV and 800 nm for CTE in blends of MDMO-PPV and fullerene derivatives. The output of the Si diode was preamplified with the same current-to-voltage amplifier and the same gain settings as for wavelength-resolved PL detection.

Irrespective of the chosen detection method, the preamplified PL signal was sent to one of the input channels of an Ametek Signal Recovery 7265 DSP lock-in amplifier. As reference, the chopper frequency was used in the case of excitation modulation while the square wave voltage frequency from the wavefunction generator was applied in the case of voltage modulation. For each data point, the integration time of the lock-in amplifier was chosen as 100 ms.

The readout of the data as well as the communication with all used instruments was accomplished with the software LabVIEW from National Instruments. For the subsequent processing of the recorded data sets, IGOR Pro from WaveMetrics was used. Data processing included e.g. the subtraction of the background which was experimentally determined for each measurement by replacing the actual device by a sample without an active layer, i.e., with the structure glass — ITO — PEDOT:PSS — Ca/Al. Also, PL spectra were corrected for the spectral response of the monochromator gratings and the sensitivity curve of the Si diode. The calculation of the field dependent PL quenching and the determination of exciton binding energies was automated via separate macros. IGOR Pro was also used for the visualization of the data in the graphs shown in this thesis.

In order to examine the reliability of the later presented experimental results, preliminary tests were carried out, focusing on laser and voltage induced sample degradation and the influence of injected charge carriers on PL quenching.

5.1.3 Sample Degradation

During all PL(F) experiments, the respective samples were simultaneously exposed to laser irradiation and an externally applied voltage, the extent of both exceeding the standard operating conditions of solar cells. In order to account for a possible consequential sample degradation, preliminary measurements were carried out, separately evaluating the effects of laser and voltage induced changes of the observed PL intensity. Beforehand, the stability of the used laser was examined. Specified with a power instability of < 1 %, the output of the laser was focused on a glass slide which was placed at the usual sample position in the cryostat. Similar to the detection of the PL originating from a sample, the scattered laser light was recorded by the monochromator–diode system at a wavelength close to the emission peak at 532 nm. The inclusion of the optical pathways and the various detector elements in the evaluation of the laser stability ensured a good comparability to the subsequent actual measurements.

The laser intensity, detected over a time of more than 100 minutes and thus by far exceeding the usual measurement time of 1 minute to 10 minutes, is shown in Figure 5.3.

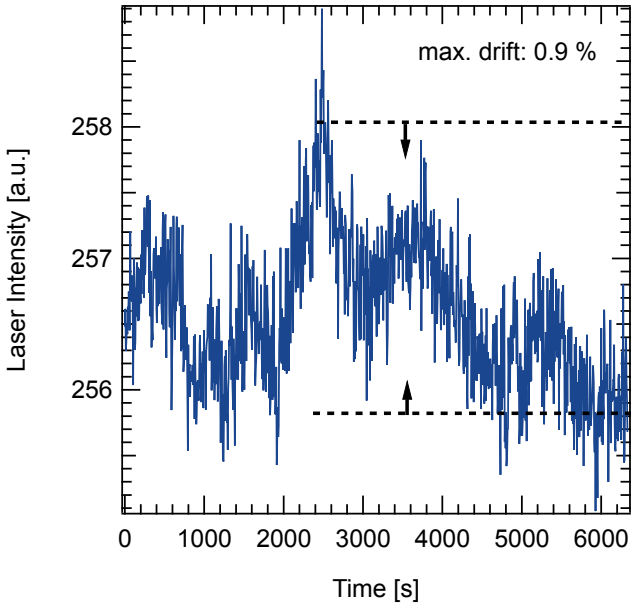

Figure 5.3: Laser intensity, monitored over a time of more than 100 minutes. Excluding the noise, an intensity drift of less than 0.9 % is observed.

Not considering the noise, the fluctuations of the laser intensity are found to be smaller than 0.9 %, allowing for an accurate determination of the actual PL intensities.

Laser Induced Sample Degradation

In order to study the influence of laser irradiation on sample degradation, two exemplary samples — using MDMO-PPV and MDMO-PPV:$PC_{61}BM$ 1:1 as active layers — were exposed to the laser light without any external voltage being applied. The irradiation time was chosen as the maximal time needed for a PL(F) measurement while the laser intensities were set to typical values with respect to the respective active layer, i.e., 1 mW for neat MDMO-PPV and 10 mW for the blend with $PC_{61}BM$. The PL intensity was detected wavelength-resolved with the monochromator–diode system, set to a wavelength close to the emission peak of the active layer. For each sample, several runs with the laser being focused on different spots of the sample were performed, two of which are depicted in Figure 5.4a for neat MDMO-PPV and Figure 5.4b for MDMO-PPV:$PC_{61}BM$ 1:1.

In the case of neat MDMO-PPV, the maximal observed PL intensity drift with time is smaller than 0.6 % for both shown experimental runs and thus in the range of the laser intensity fluctuations. For the blend system, one run does not show any significant PL intensity shift while the other run displays an increase of PL intensity which is smaller than 2.0 % and therefore larger than the laser instability. The latter might be explained by the very low overall signal height or a spatial shift of the laser position on the sample.

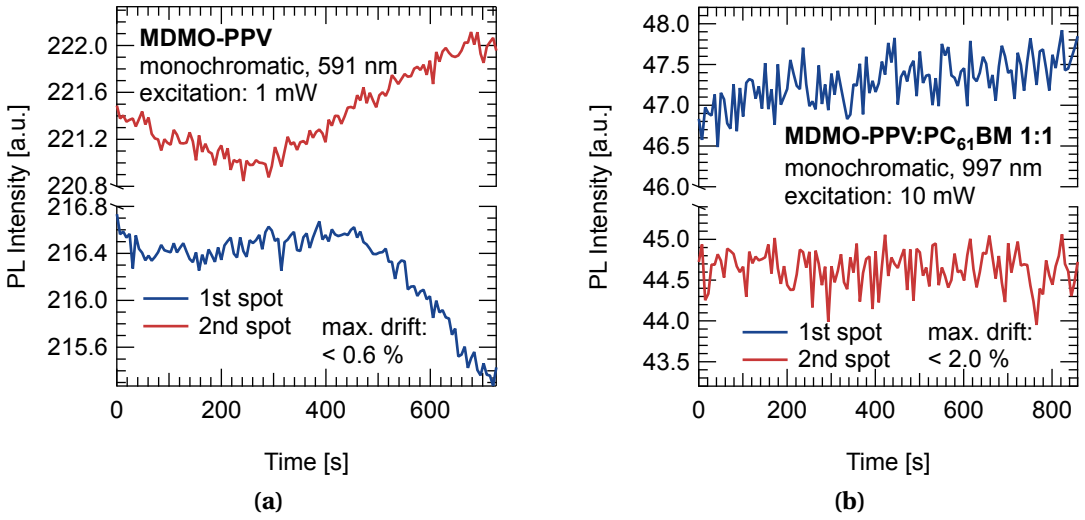

Figure 5.4: Investigation of the sample degradation due to laser irradiation. The PL intensity variation over time was detected in two consecutive runs with different laser positions on the sample. **(a)** For neat MDMO-PPV, the PL intensity drift is smaller than 0.6 %. **(b)** In the case of MDMO-PPV:$PC_{61}BM$ 1:1, the PL intensity shifts by less than 2.0 %.

In any case, regarding the high observed CTE PL quenching for blend systems of close to 100 %, even a laser induced PL shift of 0.2 % has a minor impact on the actual PL(F) experiment. Moreover, since the graphs in Figure 5.4 show both a decrease and an increase of PL intensity with time, a sample degradation solely due to laser irradiation can be excluded.

Voltage Induced Sample Degradation

With the aim of elucidating the effects of an externally applied voltage on sample degradation, MDMO-PPV and MDMO-PPV:$PC_{61}BM$ 1:1 samples were first exposed to 30 s to 35 s of laser irradiation and the corresponding PL intensity was recorded. Then, without illumination of the samples, an increasing voltage starting at 0 V and rising to -10 V or -20 V was applied, following the usual PL(F) measurement routine. Subsequently, the PL intensity was detected again without any externally applied voltage. The results of these investigations are shown in Figure 5.5.

For both MDMO-PPV and MDMO-PPV:$PC_{61}BM$ 1:1, the observed maximal PL intensity variations of 0.3 % and 0.1 % are in the range of the laser intensity instability and can therefore not be attributed to the intermediate application of an external voltage. Moreover, since both a PL decrease and a PL increase is observed in the case of neat MDMO-PPV, no sample degradation due to the externally applied voltage takes place.

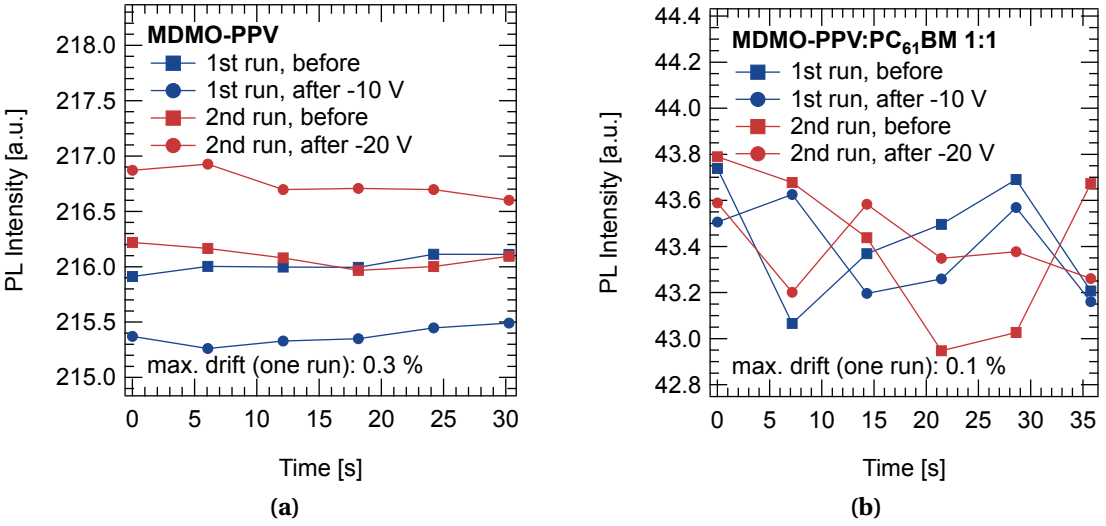

Figure 5.5: Investigation of the sample degradation due to the application of an external voltage. The PL intensity variation was detected before and after applying -10 V and -20 V. **(a)** For neat MDMO-PPV, the maximal PL intensity drift before and after voltage application is 0.3 %. **(b)** For MDMO-PPV:$PC_{61}BM$ 1:1, this value is 0.1 %.

Apparently, neither the laser irradiation of the samples nor the application of an external voltage have impairing effects on the PL emission of the samples when regarded separately. Thus, the prerequisites for a reliable conduction of PL(F) experiments, demanding the exposure of the samples to both laser light and voltage, are met.

5.1.4 Influence of Injection

Another possible factor influencing the PL(F) measurements which has to be taken into account is injection of charge carriers due to the applied voltage. An impact of injected charge carriers on field dependent PL quenching has already been reported in literature [136, 139, 140]. Here, an observed higher PL quenching in forward bias than in reverse bias direction was attributed to interactions between injected charge carriers and photogenerated excitons, leading to a decrease in the PL signal. Indeed, it has long been known that polarons may act as non-radiative singlet exciton quenching centers [141, 142, 143]. An increase in PL quenching with increasing current flow might also be explained by Joule heating of the sample [136]. On the other hand, it should also be considered that — just as in OLED devices — the injected charge carriers can radiatively recombine with each other, emitting EL at similar wavelengths as the observed PL. This would lead to an increase in the overall blend emission and a decrease of the observed field dependent quenching. However, as already mentioned in Section 5.1.1, EL is not detected in excitation modulation measurements since it is not modulated

with the same frequency as the PL signal. In any case, it is necessary to limit possible effects of charge carrier injection.

In a first attempt to minimize injection itself, a different sample structure was utilized with the active layers being sandwiched between two insulating layers of poly(methyl methacrylate) (PMMA), i.e., with a device structure of glass — PMMA — active layer — PMMA — Ca/Al. PMMA is a transparent polymer also known as the trademark Plexiglas which conveniently possesses a dielectric constant comparable to the ones of organic semiconductors [144, 145]. The PMMA was solved in n-butyl acetate and processed via spin-casting and subsequent annealing at 180 °C. The resulting film thicknesses were in the range of 200 nm to 400 nm, demanding high applied voltages exceeding 100 V in PL(F) experiments in order to reach the required electric field strengths for exciton dissociation. Although the PMMA layers succeeded in reducing the injection current to the nA regime for both forward and reverse bias direction, they also led to the formation of space charge regions in the device, distorting the applied electric field. Thus, waiting times for the decharging of the samples of up to 5 minutes between two measurement points had to be introduced in order to produce reliable results. For these reasons, the PMMA samples were replaced with standard solar cell devices as described in Section 4.3. For these samples, an external voltage was always applied in reverse bias direction, limiting injection to the range of μA to mA.

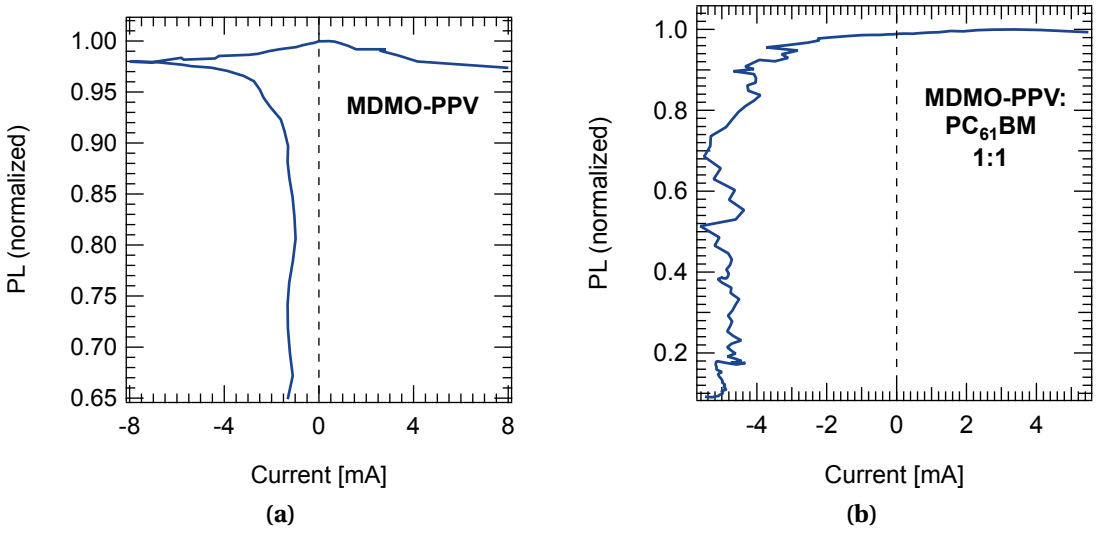

Figure 5.6: PL quenching in dependence of the current flow in forward and reverse bias direction. **(a)** For neat MDMO-PPV, the PL quenching for a current magnitude of 3 mA in forward and reverse bias direction amounts to 1 % and 35 %, respectively. **(b)** For MDMO-PPV:$PC_{61}BM$ 1:1, a PL quenching of 1 % is detected for a current flow of 5 mA in forward bias direction, while for -5 mA in reverse bias direction, the PL quenching reaches 91 %.

The influence of injection on field dependent PL quenching was investigated by simultaneously recording the PL signal and the current flow (using the SMU) in forward and reverse bias direction. By plotting the field dependent PL versus the current instead of the voltage (see Figure 5.6), the impact of injection on PL quenching can directly be extracted from the comparison between the forward and reverse bias PL signals. In an exemplary sample of neat MDMO-PPV (Figure 5.6a), for a current of 3 mA in forward bias direction, a PL quenching of only 1 % is detected, while for a similar current of -3 mA in reverse bias direction, the PL was quenched by up to 35 %. A similar and even more notable observation is made for a MDMO-PPV:$PC_{61}BM$ 1:1 device (Figure 5.6b): Here, a 1 % PL quenching occurs for a forward bias current of 5 mA, while the PL quenching for a reverse bias current of -5 mA even amounts to 91 %. Even if these observations cannot fully rule out the influence of injection on PL quenching, they demonstrate that the extent of such an influence is marginal and can be neglected with regard to the high PL quenching ratios measured in reverse bias direction. Thus, the observed PL quenching in this thesis can actually be attributed to the applied electric fields.

5.2 Field Dependent Transient Absorption – TA(F)

While the PL(F) experiments monitor the decreasing recombination of singlet excitons or CTE with an increasing applied external electric field, the TA(F) technique directly probes polarons whose generation is enhanced by the increasing field dependent dissociation of the respective exciton species.
The origins of field independent transient absorption (TA) date back to the time around 1950 when George Porter invented an experimental method called flash photolysis for the detection of short-lived molecular species [146]. It was soon taken to the nanosecond regime with the invention and further development of lasers [147, 148] — a timescale which is also appropriate for the investigation of polarons in MDMO-PPV:$PC_{61}BM$ blends [149]. In general, TA is a pump–probe technique based on two different light sources:

- A short, intense laser pulse (the so-called pump) is used to induce electronically excited, absorbing species in the sample.
- Meanwhile, a beam of continuous, less energetic light (i.e., the probe) is sent through the sample, being partially absorbed by the excited species which are taken to higher excited states.

For a TA measurement, the time-resolved transmission of the probe light is detected. Prior to sample irradiation with the pump pulse, the probe passes the sample almost

without being attenuated. The pump pulse, which possesses a center wavelength close to the absorption maximum of the used donor material, then generates excited species such as singlet excitons, CTE or polarons with characteristic absorption spectra. These excited species can absorb the probe light, leading to a reduction of its transmission. Over time, the pump pulse induced sample excitations recombine, resulting in a gradual decrease in probe light absorption and thus in its attenuation until the initial transmission strength is restored (see Figure 5.7). The time-resolved monitoring of the probe light transmission yields information on the decay dynamics and lifetimes of the excited species. Also, the initial magnitude of the recorded transients right after pump pulse excitation can be seen as a measure of the excited species generation process.

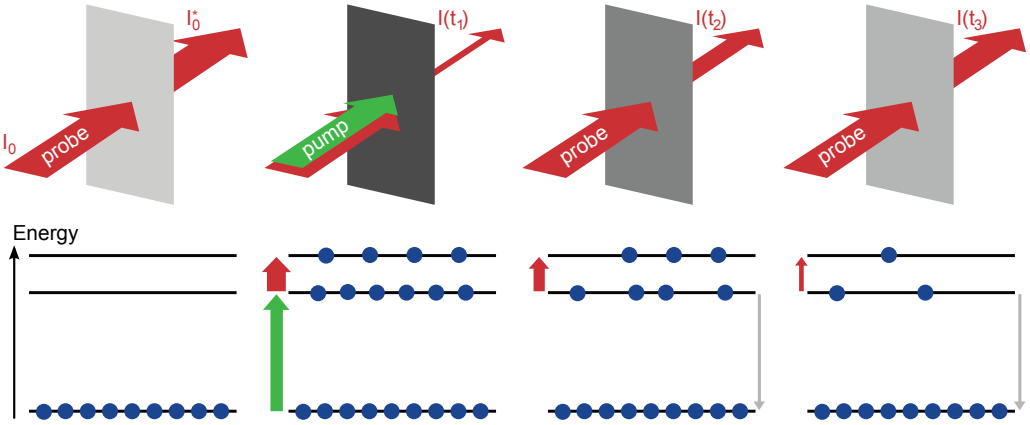

Figure 5.7: Schematic drawing of the TA measurement principle. Prior to pump pulse excitation, the sample is almost transparent to the probe light, leading to the almost unattenuated transmission of the latter. Sample irradiation with the pump pulse induces excited species which can absorb the probe light and are lifted to higher excited states. As a result, the probe light transmission is reduced. Gradually, the pump pulse induced excited species recombine, leading to the recovery of the initial probe light transmission value. Thus, information on the decay dynamics of the excited species can be gained (adopted from [150]).

As already mentioned, the investigated physical parameter in TA experiments is the transmittance T which is defined as the ratio of the transmitted to the incident light intensity I and I_0. According to the Beer-Lambert law, light passing through a sample experiences an exponential attenuation [151]:

$$T = \frac{I}{I_0} = \mathrm{e}^{-\alpha d}. \tag{5.2}$$

Here, α is the absorption coefficient of the material and d is the optical path length. The relative change of transmittance for a pump-pulse-excited sample with respect to a non-excited sample can be expressed as [150]

$$\frac{\Delta T}{T} = \frac{I}{I_0^*} - 1 \tag{5.3}$$

where I_0^* is the transmitted light intensity for the non-excited sample (see Figure 5.7). It should be noted that Equation 5.3 is independent of the incident light intensity I_0 so that $\frac{\Delta T}{T}$ can be easily extracted from a TA experiment. Naturally, the transmittance T is related to the absorbance of the sample, which is also known as optical density OD [150]:

$$OD = \log_{10}\left(\frac{1}{T}\right) = -\log_{10}\left(\frac{I}{I_0}\right). \tag{5.4}$$

The change in optical density for an excited versus a non-excited sample is given by [150]

$$\Delta OD = \log_{10}\left(\frac{I_0^*}{I_0}\right) - \log_{10}\left(\frac{I}{I_0}\right) = \log_{10}\left(\frac{I_0^*}{I}\right) \tag{5.5}$$

and can be related to the relative change of transmittance via [150]

$$\Delta OD \approx \frac{1}{\ln(10)} \cdot \left(-\frac{\Delta T}{T}\right). \tag{5.6}$$

According to the Beer-Lambert law, the optical density is proportional to the density of absorbing species n [152]:

$$OD = \frac{1}{\ln(10)} \cdot \sigma n d. \tag{5.7}$$

Here, σ is the absorption cross section of the photogenerated species. Thus, a change in the optical density ΔOD is directly related to a change in the density n of the investigated singlet excitons, CTE or polarons.

While TA measurements are commonly applied for the investigation of the decay dynamics of various excited species, the focus of the presented work was set on the field dependent generation process of polarons via intermediate CTE. Hence, the TA experiments were conducted in the presence of a variable external electric field. For these field dependent TA(F) measurements, transients were recorded for each chosen voltage starting at V_{oc} (i.e., the field-free case) and extending to higher voltages in reverse bias direction. The first few nanoseconds after excitation of the transients then reflect the charge carriers generated under the influence of the applied electric field.

5.2.1 Experimental Setup

The experimental setup used for TA(F) measurements is schematically depicted in Figure 5.8. Similar to PL(F) measurements, the samples were placed on the mounting plate of a second Janis ST-100 cold finger cryostat and connected to the electrical contacts. Again, the experiments reported in this thesis were conducted at room temperature and under dynamic vacuum in order to limit sample degradation.

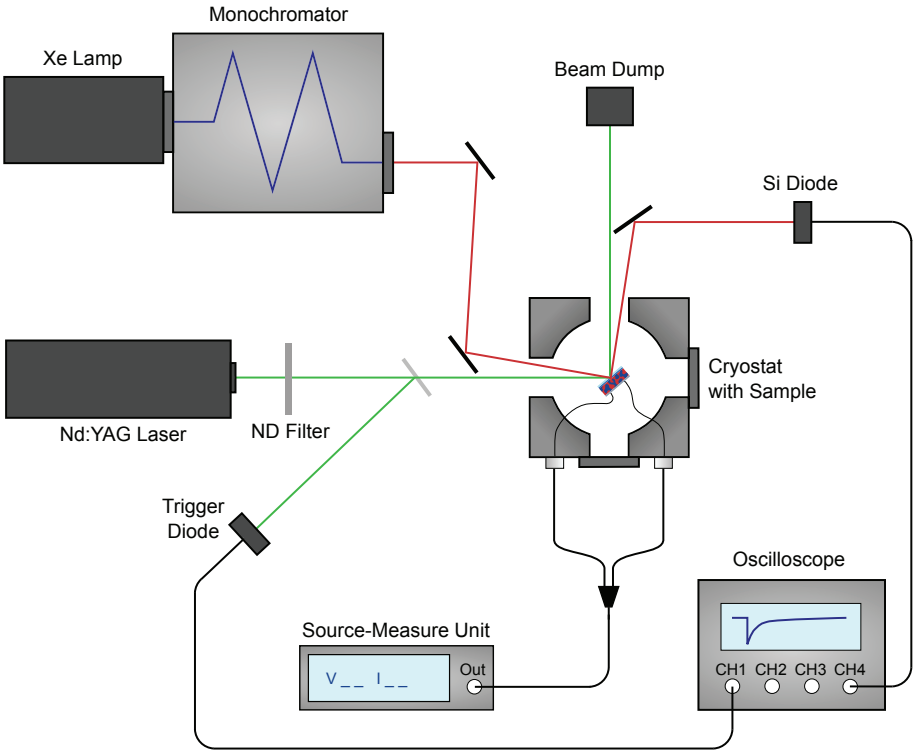

Figure 5.8: Experimental setup for TA(F) measurements. As pump pulse, a 7 ns FWHM Nd:YAG laser was used with a center wavelength of 532 nm. The probe light was provided by a Xe lamp whose output was sent through a monochromator, yielding continuous light at 917 nm for probing the positive polarons on MDMO-PPV. For data acquisition, a fast Si diode in combination with a digital oscilloscope was employed.

The pump pulses were provided by a Spectra-Physics Quanta-Ray INDI pulsed neodymium-doped yttrium aluminum garnet (Nd:YAG) laser, characterized by a full-width half-maximum (FWHM) pulse duration of 7 ns and a maximum repetition rate of 21.3 Hz. This laser possesses a fundamental wavelength of 1064 nm which was frequency-doubled by an integrated second harmonic generator to the output center wavelength of 532 nm. The original pulse energy of 105 mJ was attenuated to about 0.8 mJ by reflection on a glass plate, a pin hole and various ND filters. Moreover, an easily adjustable reduction of the pulse energy was achieved with a motorized ND filter wheel. The maximal used fluence for TA(F) experiments was set to 28 $\mu J/cm^2$ per

pulse. The pump pulses were focused onto the sample, inducing excited species in the MDMO-PPV:fullerene derivative blend system.

The probe light was brought to a spatial overlap with the pump pulses. Here, special care was taken with the alignment of the probe light, making sure that only the pump excited area of the sample was irradiated. For the probe light, the output of a Photon Technology International A-1010B 100 W Xe arc lamp was sent through an AMKO LTI monochromator with a wavelength range of 500 nm to 1000 nm. Since for the blend systems studied in this thesis, the excited species of interest for TA(F) measurements are the polarons residing on MDMO-PPV chains, the corresponding probe wavelength had to be determined. This was accomplished by recording an exemplary steady-state photoinduced absorption (PIA) spectrum of MDMO-PPV:$PC_{61}BM$ 1:1. The PIA principle is similar to the one of TA and mainly differs in the spectral instead of the temporal resolution of the detected probe light transmission. The PIA spectrum shown in Figure 5.9 was basically recorded with the PL(F) setup described in Section 5.1.2, extended by a LOT-Oriel tungsten halogen lamp providing the probe light. A detailed description of the PIA setup and the measurement routine can be found in the dissertation of Moritz Liedtke [153]. In Figure 5.9, the higher energetic peak in the PIA spectrum of MDMO-PPV:$PC_{61}BM$ 1:1 can be attributed to positive polarons on MDMO-PPV [149]. Thus, a probe light wavelength of 917 nm was chosen which is in the vicinity of the peak maximum.

The probe light transmission was recorded in reflection, using the Ca/Al contacts as mirror and thus passing the sample twice. It was then detected with a fast Femto HCA-S-400M-SI Si photodiode with an adapted micro lens for better light incoupling, an integrated preamplifier, a rise time of 1 ns and a frequency response of up to 400 MHz. Data acquisition was achieved with a Tektronix TDS 3034 four-channel digital oscilloscope which was triggered with the laser pulse frequency. Similar to PL(F) measurements, a Keithley 237 SMU was used for the application of external voltages in reverse bias direction.

The described experimental setup — which was addressed via LabVIEW and which is described in more detail in the diploma thesis of Clemens Grünewald [154] — was limited in its temporal resolution by the pulse width of the laser of 7 ns. Since single-shot experiments expressed a high SNR, the data recorded for several shots were averaged. An internal averaging of the oscilloscope comprised 512 laser pulses, and a subsequent external averaging over four sequences via LabVIEW resulted in a total number of 2048 averaged shots per data point. The processing of the recorded data is briefly described in the following section.

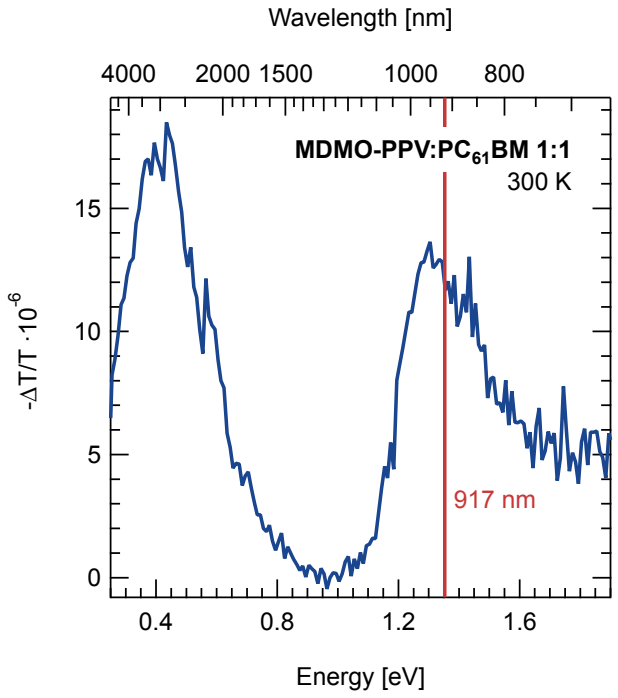

Figure 5.9: PIA spectrum of MDMO-PPV:PC_{61}BM 1:1, recorded at room temperature. The higher energetic peak is attributed to positive polarons on MDMO-PPV polymer chains [149]. For TA measurements, a probe wavelength of 917 nm was chosen.

5.2.2 Signal Processing

For the signal processing of TA experiments, an IGOR Pro procedure was employed which was originally developed by Matthias Gunz [155] and later modified by Andreas Kämpgen [150] and Clemens Grünewald [154]. The respective references also give a detailed description of the processing routine.

First of all, the TA data were corrected for PL or pump laser contributions. This was achieved by making an additional measurement without probe light (i.e., just with pump pulse excitation) for each recorded TA measurement and subtracting it from the TA data. Next, the initial probe light transmission I_0^* had to be determined. The oscilloscope, which was triggered on the pump pulses, sets the origin of its time axis at 10 % of its total temporal measurement range. The roughly 40 µs before this zero point which coincides with the pump pulse excitation were integrated and represent the value of I_0^*. Afterwards, the data points of the transients which are uniformly distributed on a linear time scale were converted to an approximately uniform distribution on a logarithmic scale. For this conversion, which also included a strong reduction of the data points from a number of about 900000 to about 1000, a polynomial smoothing algorithm [150, 154, 155] was used which also led to a significant improvement of the SNR. Subsequently, the change of optical density ΔOD was calculated from the transmis-

sion intensity data I_0^* and I, using Equation 5.5. The resulting transients comprised about two orders of magnitude in the reduction of charge carriers and four to six orders of magnitude in their temporal extent. While these transients may be used for the extraction of the charge carrier density n or for the evaluation of the recombination dynamics, for the TA(F) measurements reported in this thesis, they were merely applied for the determination of charge carrier generation. Each of the transients recorded for one specific electric field strength was integrated over the first 20 ns after excitation, yielding a parameter termed $\Delta OD_0(F)$. As a prerequisite for this operation, it had to be verified that the transients did not differ in their recombination behavior over those first 20 ns after excitation. The parameter $\Delta OD_0(F)$ then reflects the number of polarons which are initially generated for a specific electric field and can be used for a comparison to the CTE dissociation monitored via PL(F) measurements.

5.3 Auxiliary Methods

In order to interpret the results obtained from PL(F) and TA(F) measurements in terms of morphology, two auxiliary experimental techniques were employed for the investigation of the blend morphologies. The surface of the blends was characterized via AFM while both bulk and surface of the blends were addressed by ODMR. The subsequent description of the latter technique is mainly based on the diploma thesis of Stefan Väth [156] and the dissertation of Andreas Sperlich [157] on this subject.

5.3.1 Atomic Force Microscopy (AFM)

Originally developed in 1986 [158], AFM is a special scanning probe microscopy technique for investigating sample surfaces with a resolution down to the nanometer range which is much lower than the diffraction limit. It is based on the deflection of a cantilever due to the forces between the cantilever tip and a nearby surface. In this way, the surface height and other parameters such as the material stiffness can be monitored. AFM images shown in this thesis were provided by Franziska Fuchs, PhD student at Experimental Physics VI. For the measurements, a Veeco Dimension Icon system was employed in tapping mode, using a tapping mode etched silicon probe tip. The obtained height and phase images clearly reflect the presence or absence of phase segregation between donor and acceptor in the studied blends.

5.3.2 Optically Detected Magnetic Resonance (ODMR)

ODMR is a spin-sensitive experimental technique based on electron spin resonance (ESR). First observed in 1944 [159], ESR is used for the characterization of electronic states in various materials. It exploits the Zeeman effect, i.e., the energy splitting of electronic states observed for an externally applied magnetic field. For instance, triplet excitons with a total spin of $S = 1$ split into three distinct Zeeman levels with the spin quantum numbers $m_s = \pm 1$ and $m_s = 0$. Moreover, dipole–dipole interactions between the magnetic moments of adjacent spins may result in an additional energy splitting known as zero field splitting which is partially described by the zero field interaction parameter D. For $D = 0$, all three Zeeman levels are degenerate for zero magnetic field conditions while for $D \neq 0$, the degeneracy between the $m_s = 0$ and $m_s = \pm 1$ states is revoked even without the application of a magnetic field. If the described system is now irradiated with resonant microwaves, spin flips are induced between the different spin states which can be observed as microwave absorption when sweeping the magnetic field. While ESR monitors a change in the microwave absorption, ODMR detects a change in an optical transition which is related to the ESR induced spin flips, allowing for a higher sensitivity due to the easier detection of photons in the visible range as compared to the microwave range. For this thesis, the relative change in PL was recorded; hence, the experimental method is also referred to as photoluminescence detected magnetic resonance (PLDMR). The emergence of an exemplary ODMR spectrum displaying the change in photoluminescence ΔPL normalized to the total PL intensity is illustrated in Figure 5.10.

The central feature of the spectrum exhibiting the highest signal intensity can be ascribed to triplets with a high degree of delocalization for which no significant zero field splitting occurs, i.e., $D \approx 0$. Thus, the transitions with $\Delta m_s = 1$ are observed at the same magnetic field strength. The resulting central peak is enclosed by two symmetrical, less intense spectral features attributed to $\Delta m_s = 1$ transitions of more localized triplets which experience a zero field splitting $D > 0$. Together with the central peak, these features are called full field signal. In addition, a weaker feature emerges at lower magnetic fields which is due to the $\Delta m_s = 2$ transition, actually being first-order spin-forbidden but nonetheless experimentally observed. Since this peak is detected at half the magnetic field strength of the central feature of the full field signal, it is termed half field signal. As for triplet excitons localized in different organic semiconductors, the spectral positions and shapes of the respective half field signals differ, this spectral feature is used in this thesis for the detection of triplets in MDMO-PPV:fullerene derivative blends. The occurrence or non-occurrence of the characteristic half field features helps to infer morphological information concerning the phase segregation in

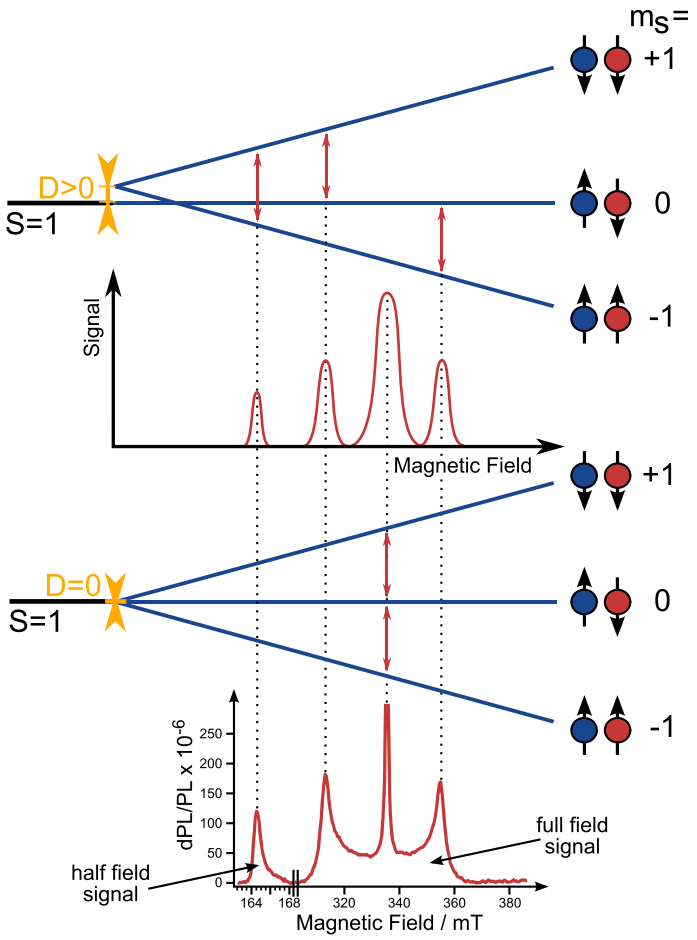

Figure 5.10: Illustration of the origins of an ODMR spectrum. The bottom graph represents an exemplary ODMR spectrum. The three peaks at the higher magnetic field side of the spectrum constitute the full field signal. They are attributed to $\Delta m_s = 1$ transitions for localized ($D > 0$) and strongly delocalized ($D \approx 0$) triplets. The feature at the lower magnetic side of the spectrum is termed half field signal and is used in this thesis for the investigation of triplets in various MDMO-PPV:$PC_{61}BM$ blends (graphics courtesy of Stefan Väth).

the blends: An efficient quenching of the triplet excitons is an indication of good intermixing between donor and acceptor while a lack thereof is regarded as proof of phase segregation instead.

The ODMR experiments shown in this thesis were conducted by Hannes Kraus, PhD student at Experimental Physics VI. For sample preparation, 3 mm × 10 mm Herasil substrates were spin-coated with the respective active layers and inserted into a quartz glass sample tube which was sealed under 20 mbar He atmosphere. These samples were placed in an Oxford Instruments ESR900 helium-flow cryostat, cooling to 5 K as set by a Lakeshore 330 temperature controller. ODMR spectra were recorded with a customized Bruker 200D spectrometer, providing microwaves in the X-band region

(8 GHz to 12 GHz, $\lambda \approx 3$ cm). The cryostat was surrounded by a Bruker ER4104OR X-band 9.43 GHz resonant microwave cavity and could be exposed to external magnetic fields of up to 0.7 T via an electromagnet. Optical excitation was achieved with a Cobolt Samba DPSS laser providing 532 nm cw light while spin transitions were induced by microwaves generated and transistor-transistor-logic-modulated by a Wiltron 69137A frequency synthesizer with amplifier, reaching an incident power of 0.5 W on the cavity. This resonant microwave irradiation caused a variation of the PL intensity, which was reconstructed by an Ametek Signal Recovery 7265 DSP lock-in amplifier from the integral PL, measured from 600 nm onwards by a Si photodiode and preamplified by a Femto DLPCA transimpedance amplifier. For a more in-depth description of the ODMR setup and the experimental technique in general, References [156] and [157] may be consulted.

6 Exciton Binding Energies

One of the key factors determining the efficiency of charge carrier photogeneration in organic BHJ solar cells is given by the Coulomb binding energy of the interfacial CTE. Its magnitude is generally assumed to be smaller in comparison to the binding energy of singlet excitons, representing the primary photoexcitations in OPV devices. However, the determination of singlet exciton or CTE binding energies leads to somewhat ambiguous results since the disorder characterizing organic semiconductors prevents the binding energies from being well-defined [59]. Concerning the singlet excitons in various PPV derivatives, their binding energies have been confined to $E_{b,S1} \leq 400$ meV by several experimental and theoretical approaches [160, 161, 162, 163] while reports for CTE binding energies in different donor–acceptor systems vary in the range of 100 meV $< E_{b,CTE} <$ 500 meV [59]. In particular, the CTE binding energy in a MDMO-PPV:$PC_{61}BM$ 1:1 blend has recently been determined as 130 meV by Hallermann et al. [98]. However, this value seems to be based on the assumption of an unrealistically high relative dielectric constant of $\epsilon_r = 5.9$, exceeding even the literature value of $\epsilon_r = 3.9$ for neat $PC_{61}BM$ [129]. In this context, the objective of the presented work is to provide a reliable value for the binding energy of the CTE in MDMO-PPV:$PC_{61}BM$ 1:1 and to compare it to the one of the singlet exciton in neat MDMO-PPV. This is achieved by monitoring the field dependence of the respective PL emission via both excitation modulated and voltage modulated PL(F). The obtained experimental data are related to the calculations of the Onsager–Braun theory, testing the model for its applicability and yielding quantitative results for the binding energies.

6.1 Binding Energies as Obtained via Excitation Modulation

Prior to the conduction of the actual PL(F) experiments, the PL spectra of neat MDMO-PPV, neat $PC_{61}BM$ and a blend of the two materials in the best OPV performing ratio of 1:4 were recorded (see Figure 6.1). While the singlet exciton PL of MDMO-PPV reaches its maximum at about 590 nm, the $PC_{61}BM$ spectrum is characterized by a peak at about 740 nm, followed by a tail extending into the infrared region. Upon blending the

two materials, their singlet exciton emission is quenched by several orders of magnitude (not shown here). However, signatures of the respective blend components are still clearly visible in the 1:4 blend spectrum as residual emission from neat material domains within the blend system.

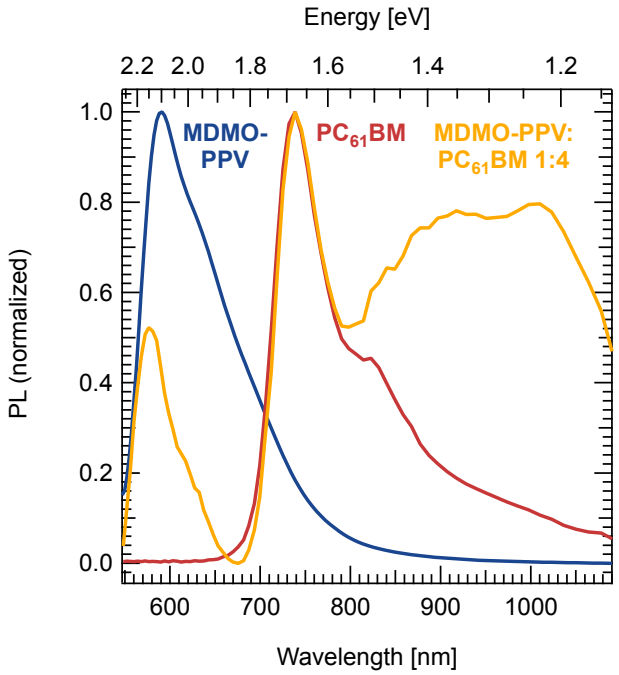

Figure 6.1: Normalized PL spectra of neat MDMO-PPV, neat $PC_{61}BM$ and a 1:4 blend of the two materials. The blend spectrum displays both signatures of the neat materials and a new feature emerging at higher wavelengths which is ascribed to radiative CTE recombination.

In addition, a new feature emerges at higher wavelengths in the blend spectrum which is not apparent in any of the neat material spectra and can be attributed to CTE emission [98]. The CTE PL expresses a significant spectral overlap with the tail of the residual $PC_{61}BM$ emission. Thus, for the conduction of PL(F) experiments, the influence of an applied electric field on the residual $PC_{61}BM$ PL has to be examined in order to allow for a quantitative analyzation of the field dependent CTE PL quenching. For this reason, spectrally reduced blend spectra have been recorded while applying an external voltage in reverse bias direction. As can be seen in Figure 6.2, an increasing voltage not only quenches the CTE PL, but also influences the $PC_{61}BM$ emission in the blend. This means that in PL(F) experiments, the residual $PC_{61}BM$ PL cannot simply be subtracted as a constant offset, making it harder to correctly evaluate the field dependence of the CTE emission.

Consequently, another blend ratio with a reduced $PC_{61}BM$ content was employed for the field dependent CTE investigations. For the chosen blend ratio of 1:1, the blend

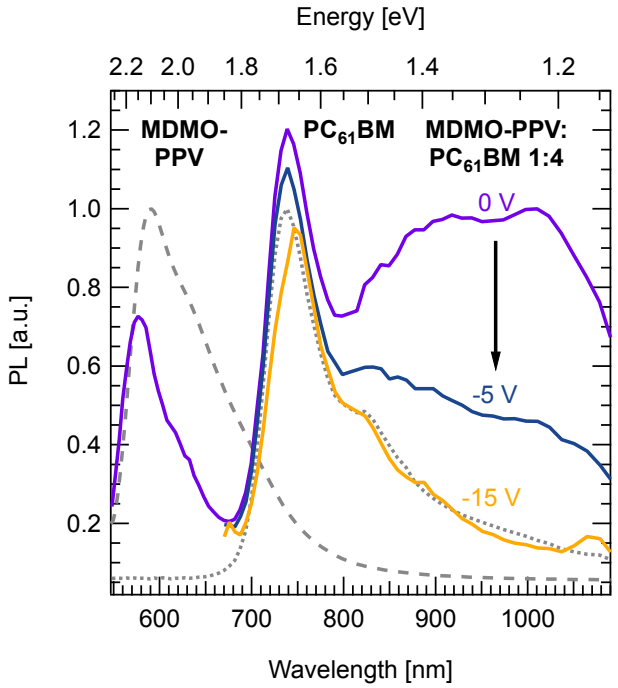

Figure 6.2: Evolution of the MDMO-PPV:$PC_{61}BM$ 1:4 PL spectrum for externally applied voltages. The PL spectra of the neat donor and acceptor materials are depicted by the dashed and the dotted curves, respectively. An increase of the external voltage in reverse bias direction quenches the CTE PL, but also alters the residual $PC_{61}BM$ emission.

spectrum does not show any PL contribution from $PC_{61}BM$ phases (see Figure 6.3). Moreover, for the application of an increasing voltage in reverse bias direction, the CTE emission is reduced uniformly, allowing for the integral detection of the CTE starting at a wavelength of 800 nm (yellow background in Figure 6.3). For the field dependent examination of the singlet exciton in neat MDMO-PPV, the respective PL is also recorded integrally, but with a cut-on wavelength of 550 nm.

Exemplary integral, excitation modulated measurements of the voltage dependent PL in MDMO-PPV and MDMO-PPV:$PC_{61}BM$ 1:1 can be seen in Figures 6.4a and 6.4c, respectively. The curves show the expected progression, with the maximal PL signal being detected without applied voltage and a decreasing signal intensity for higher voltages in reverse direction. From these curves, the field dependent PL quenching is calculated with Equation 5.1. In the examples shown in Figures 6.4b and 6.4d, the field dependent quenching amounts to more than 80 % for both MDMO-PPV and MDMO-PPV:$PC_{61}BM$ 1:1. Yet, for some of the investigated blend samples, even higher CTE PL quenching values of close to 100 % were reached (not shown here). These high quenching ratios are essential in order to achieve valid results for the binding energies in the subsequent comparison to the Onsager–Braun theory.

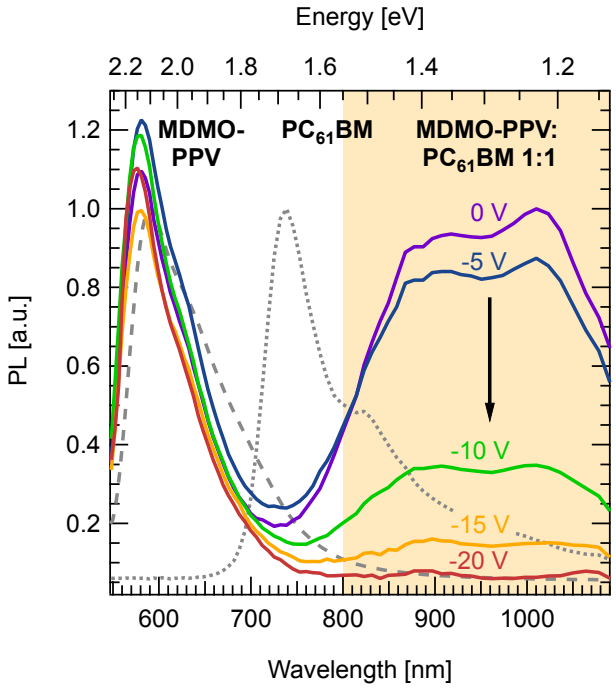

Figure 6.3: Voltage dependent PL spectra of a MDMO-PPV:$PC_{61}BM$ 1:1 blend. Here, no residual $PC_{61}BM$ PL is interfering with the CTE emission. Moreover, the CTE PL is quenched uniformly for increasing voltages in reverse bias direction, allowing for an integral detection in the spectral region indicated by the yellow background. Again, the spectra of neat MDMO-PPV and neat $PC_{61}BM$ are displayed by the dashed and by the dotted curve.

In order to determine the singlet exciton and CTE binding energies from the experimental data sets, the calculated quenching curves for MDMO-PPV and MDMO-PPV:$PC_{61}BM$ 1:1 were fitted with a fit function based on the Onsager–Braun model (see Section 3.3). For this purpose, reasonable assumptions had to be made for the input parameters T, ϵ_r and $\mu\tau$. While the temperature T was set to 297 K during the experiments, the literature value of $\epsilon_{r,PPV} = 3.0$ was used for the relative dielectric constant in MDMO-PPV [123]. With the literature value for $PC_{61}BM$, $\epsilon_{r,PCBM} = 3.9$ [129], an average relative dielectric constant of $\epsilon_r = 3.45$ was assumed for the 1:1 blend system. However, for the $\mu\tau$-product, reliable literature values were either hard to find or strongly dependent on the experimental method applied for their determination. While the lifetime of singlet excitons is generally assumed to be in the nanosecond regime, for MDMO-PPV, it was experimentally determined as e.g. 0.36 ns by Offermans et al. [101]. As for the CTE in MDMO-PPV:$PC_{61}BM$ 1:1, no literature values for the CTE lifetime in this blend ratio could be found. Yet, based on the reported values for other blend systems [57, 65, 101], a CTE lifetime of 1 ns was assumed. Concerning the charge carrier mobilities, either global, macroscopic values as determined by e.g. time-of-flight (TOF) or photoinduced charge extraction by linearly increasing voltage (photo-CELIV)

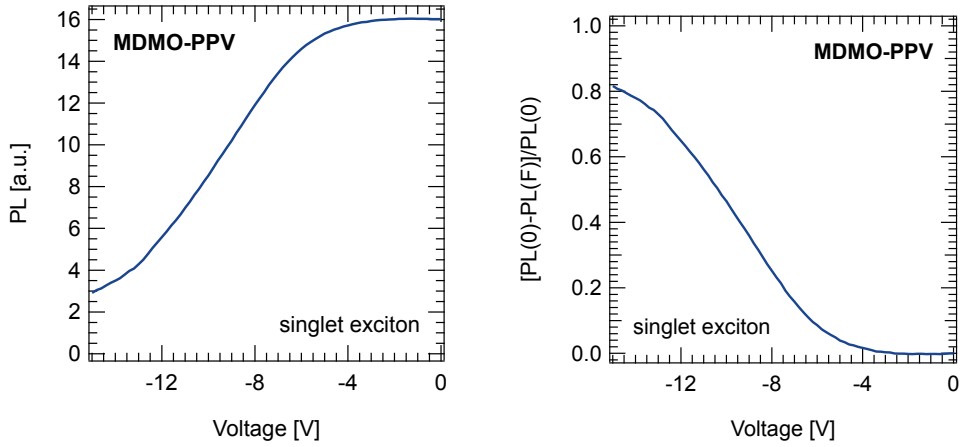

(a) PL(F) for MDMO-PPV.

(b) Quenching for MDMO-PPV.

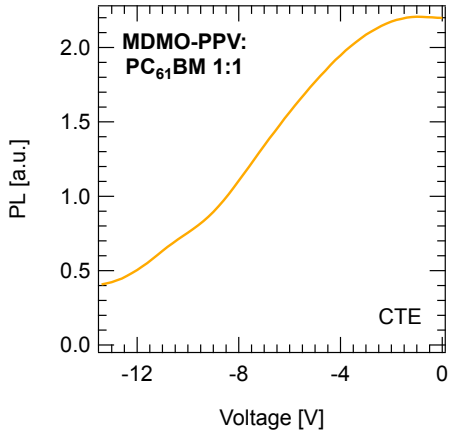

(c) PL(F) for MDMO-PPV:PC_{61}BM 1:1.

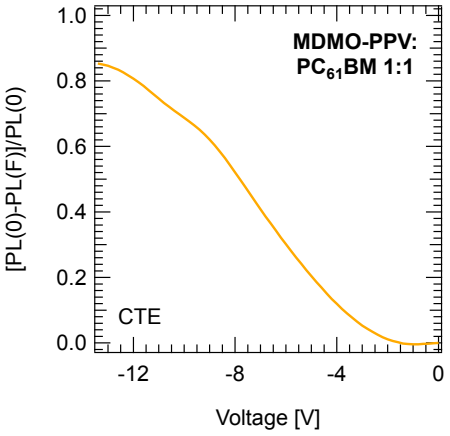

(d) Quenching for MDMO-PPV:PC_{61}BM 1:1.

Figure 6.4: PL(F) data and calculated quenching curves for neat MDMO-PPV and MDMO-PPV:PC_{61}BM 1:1. For the highest applied reverse voltages, the singlet exciton or CTE PL quenching exceeds 80 %. For several other MDMO-PPV:PC_{61}BM 1:1 samples, the field dependent quenching was even observed to be close to 100 %.

experiments or local, microscopic values originating from TRMC measurements may be used within the Onsager–Braun framework. In the case of neat MDMO-PPV, a global charge carrier mobility of about $3 \cdot 10^{-6}$ cm^2/Vs has been reported from photo-CELIV measurements [164], while the local hole mobility was found to be orders of magnitude higher, i.e., $1.8 \cdot 10^{-3}$ cm^2/Vs, as determined via TRMC [76, 165]. For blends of MDMO-PPV:PC$_{61}$BM 1:1, the global charge carrier mobility of e.g. $3 \cdot 10^{-4}$ cm^2/Vs [164] is of the same order of magnitude as the local one, which is reported to be in the range of 10^{-4} cm^2/Vs [76]. Since the investigated singlet excitons and CTE possess a more local than global character, the choice of local charge carrier mobilities seems appropriate for this thesis and has also been justified in literature [57, 93]. Moreover, it has to be noted that both the CTE lifetime and the charge carrier mobility are influenced by the application of an external electric field: While an increasing electric field leads to an enhanced mobility [67], the CTE lifetime is reduced at the same time [57]. Since the actual extent of the increase in mobility and the decrease in lifetime with increasing electric field cannot be correctly determined, a constant $\mu\tau$-product of $1 \cdot 10^{-17}$ m^2/V is assumed in this work for both neat MDMO-PPV and the blend of MDMO-PPV:PC$_{61}$BM 1:1. The limitations of this approach will be discussed in Section 6.3.

Figure 6.5 shows the comparison of the experimentally determined field induced singlet exciton PL quenching in neat MDMO-PPV (black open circles) with the theoretical Onsager–Braun dissociation probabilities (colored solid lines) which were calculated by using the above described parameters. Note that in contrast to Figure 6.4, the bottom axis now displays the electric field on a logarithmic scale. The different colors of the dissociation probabilities indicate different binding energies whose magnitudes are given in the graph. Among the different curves, the central one (green solid line) also represents the fit of the experimental data. The experimental error is given by the grey crosses and stems from the determination of the sample active layer thickness d. As d could only be determined with an accuracy of up to ± 15 nm, the conversion of the experimentally applied voltage V to the corresponding electric field F via $F = \frac{U}{d}$ is prone to an experimental error as well. This error was found to be larger than the deviation between multiple measurements and is thus used for indicating the absolute experimental error for all results reported in this chapter. As can be seen from Figure 6.5, the experimental results are in good agreement with the Onsager–Braun theory, allowing for the extraction of a Coulomb binding energy. However, since the dissociation of singlet excitons in neat conjugated polymers is a two-step process involving a polaron pair (see Figure 3.5b in Section 3.3), the extracted binding energy represents the energy needed for the dissociation of the singlet exciton into a polaron pair and thus yields a lower limit to the actual, larger singlet exciton binding energy which has to be

overcome for the dissociation to free charge carriers. The obtained value for the singlet exciton binding energy in neat MDMO-PPV as determined via excitation modulation amounts to $E_{b,S1,EM} \geq (327 \pm 30)$ meV, corresponding to an electron–hole distance of $a_{S1,EM} \leq (1.47 \pm 0.14)$ nm.

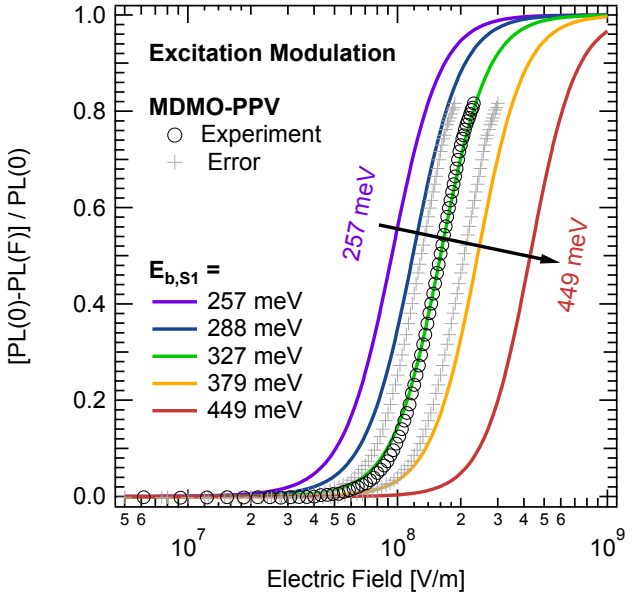

Figure 6.5: PL quenching yield for the singlet exciton emission of neat MDMO-PPV (black open circles) in comparison to the Onsager–Braun dissociation probability (colored solid lines). The experimental error is indicated by the grey crosses and originates from the inaccuracy in the determination of the active layer thickness. The extracted singlet-exciton-to-polaron-pair binding energy gives a lower limit to the actual singlet exciton binding energy which is given by $E_{b,S1,EM} \geq (327 \pm 30)$ meV.

In comparison, the experimentally determined field induced CTE PL quenching in MDMO-PPV:$PC_{61}BM$ 1:1 is shown in Figure 6.6. On first glance, it can already be seen that the field induced quenching takes place at much lower electric field strengths, indicating a reduced CTE binding energy. Similar to the case of the singlet exciton, the comparison of the CTE PL quenching to the Onsager–Braun calculations reveals a good accordance between experimental data and theoretical predictions. Thus, the CTE binding energy in MDMO-PPV:$PC_{61}BM$ 1:1 as determined via excitation modulation can be reported as $E_{b,CTE,EM} = (201 \pm 18)$ meV, being significantly smaller than $E_{b,S1,EM}$. This binding energy corresponds to an electron–hole distance of $a_{CTE,EM} = (2.07 \pm 0.21)$ nm. In order to validate the obtained results, similar experiments were conducted using voltage modulation, the results of which are reported in the subsequent section.

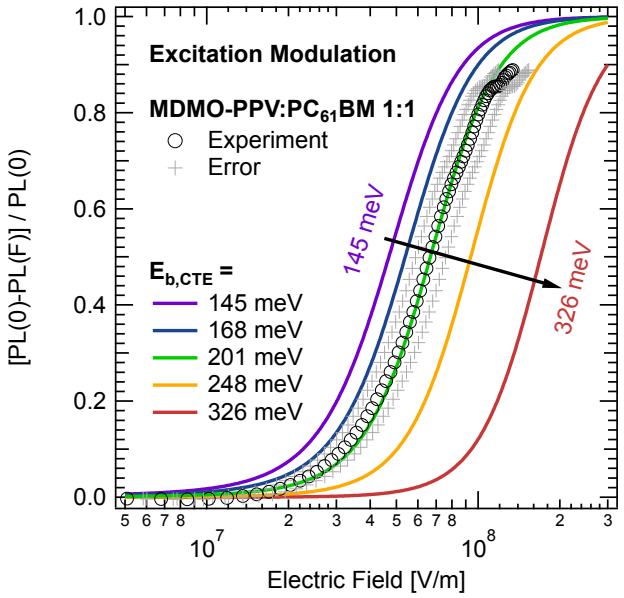

Figure 6.6: PL quenching yield for the CTE emission of MDMO-PPV:PC_{61}BM 1:1 (black open circles) in comparison to the Onsager–Braun dissociation probability (colored solid lines). The extracted value for the CTE binding energy is $E_{b,CTE,EM}$ = (201 ± 18) meV.

6.2 Comparison to Binding Energies Obtained via Voltage Modulation

As already described in Section 5.1.1, the voltage modulation measurement routine represents an alternative approach to the excitation modulation technique and should yield comparable results. Analogously to the presentation of the excitation modulation results, the field dependent singlet exciton PL quenching in neat MDMO-PPV as determined via voltage modulation is shown in Figure 6.7. Albeit consisting of fewer data points, the obtained PL quenching yield shows a similarly good agreement with the Onsager–Braun calculations as the excitation modulation data (see Figure 6.5). The lower limit of the singlet exciton binding energy in neat MDMO-PPV can be extracted as $E_{b,S1,VM} \geq (325 \pm 28)$ meV and thus validates the excitation modulation value of $E_{b,S1,EM} \geq (327 \pm 30)$ meV within the experimental error.

A similar observation is made for the case of the CTE PL quenching yield in MDMO-PPV:PC_{61}BM 1:1. Here, the comparison to the Onsager–Braun theory (see Figure 6.8) suggests a CTE binding energy of $E_{b,CTE,VM}$ = (207 ± 25) meV which is also in good agreement with the excitation modulation value of $E_{b,CTE,EM}$ = (201 ± 18) meV.

The apparent coincidence of the binding energies obtained by excitation modulation and voltage modulation measurements consolidates the reliability of the PL(F) method in general, making it a suitable tool for the determination of singlet exciton and CTE

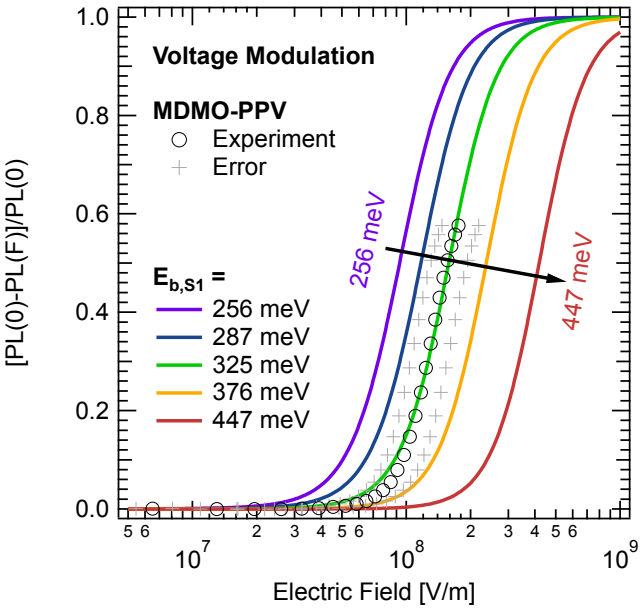

Figure 6.7: Voltage modulated PL quenching yield for the singlet exciton emission of neat MDMO-PPV (black open circles) in comparison to the Onsager–Braun dissociation probability (colored solid lines). The singlet exciton binding energy is determined as $E_{b,S1,VM} \geq (325 \pm 28)$ meV which is in good agreement to the value obtained via excitation modulation.

binding energies. Besides, the lack of a significant discrepancy between the PL quenching yields detected via the two different modulation techniques indicates that in the experiments, contributions of EL which might falsify the voltage modulation results are marginal and can be neglected. Nevertheless, due to the easier conduction of the excitation modulation experiments, this method is preferred for the subsequently reported experimental results in this thesis.

6.3 Discussion

The determined binding energies of the singlet exciton in neat MDMO-PPV and of the CTE in MDMO-PPV:$PC_{61}BM$ 1:1 are well within the range of the values reported in recent literature for comparable material systems [59, 160, 161, 162, 163]. As expected, the CTE binding energy $E_{b,CTE} \approx 201$ meV is found to be significantly reduced by at least 126 meV in comparison to the one of the singlet exciton in neat MDMO-PPV, $E_{b,S1} \approx 327$ meV. This reduction is indicative of a facilitated exciton dissociation process in the case of the CTE, supporting the notion that CTE are in fact involved in the charge carrier photogeneration process and might provide a favorable alternative to the direct dissociation of singlet excitons. Nevertheless, both $E_{b,CTE}$ and $E_{b,S1}$ are an order of magnitude higher than the thermal energy at room temperature of about

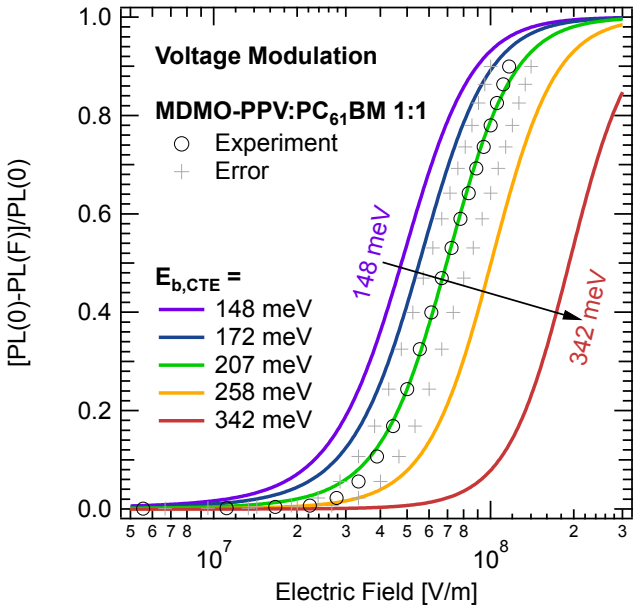

Figure 6.8: Voltage modulated PL quenching yield for the CTE emission of MDMO-PPV:PC_{61}BM 1:1 (black open circles) in comparison to the Onsager–Braun dissociation probability (colored solid lines). The extracted value for the CTE binding energy is $E_{b,CTE,VM}$ = (207±25) meV, validating the excitation modulation value within the experimental error.

25 meV, making thermally induced dissociation unfeasible and hinting at the existence of additional dissociation increasing effects such as a higher delocalization length [93], entropy effects [59] or relaxation processes in the disorder-broadened DOS [67]. The relatively high CTE binding energy also stresses the importance of a possible dissociation route via hot, less strongly bound CTS. Recent pump–push–probe experiments by Bakulin et al. [166], where relaxed CTS are re-excited by an infrared push pulse and thus given a second chance to dissociate, demonstrate that such hot CTS indeed make a significant contribution to the photocurrent. This observation is mainly ascribed to the higher hole delocalization for hot CTS as compared to relaxed CTS, resulting in a higher electron–hole distance and a consequently reduced CTE binding energy [166].

Coming back to speak of relaxed CTS, the here presented value of $E_{b,CTE}$ can also be used for a direct comparison to a recent publication employing the same experimental technique (PL(F)) on the same material system (MDMO-PPV:PC_{61}BM 1:1). In 2008, Hallermann et al. [98] reported a much smaller CTE binding energy of $E_{b,CTE,Hallermann}$ = 130 meV despite finding an only slightly different electron–hole distance of $a_{CTE,Hallermann}$ = 1.88 nm in comparison to $a_{CTE} \approx 2.07$ nm. The lower binding energy implies the assumption of an unrealistically high average relative dielectric constant of $\epsilon_{r,Hallermann} = 5.9$ instead of the value of $\epsilon_r = 3.45$ assumed in this thesis. Still, the authors claim to have used an average dielectric constant of 3. Be-

sides, the CTE PL quenching which is used for calculating $E_{b,CTE,Hallermann}$ with the Onsager model only reaches values of up to 35 %, being detrimental for an exact fitting of any theoretical model. Nevertheless, albeit not coinciding within the experimental error, both the CTE binding energy reported by Hallermann et al. and the CTE binding energy reported in this thesis are of a comparable magnitude and follow the same trend of being significantly smaller than the binding energy of the singlet exciton in MDMO-PPV.

As already indicated in Section 6.1, the most critical parameter in the calculation of the exciton binding energies via the Onsager–Braun formalism is the $\mu\tau$-product which was estimated as $1 \cdot 10^{-17}$ m^2/V. The influence of a variation of this value on the obtained binding energies shall be evaluated in the following. In the case of the singlet exciton in neat MDMO-PPV, a lifetime of 0.1 ns and a mobility of $1 \cdot 10^{-3}$ cm^2/Vs were assumed, representing the lower and upper limits of literature values, respectively. As for the upper limit of the $\mu\tau$-product, the lifetime might well be in the nanosecond regime. Thus, the highest reasonable $\mu\tau$-product is estimated as $1 \cdot 10^{-16}$ m^2/V. As for the lower limit, macroscopic mobilities in the range of 10^{-6} cm^2/Vs have been reported, which — in combination with a lifetime of 0.1 ns — would imply a $\mu\tau$-product of $1 \cdot 10^{-20}$ m^2/V. The respective singlet exciton binding energies for various $\mu\tau$-products within these limits are summarized in Table 6.1.

$\mu\tau$ [m^2/V]	$E_{b,S1}$ [meV]	$\Delta E_{b,S1}$ [meV]	$\Delta E_{b,S1}$ [%]
$1 \cdot 10^{-16}$	402	+75	23
$1 \cdot 10^{-17}$	**327**	**0**	**0**
$1 \cdot 10^{-18}$	246	-81	25
$1 \cdot 10^{-19}$	148	-179	55
$1 \cdot 10^{-20}$	76	-251	77

Table 6.1: Singlet exciton binding energies in neat MDMO-PPV for $\mu\tau$-products in the range of $1 \cdot 10^{-16}$ m^2/V to $1 \cdot 10^{-20}$ m^2/V. $\Delta E_{b,S1}$ [meV] gives the absolute deviation of $E_{b,S1}$ from the value obtained for a $\mu\tau$-product of $1 \cdot 10^{-17}$ m^2/V while $\Delta E_{b,S1}$ [%] represents the relative deviation.

Apparently, the results for the singlet exciton binding energies are strongly dependent on the choice of the $\mu\tau$-product. Reasonable values for the binding energies are only achieved for low $\mu\tau$-products between $1 \cdot 10^{-16}$ m^2/V and $1 \cdot 10^{-18}$ m^2/V and thus for relatively high mobility values. The necessity of using high mobilities for achieving plausible results is one of the most frequently criticized issues of the Onsager–Braun

model. However, in this special case, the use of high local mobilities is justified since the investigated process of exciton dissociation takes place on a more local than global scale. Still, by changing the $\mu\tau$-product by two orders of magnitude from $1 \cdot 10^{-16}$ m^2/V to $1 \cdot 10^{-18}$ m^2/V, $E_{b,S1}$ changes by 156 meV. This indicates that the error made in the calculations due to the uncertainty of the parameter $\mu\tau$ is much higher than the largest experimental error due to the determination of the active layer thicknesses.

Similar considerations can be made for the CTE in MDMO-PPV:PC_{61}BM 1:1. In this case, however, the variations between reported local and global mobilities are not as severe as for neat MDMO-PPV. Moreover, literature values for the CTE lifetime are missing altogether. Therefore, the influence of variations of the $\mu\tau$-product was only checked for the $\mu\tau$-range of $1 \cdot 10^{-16}$ m^2/V to $1 \cdot 10^{-18}$ m^2/V. The resulting CTE binding energies are listed in Table 6.2.

$\mu\tau$ [m^2/V]	$E_{b,CTE}$ [meV]	$\Delta E_{b,CTE}$ [meV]	$\Delta E_{b,CTE}$ [%]
$1 \cdot 10^{-16}$	288	+87	43
$1 \cdot 10^{-17}$	**201**	**0**	**0**
$1 \cdot 10^{-18}$	77	-124	62

Table 6.2: CTE binding energies in MDMO-PPV:PC_{61}BM 1:1 for $\mu\tau$-products in the range of $1 \cdot 10^{-16}$ m^2/V to $1 \cdot 10^{-18}$ m^2/V. $\Delta E_{b,CTE}$ [meV] gives the absolute deviation of $E_{b,CTE}$ from the value obtained for a $\mu\tau$-product of $1 \cdot 10^{-17}$ m^2/V while $\Delta E_{b,CTE}$ [%] represents the relative deviation.

Here, too, the CTE binding energies are strongly influenced by the choice of $\mu\tau$. Yet, from the reported literature values for the mobility and the lifetime of the CTE in other blend systems, the $\mu\tau$-product of $1 \cdot 10^{-17}$ m^2/V appears to be the most reasonable assumption in this case, reinforcing the significance of the obtained CTE binding energy $E_{b,CTE} \approx 201$ meV. Nevertheless, it should be noted that both the considerations for the singlet exciton in MDMO-PPV and for the CTE in MDMO-PPV:PC_{61}BM 1:1 do not include the field dependence of the $\mu\tau$-product. In order to take this influencing factor into account as well, modifications would have to be made to the Onsager–Braun model directly. As the actual extent of the field dependence of μ and τ is unknown, such modifications were not attempted for in this work.

Besides, it has to be noted that all singlet exciton and CTE binding energies reported within this thesis depend on the validity of the Onsager–Braun model which is used for their extraction from PL(F) experiments. Moreover, since the PL(F) method may only detect the radiative part of the singlet exciton and CTE recombination, non-radiative

recombination pathways cannot be accounted for but might potentially lead to slightly altered binding energies.

6.4 Conclusions

In summary, the PL(F) method was used for the determination of the singlet exciton binding energy in neat MDMO-PPV as well as for the CTE binding energy in MDMO-PPV:$PC_{61}BM$ 1:1. Deploying the excitation modulation technique, values of $E_{b,S1,EM} \geq (327 \pm 30)$ meV and $E_{b,CTE,EM} = (201 \pm 18)$ meV were obtained, suggesting a reduced CTE binding energy in comparison to the one of the singlet exciton. Simultaneously, the good description of the experimental results by the theoretical calculations via Onsager–Braun prove the applicability of this model for the description of singlet exciton and CTE dissociation processes. The obtained results were validated by measurements utilizing the voltage modulation technique, also being proof of the comparability of the two modifications of the PL(F) method. The obtained binding energies are in good agreement with literature values for comparable material systems. Moreover, the magnitude of the CTE binding energy in MDMO-PPV:$PC_{61}BM$ 1:1 seems to be more reliable than the value recently reported by Hallermann et al. [98] since it is based on more justifiable assumptions concerning the used parameters and higher CTE PL quenching yields. However, it has to be kept in mind that the reported binding energies are strongly dependent on the choice of the $\mu\tau$-product. Especially in the case of the singlet exciton binding energy in neat MDMO-PPV, the error made by the choice of $\mu\tau$ is probably much higher than the actual experimental error. Consequently, for the adaption of the PL(F) technique to other material systems, it is highly recommended to carefully choose the used data sets for both the exciton lifetime and the charge carrier mobility.

7 The Interplay of Morphology and Dielectric Constant

While the field dependence of charge carrier photogeneration and the related CTE binding energy have been evaluated for the specific case of a MDMO-PPV:$PC_{61}BM$ 1:1 blend in Chapter 6, the extent to which the obtained results can be applied for other MDMO-PPV:$PC_{61}BM$ blend compositions still remains unclear. The transition to higher fullerene contents is known to have a strong impact on the blend morphology [167, 168]. According to previous studies in MDMO-PPV:$PC_{61}BM$ blends, phase segregation of fullerene domains starts to occur at blend ratios of about 1:2 which might in turn influence the delocalization length and thus the binding energy of the interfacial CTE. Also, a higher $PC_{61}BM$ load might lead to a higher effective relative dielectric constant of the blend, increasing the screening of charges and thus effectively reducing the CTE binding energy. In recent literature, some of these considerations have already been addressed by Veldman et al. [57] who used blends of a fluorene copolymer and $PC_{61}BM$ in order to investigate the CTE behavior for different blend ratios and zero external electric field on the one hand and for a constant blend ratio and varying externally applied electric fields on the other hand. Here, this study is extended by evaluating the field dependence of charge carrier photogeneration via relaxed CTS for various MDMO-PPV:$PC_{61}BM$ blend ratios. Systematically increasing the blend fullerene content, PL(F) is used for investigating the radiative CTE recombination while TA(F) is applied to directly probe the generated charge carriers. Thus, a substantial shift in the onset of the field dependence of both CTE dissociation and polaron generation is unveiled. The origin of this changing field dependence is investigated via additional morphological studies comprising both AFM and ODMR measurements. Based on the unraveled blend morphologies, the impact of the effective dielectric constant and of the CTE delocalization on charge separation in the various blend compositions is discussed.

7.1 Field Dependent Charge Carrier Photogeneration for Different Blend Ratios

In the presented blend ratio dependent study, the field dependence of charge carrier photogeneration via CTS precursors is investigated with the help of two complementary experimental techniques: While the CTE PL in PL(F) experiments serves as a direct probe of the geminate recombination via relaxed CTS, TA(F) data yield information on charge carriers which are generated under the influence of the applied electric field in addition to those generated under zero field conditions. The experiments were conducted on MDMO-PPV:$PC_{61}BM$ compositions with 4:1, 2:1, 1:1, 1:2 and 1:4 blend ratios.

7.1.1 PL(F) Measurements

The PL spectra of all investigated MDMO-PPV:$PC_{61}BM$ blend ratios are displayed in Figure 7.1. For better comparison, all spectra are normalized to the residual PL emission of the MDMO-PPV singlet exciton.

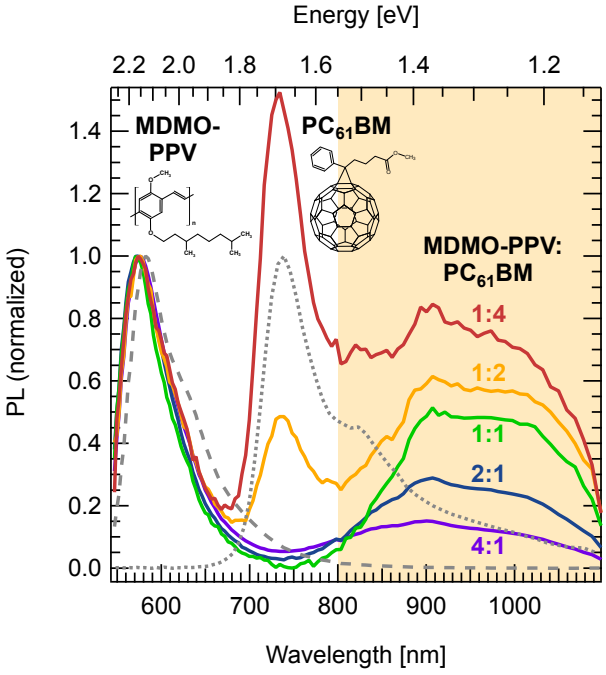

Figure 7.1: PL spectra of the investigated MDMO-PPV:$PC_{61}BM$ blend ratios of 4:1, 2:1, 1:1, 1:2 and 1:4. The neat material spectra are displayed by the dashed (MDMO-PPV) and the dotted ($PC_{61}BM$) curves, respectively. All spectra are normalized to the maximum of the singlet exciton emission of MDMO-PPV. The band at the lower energetic side of the spectra is ascribed to radiative CTE recombination. The spectral integration range for PL(F) experiments is indicated by the shaded background.

It should be noted that — when starting with a neat MDMO-PPV film — the singlet exciton PL is quenched efficiently upon the addition of even small amounts of $PC_{61}BM$ (not shown here, see e.g. References [91] and [168]). Moreover, the residual MDMO-PPV singlet exciton signal decreases for an increasing fullerene load. Thus, the depicted 1:4 blend spectrum was multiplied by a factor of 17 with respect to the 4:1 blend spectrum in order to ensure a good comparability. Again, the lower energetic emission band which is inherent to all displayed blend ratio spectra is attributed to radiative recombination through a relaxed CTS. As already mentioned in Section 6.1, the 1:4 blend ratio possesses a strong residual fullerene singlet exciton emission which is spectrally overlapping with the CTE emission of the blend and thus impedes the conduction of integral PL(F) measurements. The same observation is made for the case of the 1:2 blend. Accordingly, PL(F) experiments were only performed on the $PC_{61}BM$-poor blend ratios of 4:1, 2:1 and 1:1 with the integration range starting at 800 nm. Similar to the case of MDMO-PPV:$PC_{61}BM$ 1:1 reported in Section 6.1, the CTE PL of the different blend ratios is reduced significantly by the application of an external electric field in reverse bias direction as more and more of the CTE are able to overcome their respective binding energy and dissociate into free charge carriers. For high electric fields, the field dependent PL quenching reaches values of up to 97 % (see Figure 7.2).

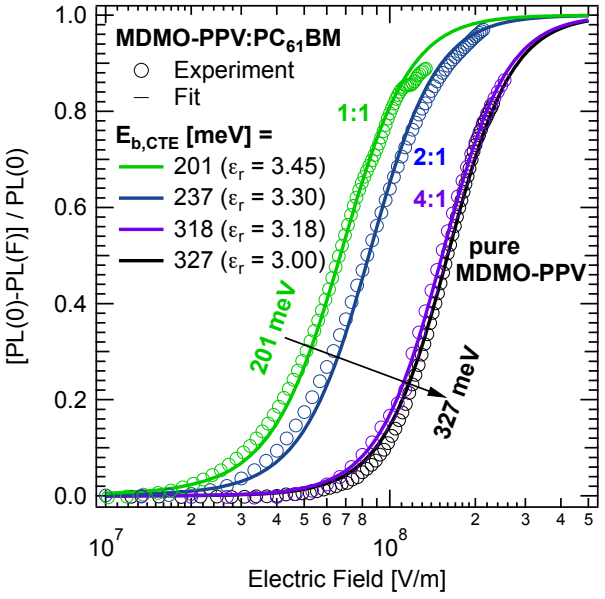

Figure 7.2: PL quenching yield for blends of MDMO-PPV:$PC_{61}BM$ 1:1, 2:1 and 4:1 and for neat MDMO-PPV (open circles) in comparison to the Onsager–Braun dissociation probability (solid lines). For the sake of clarity, error bars are omitted in this picture but can be considered similar to those depicted in Figure 6.5. The extracted binding energies are listed alongside the respective blend ratio dependent effective dielectric constants ϵ_r calculated via Equation 7.1.

At first glance, the comparison of the quenching curves for different blend ratios in Figure 7.2 reveals a fundamental change in the field dependence: For decreasing $PC_{61}BM$ loads, higher electric fields have to be applied in order to dissociate the CTE, hinting at an increased CTE binding energy. Moreover, it should be noted that the quenching curve of the CTE in MDMO-PPV:$PC_{61}BM$ 4:1, displayed by the purple open circles, looks remarkably similar to the one of the singlet exciton in neat MDMO-PPV, displayed by the black open circles. This observation might indicate that the magnitude of the exciton binding energy is not predestined by the nature of the exciton (i.e., it being a CTE or a singlet exciton), but rather depends on other factors which will be discussed in detail later on.

For the more quantitative determination of the CTE binding energies, the quenching curves were fitted with the Onsager–Braun model. While the temperature was set to $T = 297$ K during the experiments, the $\mu\tau$-product was again chosen as a constant value of $\mu\tau = 1 \cdot 10^{-17}$ m^2/V, based on the previously described considerations (see Section 6.3). The limitations of this simplifying approach will be discussed in Section 7.3. The choice of the blend ratio dependent effective dielectric constants was more critical. The determination of the effective dielectric constant in heterogeneous composite systems has been an extensively researched topic in dielectric mixture theory which led to a range of different approaches [169, 170]. In an attempt to provide a simple approximation of the effective dielectric constant for the presented work, the polymer–fullerene blend was regarded as a statistically isotropic dielectric mixture of two components and ϵ_r was determined via the upper Wiener bound [171], given by

$$\epsilon_r = f_{PPV} \cdot \epsilon_{r,PPV} + f_{PCBM} \cdot \epsilon_{r,PCBM}. \tag{7.1}$$

Here, f_{PPV} and f_{PCBM} are the volume fractions of MDMO-PPV and $PC_{61}BM$, respectively. This bound represents a rough estimation of the upper limit of the effective dielectric constants [172] required for the Onsager–Braun calculations. Naturally, since the used fullerene possesses a higher relative dielectric constant than the polymer ($\epsilon_{r,PPV} = 3.0$ [123] vs. $\epsilon_{r,PCBM} = 3.9$ [129]), the effective dielectric constant increases with increasing fullerene load; the calculated values are listed in Figure 7.2. As can be seen in the graph, the Onsager–Braun formalism provides a good description of the experimentally obtained data, allowing for the extraction of the CTE binding energies which are displayed in Figure 7.2 and summarized in Table 7.1.

Apparently, a decrease of the $PC_{61}BM$ load leads to an increase of the CTE binding energy from 201 meV for the 1:1 blend to 318 meV for the 4:1 blend, bringing it close to the singlet exciton binding energy in neat MDMO-PPV of 327 meV. This significant rise in the CTE binding energy of +117 meV is well above the experimental error, which —

Blend composition	**1:1**	**2:1**	**4:1**	**MDMO-PPV**
Exciton	CT	CT	CT	singlet
ϵ_r	3.45	3.30	3.18	3.00
E_b [meV]	201	237	318	327

Table 7.1: CTE and singlet exciton binding energies for MDMO-PPV:$PC_{61}BM$ blends with varying blend ratio and for neat MDMO-PPV. With decreasing $PC_{61}BM$ content, the CTE binding energy is increased significantly.

since all studied blends possessed similar active layer thicknesses — is about ±18 meV. The error made due to the assumption of a constant $\mu\tau$-product will be estimated in Section 7.3. For the further evaluation and support of the obtained findings, TA(F) experiments were conducted, extending the blend ratio range to higher $PC_{61}BM$ loads.

7.1.2 TA(F) Measurements

While the PL(F) technique is only sensitive to those CTE which undergo radiative recombination, TA accounts for the total polaron density which is photogenerated, yielding additional information on the charge carrier generation process. For this study, TA(F) measurements were performed on MDMO-PPV:$PC_{61}BM$ blends of 4:1, 2:1, 1:1, 1:2 and 1:4, using a wavelength of 917 nm in order to probe the positive polarons on MDMO-PPV (see Section 5.2). Exemplarily, the field dependent transients recorded for a MDMO-PPV:$PC_{61}BM$ 1:1 blend are shown in Figure 7.3.

It can be seen that for higher voltages in reverse bias direction, the transients are shifted towards higher values of ΔOD, corresponding to an increase in polaron density. As already stated earlier (Section 5.2), the field dependence of polaron generation is evaluated by integrating each transient over the first 20 ns after excitation (i.e., from 10 ns to 30 ns; see inset in Figure 7.3), representing the polaron generation for different electric fields $\Delta OD_0(F)$. This integration step is justified since in the specified time frame, the recombination behavior does not change significantly. The integrated transients are depicted in Figure 7.4a, normalized to the value at the highest applied electric field where the beginning of a saturation is visible and referred to as $\Delta OD_0(F_{max})$. Since for this study, only the polarons which are generated additionally under the influence of an externally applied electric field are of interest, the polaron generation at zero electric field $\Delta OD_0(0)$ is subtracted as a constant offset, yielding the green curve shown in Figure 7.4b. This curve now allows for a direct comparison to the PL(F) curve recorded for the same MDMO-PPV:$PC_{61}BM$ blend ratio of 1:1, given by the grey open circles.

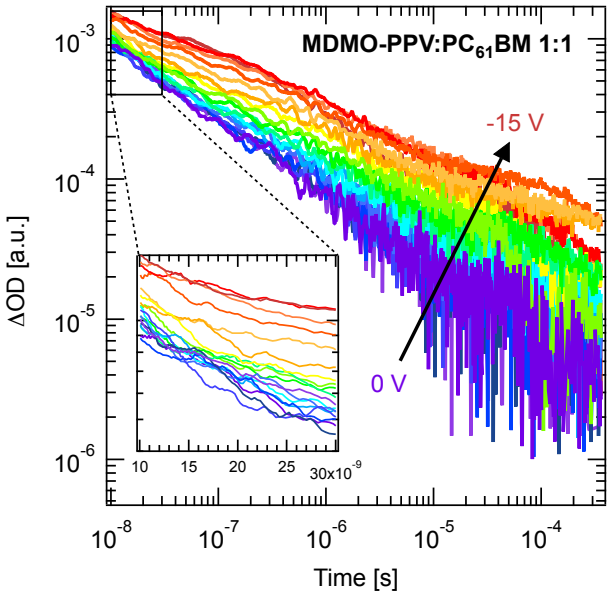

Figure 7.3: Field dependent transients recorded for a MDMO-PPV:PC_{61}BM 1:1 blend. With increasing voltages in reverse bias direction, the polaron density increases as well. For the further evaluation of the data, the first 20 ns after excitation of each transient are integrated, indicated by the inset.

Apparently, the field dependence of the CTE PL quenching recorded via PL(F) matches well with the one of the polaron generation recorded via TA(F), expressing a distinct increase in polaron generation with increasing electric field and reaching a saturation at high electric field values. However, as the TA(F) curve always runs slightly above the PL(F) curve, it seems that more polarons are generated under the influence of the applied electric field than what is to be expected from the dissociation of relaxed CTE. For the explanation of this behavior, which is especially pronounced for intermediate field strengths between $5 \cdot 10^6$ V/m and $5 \cdot 10^7$ V/m, several plausible scenarios come into mind. For example, it might be due to alternative non-radiative recombination pathways which are not probed in PL(F) experiments and might express a different field dependence than the radiative pathways. Also, the observed discrepancy might be related to hot, not yet fully thermalized CTE which could already dissociate at weaker electric fields than their relaxed counterparts. While such hot CTE cannot be monitored via PL(F), they might very well contribute to the polaron generation detected by TA(F). Even if the actual origin of the deviation between the PL(F) and the TA(F) curve cannot be unambiguously determined, Figure 7.4b demonstrates that both the PL(F) and the TA(F) technique provide comparable results as far as the general field dependence of charge carrier photogeneration is concerned.

The comparison of the TA(F) results for different MDMO-PPV:PC_{61}BM blend ratios can be seen in Figure 7.5. It should be noted that in contrast to Figure 7.4, the de-

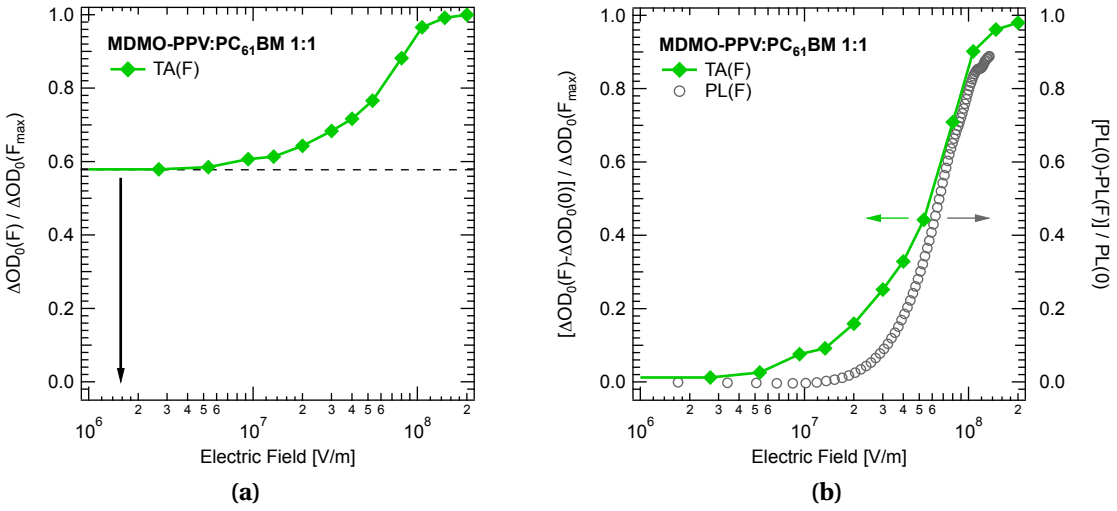

Figure 7.4: Integrated transients for different external electric fields for an MDMO-PPV:PC_{61}BM 1:1 sample. **(a)** For increasing electric field strengths, an increasing number of polarons is generated, reaching a saturation at high electric field strengths. In order to exclusively evaluate the polarons which are generated under the influence of the external electric field, the polaron generation at zero electric field is subtracted as a constant offset. **(b)** The comparison of the resulting TA(F) curve with a corresponding PL(F) curve shows a good agreement between the two experimental methods. The slightly higher polaron generation at intermediate electric field strengths in comparison to the dissociation of relaxed CTE might be due to non-radiative recombination pathways or to dissociation routes via hot CTE.

picted curves are not normalized and the electric field is now displayed on a linear instead of a logarithmic scale. In Figure 7.5, the solid lines represent the mean of several measurements while the shaded regions indicate the deviations between the averaged measurements. For the sake of clarity, the curves for the different blend ratios are displayed with an offset. Moreover, the polaron generation at zero electric field is visualized by the grey dashed lines. At first sight, a remarkable tendency becomes evident in the onset of the field dependence. Starting at the low fullerene content blend of 4:1, a constant polaron generation is observed for low electric field strengths, with the field dependence only setting in at a field strength of about $2 \cdot 10^7$ V/m. For higher PC_{61}BM loads, this onset is shifted towards lower electric fields, and for the (in terms of photovoltaics) best-performing, fullerene-rich 1:2 and 1:4 blend ratios, a distinct field dependence is observed right upon the application of even small electric fields. This shifting onset of the field dependence is visualized by the black dashed and dotted line in Figure 7.5, serving as a guide to the eye. The shift towards lower electric fields for an increasing fullerene load can be regarded as an indication for a decreasing CTE binding energy, thus supporting the results obtained via the PL(F) measurements and extending the validity of the previously drawn conclusions to the 1:2 and 1:4 blend ratios.

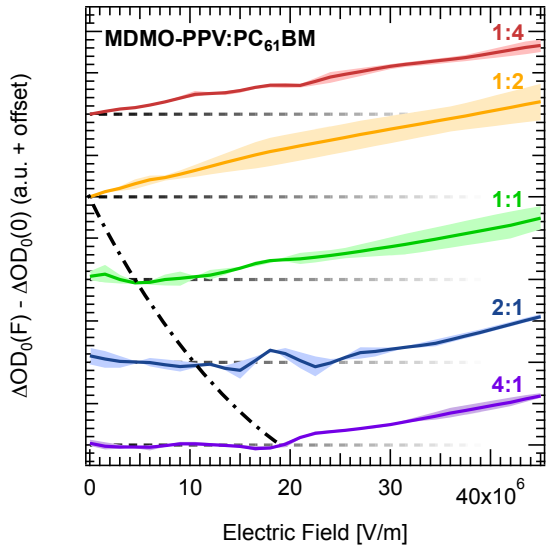

Figure 7.5: TA(F) results for the investigated MDMO-PPV:PC_{61}BM blend ratios. The solid lines represent the mean of several measurements while the shaded regions indicate the deviations between single measurements. For an increasing fullerene load, the onset of the field dependence is shifted towards lower electric field strengths, as visualized by the black dashed and dotted line. For the blend ratios of 1:2 and 1:4, a distinct field dependent polaron generation can already be observed right upon the application of even low electric fields.

Apparently, both PL(F) and TA(F) measurements suggest a decrease of the CTE binding energy with an increase of the PC_{61}BM content of the blend system. This observation might be due to mainly two possible scenarios. On the one hand, the decrease in binding energy might be related to an increase of the effective dielectric constant of the system, whereas on the other hand, an increase of the CTE delocalization length might be held accountable for the observed phenomenon. The first case would imply an effective ϵ_r considering the volume fractions of the two blend components (as already assumed for the extraction of the binding energies via the Onsager–Braun model in Section 7.1.1) instead of a local, blend ratio independent ϵ_r as given by the average of $\epsilon_{r,PPV}$ and $\epsilon_{r,PCBM}$. In the second scenario, a higher delocalization of the interfacial CTE could mainly be achieved by the formation and expansion of PC_{61}BM clusters as discussed by Deibel et al. [93]. Here, it should be noted that other influences on the CTE binding energy such as changes in the $\mu\tau$-product, in the disorder or in the LUMO of the acceptor due to a higher crystallization are possible and cannot be excluded based on the presented experimental results. In order to shed light onto the relevance of the two experimentally accessible scenarios — i.e., a change in the dielectric constant or in the CTE delocalization length — the morphologies of the different blend ratios are examined via AFM and ODMR measurements.

7.2 Morphological Characterization

The topological characterization of the blend films was achieved by AFM measurements. The respective height and phase images for the different blend ratios are displayed in Figure 7.6. In consistence with earlier publications [31, 167], the fullerene-poor blend ratios of 4:1 to 1:1 exhibit a relatively smooth surface which indicates a homogeneous intermixing of the two blend components. Here, $PC_{61}BM$ is assumed to be molecularly dispersed in the surrounding MDMO-PPV matrix. For the fullerene-rich blend ratios of 1:2 and 1:4, distinct bright and dark regions are visible in the AFM images. The observation of such clearly distinguishable regions indicates a phase segregation with the formation of $PC_{61}BM$ clusters. Yet, it should be noted that the presence of MDMO-PPV or $PC_{61}BM$ in domains of the respective other material cannot be ruled out [31, 91, 168]. Since the shown AFM data merely provide information on the surface of the blends, they cannot serve as proof for a non-occuring phase separation in the bulk of the low fullerene content blend films. Therefore, the morphological characterization was completed by ODMR measurements, yielding information on both the surface and the bulk of the studied films. As already indicated in Section 5.3.2, ODMR allows for unambiguously proving the existence of triplet excitons. In the context of the presented work, ODMR is used as an indicator for phase segregation in the blend films: While an efficient quenching of triplet excitons in the blends is regarded as an indication for a good intermixing, a lack thereof serves as proof of phase segregation instead. ODMR measurements on blends of MDMO-PPV:$PC_{61}BM$ were already reported by Scharber et al. in 2003 [173]. However, due to the sensitivity of the experimental setup, the reported results were limited to blends with a $PC_{61}BM$ load of only up to 10 %. Here, this range is extended, obtaining the triplet exciton signatures of the neat polymer and fullerene as well as of blends with ratios from 1:4 to 4:1. As expected from earlier measurements on a similar PPV derivative [174], the neat MDMO-PPV possesses a localized triplet which leads to both a full field and a half field signal, the latter of which is shown in the lower trace in Figure 7.7. This MDMO-PPV triplet half field signature clearly differs from the one of neat $PC_{61}BM$, depicted in the upper trace of Figure 7.7. Thus, in blends of the two materials, the respective triplet contributions can be easily distinguished. Upon the addition of small amounts of $PC_{61}BM$ (see trace of the 4:1 blend), the overall MDMO-PPV PL is quenched and in return, the intensity of the triplet signature increases as compared to neat MDMO-PPV. With a further increase of the fullerene load of the blend to a 2:1 ratio, the PL quenching trend continues while the triplet yield is now reduced as well, possibly in favor of CTS. Still, the residual

PL only allows for the detection of a MDMO-PPV localized triplet; no $PC_{61}BM$ localized triplet is observed.

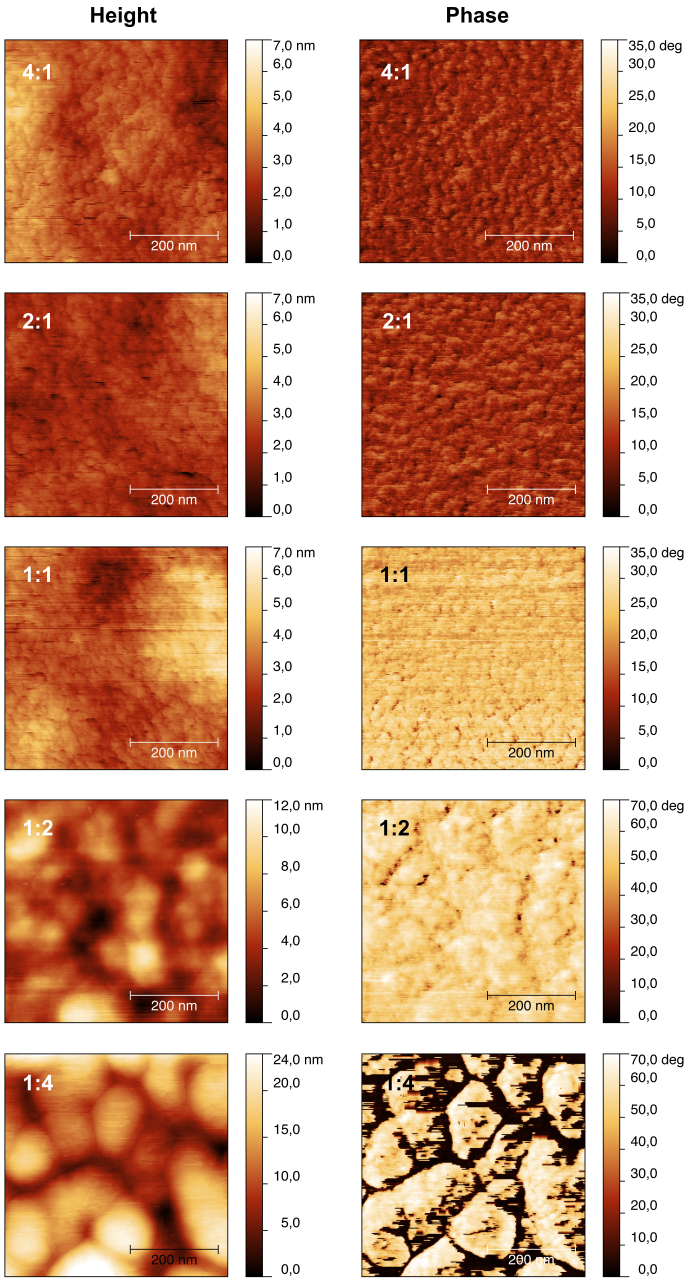

Figure 7.6: AFM height and phase images of the investigated MDMO-PPV:$PC_{61}BM$ blends. The bright regions are attributed to $PC_{61}BM$ while the dark regions represent MDMO-PPV-rich domains. The image size is 500 nm × 500 nm in all cases. Starting at a $PC_{61}BM$ load of 1:2, the formation of $PC_{61}BM$ clusters is clearly visible.

For the 1:1 blend ratio, the MDMO-PPV triplet yield is further reduced. However, a new feature can be observed, rising at a magnetic field of about 167.9 mT and being attributed to the fullerene localized triplet. Apparently, excited $PC_{61}BM$ can now undergo intersystem crossing into the triplet state since there are no donor molecules

in its immediate vicinity which could promote a CT instead. This means that small fullerene domains have to be present in order to explain the observed $PC_{61}BM$ triplet signature. It should be noted that in principle, an acceptor (or donor) triplet state can also be populated via electron back transfer from a CTS if the CTS energy of the system is equal to or higher than the acceptor (or donor) triplet energy. However, in MDMO-PPV:$PC_{61}BM$, this is not the case [56], meaning that the observed fullerene triplet can only originate from an intersystem crossing process. The fullerene triplet exciton peak develops into a prominent feature in the $PC_{61}BM$-rich blends of 1:2 and 1:4, hinting at the formation of larger size fullerene domains.

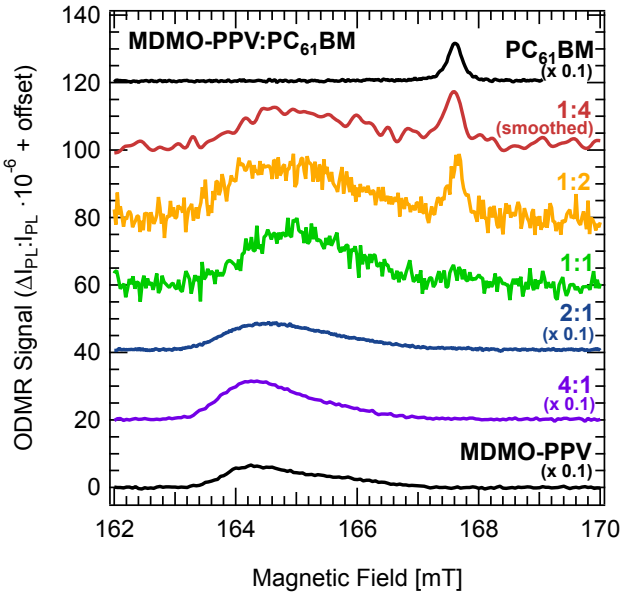

Figure 7.7: ODMR half field transition spectra of the investigated blend systems. In addition to the blend spectra, the neat material spectra of MDMO-PPV and $PC_{61}BM$ are displayed in order to illustrate the spectral position of the corresponding localized triplet exciton. The curves represent the resonant change of PL due to microwave modulation, normalized to the absolute PL signal. While the 4:1 and 2:1 blend ratios only show a contribution of the MDMO-PPV localized triplet, the higher fullerene load blends starting at 1:1 also express a $PC_{61}BM$ localized triplet signature, hinting at an occurring phase separation.

Considering the results of both AFM and ODMR measurements, the possibility of phase segregation in the fullerene-poor blend ratios of 4:1 and 2:1 can be excluded, being consistent with the absence of residual $PC_{61}BM$ singlet exciton emission in the respective PL spectra (see Figure 7.1). This observation corroborates the assumption made by Hallermann et al. [91] that for these blend systems, the fullerene molecules are molecularly dispersed in the surrounding MDMO-PPV matrix. Concerning the 1:1 blend, however, the high sensitivity of the ODMR technique allows for more precise conclusions than those drawn from AFM images, PL spectra or even transmission elec-

tron microscopy [31]: In the 1:1 blend, the formation of small $PC_{61}BM$ domains is already indicated in the ODMR half field spectrum even if the AFM image still shows a flat, well-intermixed surface. However, the size of those $PC_{61}BM$ clusters seems to be tiny since no residual fullerene PL emission is observed in the corresponding PL spectrum (see Figure 7.1). This fullerene domain size is significantly increased for the $PC_{61}BM$-rich blend ratios of 1:2 and 1:4, which can be deduced from AFM and ODMR results as well as from the distinct residual $PC_{61}BM$ PL emission in the respective PL spectra.

7.3 Discussion

The presented morphological characterization of the different blend systems helps to clarify the roles of the relative dielectric constant ϵ_r and of the CTE delocalization length for charge carrier photogeneration via intermediate relaxed CTS. Since the relative impact of the mentioned factors is strongly dependent on the prevailing blend ratio, the further considerations are split into two parts, separately addressing fullerene-poor and fullerene-rich blend systems.

Fullerene-Poor Blend Ratios (4:1, 2:1 and 1:1)

For the MDMO-PPV:$PC_{61}BM$ 4:1, 2:1 and 1:1 blends, no or — for the 1:1 blend ratio — no significant phase segregation is observed. This implies that for these blends, no change is expected for the CTE delocalization length which is related to the formation of microcrystalline fullerene clusters allowing for a higher electron–hole distance. As far as the dielectric constant is concerned, there are mainly two different points of view. On the one hand, one might argue that due to the position of the CTE at the donor–acceptor interface with $\epsilon_{r,PPV} = 3.0$ and $\epsilon_{r,PCBM} = 3.9$, the CTE should always be subject to the same dielectric constant of $\epsilon_r = 3.45$, irrespective of the actual blend ratio. On the other hand, since a changing CTE delocalization length has already been ruled out for the low fullerene content blend ratios, a constant relative dielectric constant would fail to explain the observed shifting field dependence of charge carrier photogeneration. In order to account for this change in field dependence, the CTE binding energy has to be influenced by an effective dielectric constant which is determined by the volume fractions of polymer and fullerene in the respective blend. Thus, for a rising $PC_{61}BM$ content, the interfacial CTE is increasingly exposed to the higher ϵ_r of the fullerene molecules in its vicinity and as a result, its binding energy is reduced (keeping in mind that this conclusion is made under the assumption of a constant $\mu\tau$-product). The described scenario is also in accordance with a previous publication by Mihailetchi

et al. [175], reporting on photocurrent measurements for the same blend system which were fitted by a numerical model. Here, a decrease of the fullerene content from 80 % (i.e., a 1:4 blend ratio) to 50 % (i.e., a 1:1 blend ratio) led to a significant reduction of the dissociation efficiency of bound electron–hole pairs. This observation was at least partially ascribed to a presumably decreasing, spatially averaged dielectric constant, related to a stronger electron–hole pair binding energy. The experimental findings presented in this work validate the decrease in the binding energy with a rising fullerene content and the eligibility of the assumption of an effective, blend ratio dependent dielectric constant. However, it should be noted that the increase in dielectric constant with higher fullerene content cannot fully account for the strong decrease in the binding energy, which should be proportional to $\frac{1}{\epsilon_r}$. Apparently, additional factors such as changes in the $\mu\tau$-product, disorder effects or variations in the $PC_{61}BM$ LUMO might have an impact on the CTE binding energy as well.

Blend composition	**1:1**	**4:1**
ϵ_r	3.45	3.18
$\mu\tau$ [m^2/V]	$1 \cdot 10^{-17}$	$1 \cdot 10^{-17}$
$E_{b,CTE}$ [meV]	201	318

Table 7.2: Reference values for the CTE binding energy of MDMO-PPV:$PC_{61}BM$ 1:1 and 4:1. $E_{b,CTE}$ was calculated under the assumption of a blend ratio dependent effective dielectric constant and a constant $\mu\tau$-product of $1 \cdot 10^{-17}$ m^2/V.

Blend composition	**1:1**	**4:1**
ϵ_r	3.45	3.18
$\mu\tau$ [m^2/V]	$1 \cdot 10^{-17}$	$5 \cdot 10^{-19}$
$E_{b,CTE}$ [meV]	201	209

Table 7.3: CTE binding energies of MDMO-PPV:$PC_{61}BM$ 1:1 and 4:1 under the assumption of a decreased $\mu\tau$-product for the 4:1 blend. The used dielectric constant is the same as in Table 7.2.

In order to evaluate the potential error made in the calculation of $E_{b,CTE}$ due to the assumption of a constant $\mu\tau$-product, references of changes in μ and in τ for varying blend ratios have to be taken into account. To the best knowledge of the author, no blend ratio dependent studies of the CTE lifetime τ in the material system MDMO-PPV:$PC_{61}BM$ have been presented in literature so far. However, such investigations

have been carried out for a different material system (using a fluorene copolymer as donor and $PC_{61}BM$ as acceptor) by Veldman et al. [57]. For this particular system, τ was found to be reduced by a factor of about 2 when going from a 4:1 (i.e., 20 wt % $PC_{61}BM$) to a 1:4 (i.e., 80 wt % $PC_{61}BM$) blend ratio. Measurements for a 1:1 blend ratio are not reported on in this publication. Coming to speak of μ, there do not seem to exist blend ratio dependent measurements of the local charge carrier mobility in MDMO-PPV:$PC_{61}BM$ blends. Yet, the blend ratio dependence of the global charge carrier mobility for this material system has been studied via photo-CELIV by Dennler et al. [164]. Apparently, the global μ increases significantly by a factor of about 40 when going from a 4:1 blend to a 1:1 blend. Assuming that the reported blend ratio dependent changes in μ and τ also apply to the material system and the local charge carrier mobility used in this thesis, the $\mu\tau$-product would decrease from $1 \cdot 10^{-17}$ m^2/V for a 1:1 blend to $5 \cdot 10^{-19}$ m^2/V for a 4:1 blend. Using the latter value for the calculation of the CTE binding energy in a 4:1 blend, a tremendous drop from 318 meV to 209 meV is observed for $E_{b,CTE}$ as compared to the $E_{b,CTE}$ previously calculated under the assumption of a constant $\mu\tau$-product of $1 \cdot 10^{-17}$ m^2/V. These calculations are summarized in Tables 7.2 and 7.3. Thus, assuming a $\mu\tau$-product which is decreasing by a factor of 20 when going from a 1:1 to a 4:1 blend ratio, the CTE binding energies for the two different blends would be equal within the experimental error. This observation indicates that the error made by the estimation of the $\mu\tau$-product is certainly higher than the experimental error due to the determination of the active layer thickness. In any case, it should be kept in mind that the change in the $\mu\tau$-product by a factor of 20 is based on reports for a different material system and for a global instead of a local charge carrier mobility and can only serve as the basis for a rough error estimation in the context of this thesis.

Fullerene-Rich Blend Ratios (1:2 and 1:4)

In contrast to the fullerene-poor blend ratios, the high $PC_{61}BM$ content blends of 1:2 and 1:4 exhibit a distinct phase segregation with the formation of large-scale $PC_{61}BM$ domains. For these phase separated blends, the onset of the field dependence observed via TA(F) occurs right upon the application of even small electric fields. This phenomenon may be ascribed to an interplay of both a higher effective dielectric constant and a larger CTE delocalization length. Such a higher delocalization is related to the presence of microcrystalline $PC_{61}BM$ clusters which express a high electron mobility [57, 93, 175]. Thus, for blends with a $PC_{61}BM$ load exceeding 60 %, a sharp increase in the mobility has been reported [76]. For these well phase segregated blends, no clear distinction can be made between the impact of ϵ_r and CTE delocalization on CTE sep-

aration. Yet, both factors clearly have a strong influence on the field dependence of charge carrier photogeneration via CTS precursors.

7.4 Conclusions

Extending the results presented in Chapter 6, the electric field dependence of charge carrier photogeneration via CTS precursors has been investigated for different MDMO-PPV:$PC_{61}BM$ blend ratios. PL(F) measurements on the fullerene-poor blend ratios of 4:1, 2:1 and 1:1 revealed a remarkable shift in the field behavior of the relaxed CTE PL emission. By fitting the experimental data to the Onsager–Braun model, decreasing CTE binding energies of 318 meV (with $\epsilon_r = 3.18$), 237 meV (with $\epsilon_r = 3.30$) and 201 meV (with $\epsilon_r = 3.45$) could be extracted for increasing $PC_{61}BM$ loads, assuming a constant $\mu\tau$-product of $1 \cdot 10^{-17}$ m^2/V. The observed trend in field dependence was also found to hold true for the better-performing, fullerene-rich blend ratios of 1:2 and 1:4, as shown by TA(F) experiments. Morphological investigations of the studied blend systems via AFM and ODMR suggested a homogeneous surface and bulk structure for the 4:1 and 2:1 blends, the start of a phase segregation for the 1:1 blend and clearly separated $PC_{61}BM$ domains for the 1:2 and 1:4 blends. These results indicate that for the fullerene-poor blends, an effective, blend ratio dependent dielectric constant can be held accountable for the detected CTE field dependence. For the fullerene-rich blends exhibiting microcrystalline $PC_{61}BM$ domains, however, the observed field dependence is likely due to an interplay of an increase in both the dielectric constant and the CTE delocalization length. In a greater picture, the discussed results stress the importance of a high dielectric constant in order to ensure an efficient charge carrier photogeneration in organic solar cell devices.

8 Effects of Acceptor LUMO and Trap States

While the CTE binding energy has just been shown to strongly depend on the donor–acceptor blend ratio which determines both the effective relative dielectric constant and the morphology of the blend system, there are several other candidates which might have an impact on $E_{b,CTE}$. The following chapter addresses the influence of the acceptor energetics by substituting $PC_{61}BM$ for two other fullerene derivatives, bisPCBM and $PC_{71}BM$. The fullerene bisadduct bisPCBM was first introduced in 2008 by Lenes et al. [130] with the main goal of improving the open circuit voltage. As V_{oc} is decisively governed by the energy difference between the donor HOMO and the acceptor LUMO, an increase of the latter will lead to an increase of V_{oc} without shifting the absorption of the device (like changing the donor LUMO or HOMO would) [130]. Such a rise in the LUMO level is reported for bisPCBM with an increase of roughly 0.1 eV as compared to $PC_{61}BM$, attributable to the attachment of a second side chain on the C_{60} cage [130]. Consequently, Lenes et al. observed a 0.15 V higher V_{oc} for P3HT:bisPCBM devices as compared to P3HT:$PC_{61}BM$, leaving j_{sc} almost unchanged and thus increasing the device efficiency by a factor of 1.2. The assignment of the increase in the open circuit voltage to an increase in the acceptor LUMO was recently validated by another group [176].

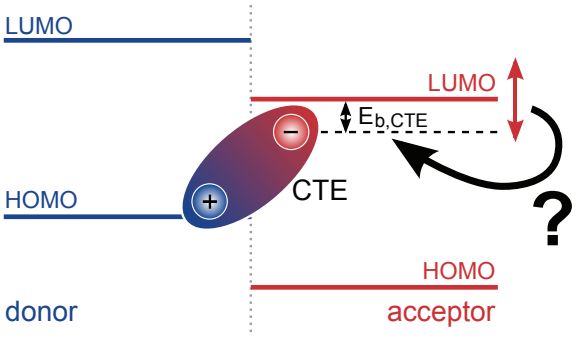

Figure 8.1: Possible interplay between the acceptor LUMO level and the CTE binding energy. Since the CTE forms out between the HOMO of the donor and the LUMO of the acceptor, shifting the acceptor LUMO might influence the CTE binding energy.

Coming back to speak of the central topic of this thesis, i.e., the CTE which is formed out between the donor HOMO and the acceptor LUMO, one might reason that an increase of the acceptor LUMO level does not only lead to a rise in V_{oc} but also alter the binding energy of the CTE (see Figure 8.1). In order to test this hypothesis, PL(F) measurements were conducted on solar cell devices utilizing MDMO-PPV as donor and $PC_{61}BM$, bisPCBM and $PC_{71}BM$ as acceptors. In contrast to bisPCBM, the LUMO level difference between $PC_{71}BM$ and $PC_{61}BM$ only amounts to some meV [27] so that one would expect no change in $E_{b,CTE}$ for MDMO-PPV:$PC_{61}BM$ and MDMO-PPV:$PC_{71}BM$ blends. The determined CTE binding energies for all three blend systems are discussed in terms of the acceptor LUMO level variation and yet another influencing factor related to the acceptor energetics, namely the trap states of the acceptor.

8.1 CTE Binding Energies for Different Acceptors

Prior to the actual PL(F) measurements for the extraction of the CTE binding energies, the PL spectra of MDMO-PPV blended with either $PC_{61}BM$, bisPCBM or $PC_{71}BM$ had to be evaluated in order to determine a suitable blend ratio for all subsequent experiments. Since the fullerene load of a blend has a major impact on the CTE binding energy (see Chapter 7), a comparison of the latter for different acceptors is only justified when using the same blend ratio for all studied blend systems. While the use of 1:1 blends would have been desirable due to a good comparability to the previously presented results in Chapters 6 and 7, $PC_{71}BM$ turned out to be the limiting factor regarding this goal. Unlike MDMO-PPV:$PC_{61}BM$ 1:1 (see Figure 6.3) and MDMO-PPV:bisPCBM 1:1 (PL spectra not shown here), the PL spectrum of MDMO-PPV:$PC_{71}BM$ 1:1 displays a distinct peak which can be assigned to residual PL emission from neat $PC_{71}BM$, overlapping with the CTE emission at higher wavelengths and thus impeding the conduction of PL(F) experiments (see Figure 8.2). For MDMO-PPV:$PC_{71}BM$ blends in a 1.5:1 and 2:1 blend ratio, however, no residual fullerene derivative emission is observed in the PL spectra. Consequently, a blend ratio of 2:1 was chosen for all MDMO-PPV:fullerene derivative blends in order to ensure the comparability to the results presented in Chapter 7.

The 2:1 blend ratio PL spectra for the different acceptors are summarized in Figure 8.3; the neat fullerene derivative PL signals are displayed as dotted curves in the same colors as the respective blend signals.

The PL quenching curves originating from integral PL(F) measurements on the three 2:1 blend systems are depicted as the open circles in Figure 8.4. Again, the experimental error bars due to the determination of the active layer thicknesses are omitted in this

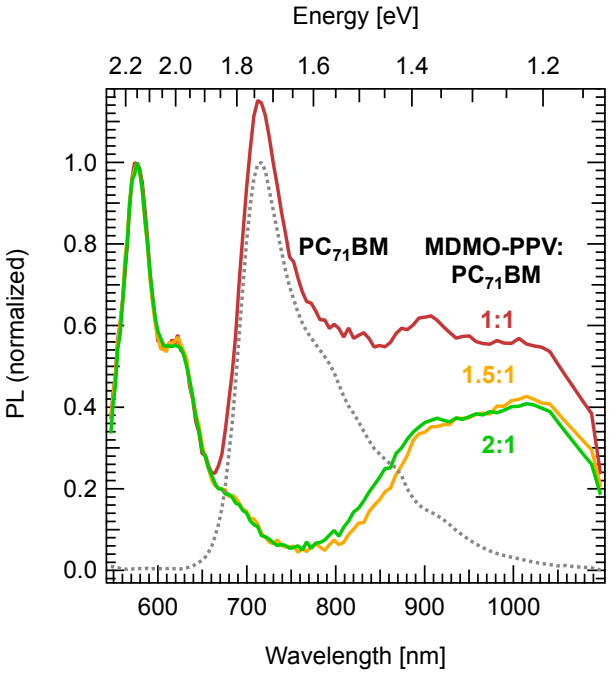

Figure 8.2: PL spectra of MDMO-PPV:$PC_{71}BM$ in a 1:1, 1.5:1 and 2:1 blend ratio. The PL spectrum of neat $PC_{71}BM$ is given by the grey dotted line. In all spectra, CTE emission is observed in the infrared spectral range. While the PL spectrum of MDMO-PPV:$PC_{71}BM$ 1:1 displays a strong residual emission which can be attributed to the neat fullerene, such a feature is absent in the spectra of the 1.5:1 and 2:1 blend. For a better comparability to previously presented results (see Chapter 7), the 2:1 blend ratio is chosen for further evaluations.

picture but are similar to the ones given in Figure 6.6. On first glance, it can be seen that the field dependent PL quenching is shifted to higher electric fields when switching from MDMO-PPV:$PC_{61}BM$ 2:1 to MDMO-PPV:bisPCBM 2:1 and onwards to MDMO-PPV:$PC_{71}BM$ 2:1. A more quantitative evaluation of the experimental results, i.e., the determination of the CTE binding energies via the Onsager–Braun model, requires the effective relative dielectric constants ϵ_r and the $\mu\tau$-products of the respective blends as input parameters. Whereas ϵ_r of the MDMO-PPV:$PC_{61}BM$ 2:1 blend was already chosen as 3.30 based on literature values for MDMO-PPV ($\epsilon_{r,PPV} = 3.0$ [123]) and $PC_{61}BM$ ($\epsilon_{r,PCBM} = 3.9$ [129]) in Chapter 7, to the best knowledge of the author, there currently exist no reports in literature on the relative dielectric constants of bisPCBM and $PC_{71}BM$. Thus, the effective relative dielectric constants of MDMO-PPV:bisPCBM 2:1 and MDMO-PPV:$PC_{71}BM$ 2:1 were assumed to be similar to the one of MDMO-PPV:$PC_{61}BM$ 2:1, i.e., $\epsilon_r = 3.30$. As for the $\mu\tau$-product, the CTS lifetime was again chosen as 1 ns due to the lack of specific literature values for the investigated blend systems. Also, a literature search on TRMC measurements of the local charge carrier mobilities for the studied blend systems yielded no results. Speaking of the global electron

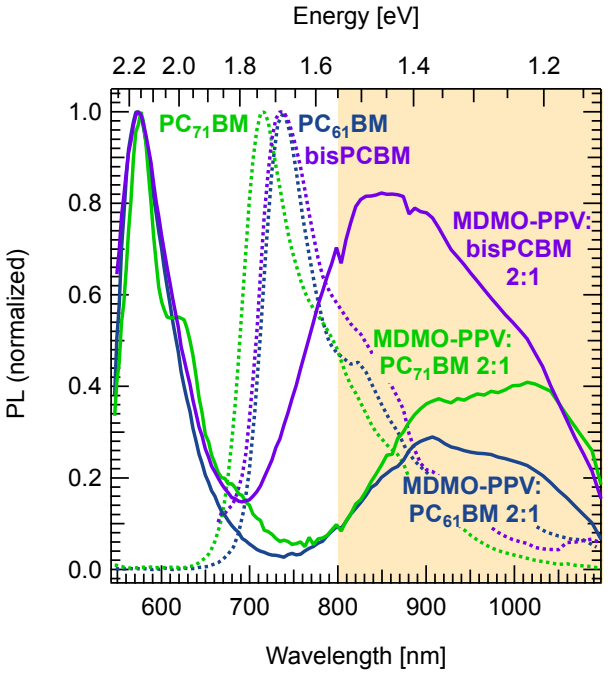

Figure 8.3: PL spectra of MDMO-PPV:$PC_{61}BM$, MDMO-PPV:$PC_{71}BM$ and MDMO-PPV:bisPCBM, all in a 2:1 blend ratio. The respective fullerene spectra are displayed as dotted lines in the same colors as the corresponding blend spectra. Apparently, none of the investigated 2:1 blend systems exhibits any residual PL emission due to the neat fullerenes. The spectral region used for the integral PL(F) measurements is indicated by the shaded background.

mobilities of the neat acceptor materials, Wöbkenberg et al. [177] reported comparable values for both $PC_{61}BM$ and $PC_{71}BM$ OFETs while Lenes et al. [130] found that the electron mobility in neat bisPCBM is reduced by a factor of about 3 to $7 \cdot 10^{-8}$ m^2/Vs as compared to $2 \cdot 10^{-7}$ m^2/Vs for neat $PC_{61}BM$. However, since the impact of the electron mobility of the neat acceptor material on the local charge carrier mobility of an actual photovoltaic device using MDMO-PPV as donor and a donor–acceptor blend ratio of 2:1 remains unclear, an estimated $\mu\tau$-product of $1 \cdot 10^{-17}$ m^2/V is used for the further evaluations. Based on the discussed estimations for ϵ_r and the $\mu\tau$-product, the comparison of the Onsager–Braun theory to the experimental data yields CTE binding energies which are increasing from MDMO-PPV:$PC_{61}BM$ 2:1 over MDMO-PPV:bisPCBM 2:1 to MDMO-PPV:$PC_{71}BM$ 2:1 and which are listed in Figure 8.4. Here, it should be noted that the largest difference in $E_{b,CTE}$, i.e., the difference between the CTE binding energy in MDMO-PPV:$PC_{71}BM$ 2:1 of 280 meV and the one in MDMO-PPV:$PC_{61}BM$ 2:1 of 237 meV which amounts to 43 meV, is only slightly larger than the experimental error of each of these values which is about ±18 meV. Moreover, for the rather small differences in the quenching curves observed for the three different acceptors, the choice of the $\mu\tau$-product plays a crucial role for the determination of the CTE binding energies. Un-

der the assumption that the local charge carrier mobility in MDMO-PPV:bisPCBM 2:1 is also reduced by a factor of 3 like the global electron mobility in bisPCBM as compared to $PC_{61}BM$, a $\mu\tau$-product of $3 \cdot 10^{-18}$ m^2/V would have to be fed into the Onsager–Braun model. This would result in a binding energy of the CTE in MDMO-PPV:bisPCBM 2:1 of only 217 meV, being much smaller than the 263 meV calculated for a $\mu\tau$-product of $1 \cdot 10^{-17}$ m^2/V and even smaller than the one of MDMO-PPV:$PC_{61}BM$ 2:1.

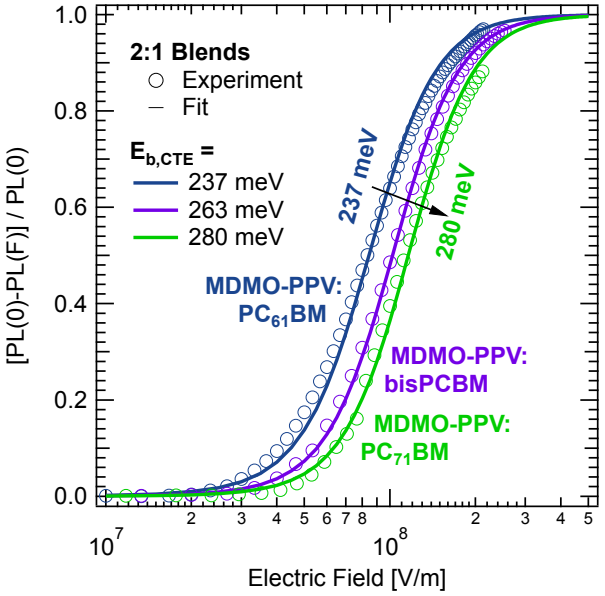

Figure 8.4: PL quenching yield for MDMO-PPV blends with the fullerene derivatives $PC_{61}BM$, bisPCBM and $PC_{71}BM$, each in a 2:1 blend ratio. The open circles represent the experimental data while the solid lines depict the respective fitted Onsager–Braun dissociation probabilities, using an effective relative dielectric constant of $\epsilon_r = 3.30$ and a $\mu\tau$-product of $1 \cdot 10^{-17}$ m^2/V for the extraction of the CTE binding energies. For the sake of clarity, error bars are omitted.

Keeping these limitations concerning the validity of the determined CTE binding energies in mind and assuming a constant $\mu\tau$-product for all three blend systems, possible causes of the observed deviations in $E_{b,CTE}$ are discussed in the following section.

8.2 Discussion

Starting from the previously made hypothesis that a change in the acceptor LUMO level might lead to a change in the CTE binding energy, it is quite obvious that the obtained experimental results cannot validate such an assumption. In order to do so, the CTE binding energies of MDMO-PPV:$PC_{61}BM$ 2:1 and MDMO-PPV:$PC_{71}BM$ 2:1 (with $PC_{61}BM$ and $PC_{71}BM$ possessing similar LUMO levels) would have to be comparable to each other, while the one of the MDMO-PPV:bisPCBM 2:1 blend (with the LUMO

level of bisPCBM exceeding the one of $PC_{61}BM$ by about 0.1 eV) would have to clearly differ. Yet, a rising CTE binding energy is observed when switching between $PC_{61}BM$, bisPCBM and $PC_{71}BM$ as blend acceptor. While an impact of the acceptor LUMO level on the CTE binding energy cannot be fully excluded based on the presented results, it is evident that the LUMO energy is not the root cause of the differences in $E_{b,CTE}$. However, these differences might well be related to acceptor trap states, representing another aspect of the energetics of the respective fullerene derivatives.

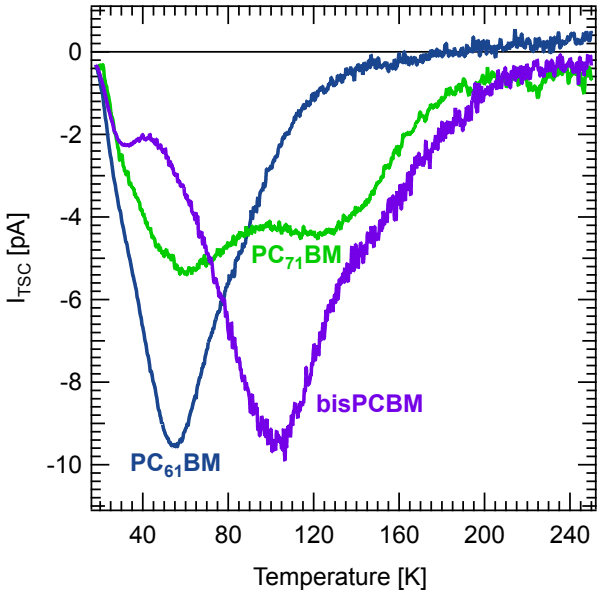

Figure 8.5: TSC spectra of the neat fullerenes $PC_{61}BM$, bisPCBM and $PC_{71}BM$. Both bisPCBM and $PC_{71}BM$ display broader TSC spectra which are spread towards higher temperatures as compared to $PC_{61}BM$, implying broader trap distributions and higher activation energies (graph adapted from [178] with permission of Julia Rauh).

In 2011, Julia Rauh (formerly Schafferhans, PhD student at Experimental Physics VI) investigated the trap states in $PC_{61}BM$, bisPCBM and $PC_{71}BM$ via thermally stimulated current (TSC) measurements [178]. During TSC experiments, the traps which are inherent to the investigated organic semiconductors are first filled by illuminating the samples at low temperatures (18 K). After a certain dwell time, the trapped charge carriers are then released by thermal activation, i.e., by increasing the temperature up to 300 K with a constant heating rate. Meanwhile, the resulting current I_{TSC} as a function of temperature is detected. I_{TSC} is caused by the extraction of the released charge carriers due to the built-in potential. The TSC spectrum can also be detected fractionally, meaning that after trap-filling, the sample is pre-heated to a certain temperature and the spectrum is taken afterwards without any additional trap-filling steps. From the gathered data, information on the trap states such as the lower limit of the trap density n_t and the trap activation energy E_t can be gained. A more detailed description of the

TSC experiments and the subsequent data evaluation can be found in the publication of Schafferhans et al. [178]. The TSC spectra for the three fullerene derivatives $PC_{61}BM$, bisPCBM and $PC_{71}BM$ as reported in the mentioned paper are displayed in Figure 8.5. The shapes of all three spectra hint at a broad trap distribution instead of localized trap levels. The curves of bisPCBM and $PC_{71}BM$ display even broader distributions stretched to higher temperatures as compared to $PC_{61}BM$, indicating higher activation energies. While $PC_{61}BM$ exhibits mainly one feature with a maximum at 55 K, bisPCBM possesses two distinct peaks, a minor one at 32 K and a dominant one at 103 K. $PC_{71}BM$ also shows two features, situated at 60 K and 120 K and being of comparable height. A quantitative evaluation of the experimental data described in Reference [178] yields the activation energies corresponding to the respective peak temperatures as well as the lower limits of the trap densities for all three fullerene derivatives (see Table 8.1).

Acceptor	**$PC_{61}BM$**	**bisPCBM**	**$PC_{71}BM$**
LUMO relative to $PC_{61}BM$	-	+ 0.1 eV	-
$E_{b,CTE}$ [meV]	237	263	280
$n_t[m^{-3}]$	$\geq 1.7 \cdot 10^{22}$	$\geq 2.3 \cdot 10^{22}$	$\geq 2.0 \cdot 10^{22}$
E_t [meV]	**86**	45 / **184**	96 / **223**

Table 8.1: CTE binding energies of MDMO-PPV blended with $PC_{61}BM$, bisPCBM and $PC_{71}BM$ in a 2:1 blend ratio in comparison to the trap state characteristics of the respective neat fullerene derivatives. Both bisPCBM and $PC_{71}BM$ feature higher trap densities and higher activation energies as compared to neat $PC_{61}BM$, which might be correlated to the increased CTE binding energies of the first two fullerene derivatives in blends with MDMO-PPV.

Given the fact that in comparison to $PC_{61}BM$, trap states seem to play a more important role for bisPCBM and $PC_{71}BM$ due to the higher trap densities, and considering the existence of deeper traps with higher activation energies in the latter fullerene derivatives, a possible correlation might be seen between the trap states and the CTE binding energies which are increasing for bisPCBM and $PC_{71}BM$ as well. Thus, it might be possible that the CTS in the investigated MDMO-PPV blend systems does not form out between the donor HOMO and the actual acceptor LUMO, but rather between the donor HOMO and deeper lying acceptor trap states with respect to the acceptor LUMO (see Figure 8.6 for illustration). Since both bisPCBM and $PC_{71}BM$ possess deeper traps than $PC_{61}BM$, an increase of the CTE binding energies could then be expected for these two fullerene derivatives, an assumption which is supported by the experimental results.

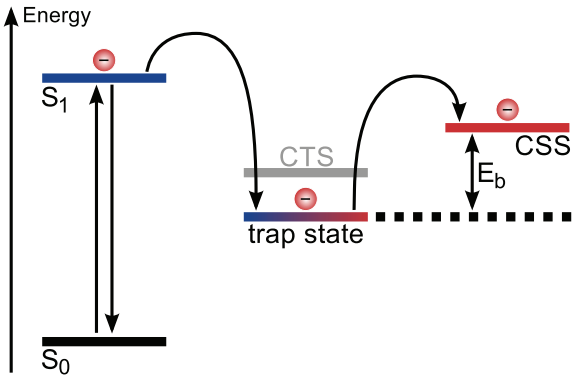

Figure 8.6: Possible impact of trap states on the CTE binding energy. Presumably, CTS can be formed with deeper lying acceptor trap states instead of the acceptor LUMO, leading to higher CTE binding energies for deeper traps.

In the context of the just presented approach to the explanation of the increasing CTE binding energies, it should be noted that a recent publication by Wetzelaer et al. [179] reports that CT emission in organic polymer–fullerene solar cells stems from free-carrier bimolecular recombination at the donor–acceptor interface instead of from a trap-mediated process. However, the authors base their statement on the detection of voltage dependent EL, making it not fully applicable to the here presented photoluminescence results due to the differences in the underlying processes. Following another recent publication by Tvingstedt et al. [100] who observed spectral differences in the PL and EL emission of the CTE, PL is mainly due to geminate recombination of CTE while EL originates from bimolecular recombination as a result of charge carrier injection and takes place at lower energies than PL. This also implies that PL and EL occur at different sites in the BHJ. Thus, PL is expected to stem from more spatially disordered, intimately mixed regions of the active layer which make it harder for the charge carriers to escape the potential of each other and consequently promote geminate CTE recombination. EL, on the other hand, can be attributed to the more spatially ordered BHJ regions which are easy to access for oppositely charged carriers. Coming back to speak of the publication of Wetzelaer et al., these considerations indicate that the main statement of the paper is certainly relevant to CTE recombination observed via EL but may not hold true for CTE recombination via PL. As a result, the increasing CTE binding energies observed in PL(F) measurements could still be due to CTS formation between donor HOMO and acceptor trap states, even if this assumption cannot be experimentally validated here.

8.3 Conclusions

Based on the hypothesis that a variation of the acceptor LUMO level might cause a variation of the CTE binding energy, integral PL(F) measurements were conducted on blends of MDMO-PPV:$PC_{61}BM$ 2:1, MDMO-PPV:bisPCBM 2:1 and MDMO-PPV:$PC_{71}BM$ 2:1. With the LUMO level of neat bisPCBM being approximately 0.1 eV higher than the one of neat $PC_{61}BM$ and neat $PC_{71}BM$, similar CTE binding energies were expected for MDMO-PPV blends with the latter two fullerene derivatives in contrast to a differing CTE binding energy for the bisPCBM blend. However, the experimentally determined CTE binding energies were found to increase from $PC_{61}BM$ over bisPCBM to $PC_{71}BM$, albeit it has to be noted that this rise is only slightly higher than the experimental error and strongly depends on the $\mu\tau$-product used for the Onsager–Braun fit. Still, it can be concluded that the acceptor LUMO level does not seem to have a major impact on the CTE binding energy. For the explanation of the observed increasing CTE binding energies, a correlation to the trap state levels of the neat fullerene derivatives as reported by Schafferhans et al. [178] comes to hand: For both bisPCBM and $PC_{71}BM$, higher trap densities and higher activation energies as compared to $PC_{61}BM$ were extracted from TSC measurements. Thus, the CTS observed in PL(F) experiments might not be formed between the donor HOMO and the actual acceptor LUMO, but rather between the donor HOMO and a deeper lying acceptor trap state with respect to the acceptor LUMO, resulting in the reported increase in $E_{b,CTE}$. It should be noted that this assumption is not disproven by the statement that CTE emission in polymer–fullerene solar cells is not a trap-mediated process made by Wetzelaer et al. [179], which is based on EL measurements and thus does not apply to the PL(F) experiments yielding the increased CTE binding energies.

9 Conclusions

9.1 Conclusions

The primary focus of this thesis was set on the investigation of the charge carrier photogeneration via intermediate charge transfer states (CTS) in organic bulk heterojunction (BHJ) solar cells, the latter of which present the most promising concept in the field of organic photovoltaics (OPV) to date. This goal was mainly pursued with the help of field dependent photoluminescence (PL(F)) measurements, probing the radiative recombination of relaxed charge transfer excitons (CTE) under the influence of an external electric field. For increasing field strengths, the amount of CTE which are able to overcome their coulombic binding energy and to dissociate is increasing as well so that as a consequence, the photoluminescence (PL) signal is reduced. The comparison of the obtained PL quenching curve to the theoretical dissociation probability as given by the Onsager–Braun model allows for the extraction of the respective exciton binding energy as one of the key parameters in the charge carrier photogeneration processes. The PL(F) technique was complemented by field dependent transient absorption (TA(F)) measurements, directly providing access to the charge carriers which were additionally generated due to the external electric field. In order to interpret the results obtained via PL(F) and TA(F), atomic force microscopy (AFM) and optically detected magnetic resonance (ODMR) were employed for the morphological characterization of the samples. All experiments were conducted on solar cell devices consisting of blends of the OPV work horse polymer MDMO-PPV and one of the fullerene derivatives $PC_{61}BM$, bisPCBM and $PC_{71}BM$ in various blend compositions, serving as reference systems for newly developed, state-of-the-art donor–acceptor blends.

In a first approach to the topic, the binding energies of both the CTE in a blend of MDMO-PPV:$PC_{61}BM$ 1:1 and the singlet exciton in neat MDMO-PPV were determined via excitation modulated PL(F) and set in comparison. As expected, the CTE binding energy $E_{b,CTE} = (201 \pm 18)$ meV was found to be much weaker than the one of the singlet exciton, $E_{b,S1} = (327 \pm 30)$ meV. Additional voltage modulated PL(F) measurements yielded similar results, supporting the validity of the obtained binding energies which are also in good agreement with literature values for comparable material sys-

tems. However, it should be noted that the choice of the $\mu\tau$-product proved to play a crucial role for the exact determination of the binding energies, which has to be kept in mind when adapting the PL(F) method to other material systems.

These first results were extended by investigating the CTE-mediated charge carrier photogeneration process for different MDMO-PPV:$PC_{61}BM$ blend ratios. PL(F) measurements on 4:1, 2:1 and 1:1 blends, i.e., with an increasing $PC_{61}BM$ load, revealed decreasing CTE binding energies of 318 meV, 237 meV and 201 meV under the assumption of a constant $\mu\tau$-product. This trend was found to qualitatively continue for the better OPV performing blend ratios of 1:2 and 1:4 which were studied with the help of TA(F) experiments. The morphological characterization of the investigated blend systems via AFM and ODMR uncovered a homogeneous surface and bulk structure for the 4:1 and 2:1 blends while the onset of a phase segregation was visible for the 1:1 blend. Distinct $PC_{61}BM$ domains governed the 1:2 and 1:4 blends. Taking all experimental findings into account, the conclusion was drawn that for the fullerene-poor blends, an effective dielectric constant which depends on the prevailing blend ratio is responsible for the observed CTE field dependence. For the fullerene-rich blends exhibiting a pronounced phase separation, however, both the dielectric constant and the CTE delocalization length have an impact on the CTE field behavior. Most significantly, these results stress the importance of a high dielectric constant for an efficient charge carrier photogeneration in OPV devices.

Finally, the CTE binding energies in MDMO-PPV blends with either $PC_{61}BM$, bisPCBM or $PC_{71}BM$ in a 2:1 blend ratio were determined in order to test the hypothesis that the raised LUMO level of bisPCBM as compared to the ones of $PC_{61}BM$ and $PC_{71}BM$ might have an impact on $E_{b,CTE}$. On the contrary, a slight increase of the CTE binding energy was observed with 237 meV for $PC_{61}BM$, 263 meV for bisPCBM and 280 meV for $PC_{71}BM$. This behavior might be related to trap states in the different fullerene derivatives. Both bisPCBM and $PC_{71}BM$ possess not only higher trap densities but also deeper traps than $PC_{61}BM$. These trap states might be involved in the formation of CTS with the donor HOMO which could be detected in PL(F) experiments. Albeit not being verifiable with the experimental methods at hand, the presented scheme might well serve as an explanation for the deviations in $E_{b,CTE}$ between the different fullerene derivatives.

All reported binding energies were evaluated within the Onsager–Braun framework, which was found to be suitable for the description of the experimentally observed field dependent CTE dissociation. Yet, no attempt was made to verify the predicted temperature dependence as one of the frequently criticized issues of the model, which might be a worthwhile topic for future studies. Moreover, as the role of the dielectric

constant for charge carrier photogeneration was highlighted by the blend ratio dependent experiments, a more thorough investigation of this aspect might be considered, using e.g. specially designed polymers with high dielectric constants such as poly[2-methoxy-5-(triethoxymethoxy)-1,4-phenylene vinylene] (PEO-PPV) and poly(2,5-bis-(triethoxymethoxy)-1,4-phenylene vinylene) (diPEO-PPV) or adding small amounts of nano-particles displaying a high ϵ_r such as TiO_2 to the photovoltaic blends. In general, the here presented results suggest relaxed CTE binding energies which exceed the thermal energy at room temperature by far, hinting at a hot CTE-mediated charge carrier photogeneration under standard low-field solar cell operating conditions, at least as far as the used MDMO-PPV based reference system is concerned. Consequently, a series of similar experiments on promising new material systems such as various low-bandgap copolymers may be an intriguing research topic, enhancing the understanding of the fundamental processes of photoinduced charge carrier generation and thus bringing OPV one step closer to a successful market implementation in the near future.

9.2 Zusammenfassung

Die vorliegende Arbeit diente der Untersuchung der photoinduzierten Ladungsträgergenerierung über Ladungstransferzustände (engl. „Charge Transfer States“, CTS) in organischen „Bulk Heterojunction“-Solarzellen, welche den zur Zeit vielversprechendsten Ansatz auf dem Gebiet der organischen Photovoltaik (OPV) darstellen. Um dieses Ziel zu erreichen, wurde hauptsächlich die experimentelle Methode der feldabhängigen Photolumineszenzmessung (PL(F)) eingesetzt, mit der die strahlende Rekombination von relaxierten Ladungstransfer-Exzitonen (engl. „Charge Transfer Excitons“, CTE) unter Einfluss eines externen elektrischen Feldes detektiert werden kann. Mit zunehmender Feldstärke steigt auch die Anzahl der CTE, die ihre Coulomb-Bindungsenergie überwinden können und dissoziieren, so dass das Photolumineszenzsignal absinkt. Durch einen Vergleich dieses Signals mit der theoretischen Dissoziationswahrscheinlichkeit nach dem Onsager–Braun-Modell lässt sich die Exzitonen-Bindungsenergie als wichtigen Faktor der Ladungsträgergenerierung bestimmen. Die PL(F)-Messungen wurden durch feldabhängige transiente Absorptionsexperimente (TA(F)) ergänzt, um direkten Zugang zu den Ladungsträgern zu haben, die zusätzlich durch das extern angelegte elektrische Feld generiert werden. Zur Interpretation der PL(F)- und TA(F)-Ergebnisse wurden außerdem Rasterkraftmikroskopie (AFM) und optisch detektierte Magnetresonanz (ODMR) angewandt, um Aufschluss über die zugrundeliegende Morphologie der untersuchten Proben zu gewinnen. Alle Experimente wurden an Solarzellen durchgeführt, deren aktive

Schichten aus einem Gemisch des etablierten OPV-Polymers MDMO-PPV mit einem der Fulleren-Derivate $PC_{61}BM$, bisPCBM oder $PC_{71}BM$ in unterschiedlichen Mischungsverhältnissen bestanden. Die verwendeten Materialien stellten damit ein Referenzsystem für neu entwickelte, hoch effiziente Donator–Akzeptor-Kombinationen dar.

Zunächst wurden die Bindungsenergien von sowohl dem CTE in MDMO-PPV:$PC_{61}BM$ 1:1 als auch dem Singulett-Exziton in reinem MDMO-PPV mit Hilfe der anregungsmodulierten PL(F) bestimmt und miteinander verglichen. Wie erwartet ergab sich dabei eine CTE-Bindungsenergie, welche mit $E_{b,CTE} = (201 \pm 18)$ meV wesentlich geringer ausfällt als die des Singulett-Exzitons mit $E_{b,S1} = (327 \pm 30)$ meV. Zusätzliche spannungsmodulierte PL(F)-Messungen führten zu vergleichbaren Resultaten und unterstützen somit die Belastbarkeit der bestimmten Bindungsenergien, welche zudem gut mit Literaturwerten für ähnliche Materialsysteme übereinstimmen. An dieser Stelle ist anzumerken, dass die Wahl des für die Berechnungen verwendeten $\mu\tau$-Produkts die erhaltenen Bindungsenergien in entscheidendem Maße beeinflusst. Dieser Aspekt sollte auch bei der zukünftigen Adaption der PL(F)-Technik für andere Materialsysteme berücksichtigt werden.

Die zuvor beschriebenen Messungen wurden in einem zweiten Schritt auf MDMO-PPV:$PC_{61}BM$-Gemische in unterschiedlichen Mischungsverhältnissen ausgeweitet. PL(F)-Messungen an Gemischen mit einem steigenden $PC_{61}BM$-Anteil von 4:1, 2:1 und 1:1 ergaben unter der Annahme eines konstanten $\mu\tau$-Produktes in dieser Reihenfolge sinkende CTE-Bindungsenergien von 318 meV, 237 meV und 201 meV — ein Trend, der in TA(F)-Experimenten auch zumindest qualitativ für die aus photovoltaischer Sicht effizienteren 1:2- und 1:4-Gemische anhielt. Die morphologische Charakterisierung der untersuchten Systeme durch AFM und ODMR ergab eine homogene Struktur für das 4:1- und 2:1-Mischungsverhältnis. Demgegenüber wurde im 1:1-Gemisch der Beginn einer Phasenseparation sichtbar, welche dann für die 1:2- und die 1:4-Mischung mit deutlich sichtbaren $PC_{61}BM$-Domänen stark ausgeprägt war. Unter Einbeziehung aller experimentellen Ergebnisse konnte darauf geschlossen werden, dass in den Gemischen mit geringem Fulleren-Anteil die vom Mischungsverhältnis abhängige, effektive dielektrische Konstante für das beobachtete elektrische Feldverhalten der CTE verantwortlich ist. Im Gegensatz dazu kann für Gemische mit einem höheren Anteil an Fullerenen und einer erkennbaren Phasenseparation sowohl von einem Einfluss der dielektrischen Konstante als auch von einem Einfluss der CTE-Delokalisationslänge auf die Feldabhängigkeit der CTE ausgegangen werden. Diese Resultate demonstrieren die große Bedeutung einer hohen dielektrischen Konstante im Bezug auf eine effiziente Ladungsträgergenerierung in organischen Solarzellen.

Schließlich wurden die CTE-Bindungsenergien in Gemischen aus MDMO-PPV und einem der Fulleren-Derivate $PC_{61}BM$, bisPCBM oder $PC_{71}BM$ in einem 2:1-Verhältnis bestimmt. Ziel hierbei war es, die Hypothese zu überprüfen, dass das im Vergleich zu $PC_{61}BM$ und $PC_{71}BM$ höhere LUMO-Niveau von bisPCBM einen Einfluss auf die Bindungsenergie des CTE haben könnte. Entgegen dieser Annahme wurde für $E_{b,CTE}$ jedoch ein leichter Anstieg von 237 meV für $PC_{61}BM$ über 263 meV für bisPCBM bis hin zu 280 meV für $PC_{71}BM$ festgestellt. Das beobachtete Verhalten könnte auf die Fallenzustände der Fulleren-Derivate zurückzuführen sein, die sowohl für bisPCBM als auch für $PC_{71}BM$ eine höhere Dichte und höhere Aktivierungsenergien besitzen als für $PC_{61}BM$. Eben solche Akzeptor-Fallenzustände könnten mit dem HOMO-Niveau des Donators CTS ausbilden, welche dann durch PL(F) detektiert werden. Wenn auch das vorgestellte Szenario nicht durch die verfügbaren experimentellen Methoden verifiziert werden konnte, stellt es doch eine plausible Erklärung für die Abweichung zwischen den CTE-Bindungsenergien unterschiedlicher Fulleren-Derivate dar.

Zusammenfassend betrachtet verdeutlicht die vorliegende Arbeit die Eignung der Onsager–Braun-Theorie für die Beschreibung der experimentell beobachteten feldabhängigen CTE-Dissoziation. Es sei an dieser Stelle darauf hingewiesen, dass die im Modell angenommene und häufig kritisierte Temperaturabhängigkeit nicht überprüft wurde, was jedoch ein Ansatzpunkt für zukünftige Studien sein könnte. Auch die eingehendere Untersuchung von Materialsystemen mit hohen dielektrischen Konstanten, die z.B. durch speziell synthetisierte Polymere wie poly[2-methoxy-5-(triethoxymethoxy)-1,4-phenylene vinylene] (PEO-PPV) und poly(2,5-bis-(triethoxymethoxy)-1,4-phenylene vinylene) (diPEO-PPV) oder durch die Beimischung geringer Mengen an Nanopartikeln wie TiO_2 zur aktiven Schicht der Solarzellen erreicht werden können, erscheint im Hinblick auf die dargestellte herausragende Rolle der dielektrischen Konstante durchaus lohnenswert. Im Allgemeinen lassen die hier beschriebenen Messungen und Ergebnisse auf Bindungsenergien der relaxierten CTE schließen, die weit über der bei Raumtemperatur erreichten thermischen Energie liegen. Dies deutet auf einen Ladungsträgergenerierungsprozess hin, der bei den unter normalen OPV-Betriebsbedingungen vorliegenden, relativ schwachen elektrischen Feldern hauptsächlich über heiße CTE abläuft — zumindest im Bezug auf das verwendete Referenzmaterialsystem. Folglich könnte eine ähnliche Versuchsreihe an neuen Materialsystemen z.B. unter Verwendung von sogenannten „Low-Bandgap“-Polymeren ein vielversprechendes Forschungsvorhaben darstellen, welches das Verständnis der fundamentalen Prozesse der photoinduzierten Ladungsträgergenerierung erweitern und somit die OPV einen Schritt näher an eine erfolgreiche Markteinführung bringen könnte.

Bibliography

[1] REN21 - Renewable Energy Policy Network for the 21st Century. Renewables 2013 - Global status report (2013). URL: http://www.ren21.net/Portals/0/documents/Resources/GSR/2013/GSR2013_lowres.pdf, date accessed: June 29th, 2013.

[2] Gesetz über die Einspeisung von Strom aus erneuerbaren Energien in das öffentliche Netz (Stromeinspeisungsgesetz) (DE), BGBl. I S. 2633, December 7th, 1990.

[3] Gesetz für den Vorrang Erneuerbarer Energien (Erneuerbare-Energien-Gesetz - EEG) (DE), BGBl. I S. 305, March 29th, 2000.

[4] AGEE-Stat c/o Zentrum für Sonnenenergie- und Wasserstoff-Forschung Baden-Württemberg (ZSW). Erneuerbare Energien 2012 (2013). URL: http://www.bmu.de/fileadmin/Daten_BMU/Pools/Broschueren/20130430_erneuerbare_energien_2012_bf.pdf, date accessed: June 29th, 2013.

[5] Gesetz zur Änderung des Rechtsrahmens für Strom aus solarer Strahlungsenergie und weiteren Änderungen im Recht der erneuerbaren Energien (PV-Novelle) (DE), BGBl. I S. 1754, August 23th, 2012.

[6] A. E. Becquerel. Mémoire sur les effets électriques produits sous l'influence des rayons solaires. *Comt. Rend. Acad. Sci.*, **9**, 561 (1839).

[7] D. M. Chapin, C. S. Fuller and G. L. Pearson. A new silicon p-n junction photocell for converting solar radiation into electrical power. *J. Appl. Phys.*, **25**, 676 (1954). doi: 10.1063/1.1721711.

[8] M. A. Green, K. Emery, Y. Hishikawa, W. Warta and E. D. Dunlop. Solar cell efficiency tables (version 41). *Prog. Photovolt: Res. Appl.*, **21**, 1 (2013). doi: 10.1002/pip.2352.

[9] W. Shockley and H. J. Queisser. Detailed balance limit of efficiency of p-n junction solar cells. *J. Appl. Phys.*, **32**, 510 (1961). doi: 10.1063/1.1736034.

[10] BINE Informationsdienst. FIZ Karlsruhe. Photovoltaik - Innovationen (2011). URL: http://www.bine.info/fileadmin/content/Publikationen/Themen-Infos/II_2011/TI_II_11_internetx.pdf, date accessed: June 29th, 2013.

[11] Web of Knowledge. URL: www.webofknowledge.com, search topic "organic photovoltaics", date accessed: June 29th, 2013.

[12] H. Shirakawa, E. J. Louis, A. G. MacDiarmid, C. K. Chiang and A. J. Heeger. Synthesis of electrically conducting organic polymers: Halogen derivatives of polyacetylene, $(CH)_x$. *J. Chem. Soc., Chem. Comm.*, 578 (1977). doi: 10.1039/c39770000578.

[13] C. Deibel and V. Dyakonov. Polymer–fullerene bulk heterojunction solar cells. *Rep. Prog. Phys.*, **73**, 096401 (2010). doi: 10.1088/0034-4885/73/9/096401.

[14] R. Gaudiana. Third-generation photovoltaic technology - The potential for low-cost solar energy conversion. *J. Phys. Chem. Lett.*, **1**, 1288 (2010). doi: 10.1021/jz100290q.

[15] Eight19. Company profile. URL: www.eight19.com, date accessed: July 6th, 2013.

[16] Heliatek. Pressemitteilung: Neuer Weltrekord für organische Solarzellen: Heliatek behauptet sich mit 12 % Zelleffizienz als Technologieführer (2013). URL: http://www.heliatek.com/wp-content/uploads/2013/01/130116_PM_Heliatek-erzielt-Weltrekordeffizienz-fuer-OPV.pdf, date accessed: July 6th, 2013.

[17] C. J. Brabec, S. Gowrisanker, J. J. M. Halls, D. Laird, S. Jia and S. P. Williams. Polymer-fullerene bulk-heterojunction solar cells. *Adv. Mater.*, **22**, 3839 (2010). doi: 10.1002/adma.200903697.

[18] W. Brütting, editor. *Physics of organic semiconductors*. Wiley-VCH, Weinheim, 1st edition (2005).

[19] M. Schwoerer and H. C. Wolf. *Organische Molekulare Festkörper*. Wiley-VCH, Weinheim (2005).

[20] K. Leo. Organic semiconductor world. URL: www.orgworld.de, date accessed: February 2nd, 2013.

[21] R. E. Peierls. *Quantum theory of solids*. Oxford University Press, London (1955).

[22] N. J. Turro, V. Ramamurthy and J. C. Scaiano. *Modern molecular photochemistry of organic molecules*. University Science Books, Sausalito (2010).

[23] D. Hertel and H. Bässler. Photoconduction in amorphous organic solids. *Chem. Phys. Chem.*, **9**, 666 (2008). doi: 10.1002/cphc.200700575.

[24] G. A. Chamberlain. Organic solar cells: A review. *Solar Cells*, **8**, 47 (1983). doi: 10.1016/0379-6787(83)90039-X.

[25] C. W. Tang. Two-layer organic photovoltaic cell. *Appl. Phys. Lett.*, **48**, 183 (1986). doi: 10.1063/1.96937.

[26] G. Yu, J. Gao, J. C. Hummelen, F. Wudl and A. J. Heeger. Polymer photovoltaic cells: Enhanced efficiencies via a network of internal donor-acceptor heterojunctions. *Science*, **270**, 1789 (1995). doi: 10.1126/science.270.5243.1789.

[27] D. Mühlbacher, M. Scharber, M. Morana, Z. Zhu, D. Waller, R. Gaudiana and C. Brabec. High photovoltaic performance of a low-bandgap polymer. *Adv. Mater.*, **18**, 2884 (2006). doi: 10.1002/adma.200600160.

[28] Y. Liang, Z. Xu, J. Xia, S.-T. Tsai, Y. Wu, G. Li, C. Ray and L. Yu. For the bright future - Bulk heterojunction polymer solar cells with power conversion efficiency of 7.4%. *Adv. Mater.*, **22**, E135 (2010). doi: 10.1002/adma.200903528.

[29] M. C. Scharber, M. Koppe, J. Gao, F. Cordella, M. A. Loi, P. Denk, M. Morana, H.-J. Egelhaaf, K. Forberich, G. Dennler, R. Gaudiana, D. Waller, Z. Zhu, X. Shi and C. J. Brabec. Influence of the bridging atom on the performance of a low-bandgap bulk heterojunction solar cell. *Adv. Mater.*, **22**, 367 (2010). doi: 10.1002/adma.200900529.

[30] S. E. Shaheen, C. J. Brabec, N. S. Sariciftci, F. Padinger, T. Fromherz and J. C. Hummelen. 2.5% efficient organic plastic solar cells. *Appl. Phys. Lett.*, **78**, 841 (2001). doi: 10.1063/1.1345834.

[31] J. K. J. van Duren, X. Yang, J. Loos, C. W. T. Bulle-Lieuwma, A. B. Sieval, J. C. Hummelen and R. A. J. Janssen. Relating the morphology of poly(*p*-phenylene vinylene)/methanofullerene blends to solar-cell performance. *Adv. Funct. Mater.*, **14**, 425 (2004). doi: 10.1002/adfm.200305049.

[32] P. Vanlaeke, A. Swinnen, I. Haeldermans, G. Vanhoyland, T. Aernouts, D. Cheyns, C. Deibel, J. D'Haen, P. Heremans, J. Poortmans and J. V. Manca. P3HT/PCBM bulk heterojunction solar cells: Relation between morphology and electro-optical characteristics. *Sol. Energ. Mat. Sol. C.*, **90**, 2150 (2006). doi: 10.1016/j.solmat.2006.02.010.

[33] F. Padinger, R. S. Rittberger and N. S. Sariciftci. Effects of postproduction treatment on plastic solar cells. *Adv. Funct. Mater.*, **13**, 85 (2003). doi: 10.1002/adfm.200390011.

[34] J. Peet, J. Y. Kim, N. E. Coates, W. L. Ma, D. Moses, A. J. Heeger and G. C. Bazan. Efficiency enhancement in low-bandgap polymer solar cells by processing with alkane dithiols. *Nature Mater.*, **6**, 497 (2007). doi: 10.1038/nmat1928.

[35] J. Schafferhans. Investigation of defect states in organic semiconductors: Towards long term stable materials for organic photovoltaics. Dissertation, Julius-Maximilians-Universität Würzburg (2011).

[36] S. J. Martin, D. D. C. Bradley, P. A. Lane, H. Mellor and P. L. Burn. Linear and nonlinear optical properties of the conjugated polymers PPV and MEH-PPV. *Phys. Rev. B*, **59**, 15133 (1999). doi: 10.1103/PhysRevB.59.15133.

[37] H. Hoppe, N. Arnold, N. S. Sariciftci and D. Meissner. Modeling the optical absorption within conjugated polymer/fullerene-based bulk-heterojunction organic solar cells. *Sol. Energ. Mat. Sol. C.*, **80**, 105 (2003). doi: 10.1016/S0927-0248(03)00137-5.

[38] E. Lioudakis, A. Othonos, I. Alexandrou and Y. Hayashi. Optical properties of conjugated poly(3-hexylthiophene)/[6,6]-phenylC_{61}-butyric acid methyl ester composites. *J. Appl. Phys.*, **102**, 083104 (2007). doi: 10.1063/1.2799049.

[39] A. V. Gavrilenko, T. D. Matos, C. E. Bonner, S.-S. Sun, C. Zhang and V. I. Gavrilenko. Optical absorption of poly(thienylene vinylene)-conjugated polymers: Experiment and first principle theory. *J. Phys. Chem. C*, **112**, 7908 (2008). doi: 10.1021/jp711772z.

[40] R. Schueppel, K. Schmidt, C. Uhrich, K. Schulze, D. Wynands, J. L. Brédas, E. Brier, E. Reinold, H.-B. Bu, P. Baeuerle, B. Maennig, M. Pfeiffer and K. Leo. Optimizing organic photovoltaics using tailored heterojunctions: A photoinduced absorption study of oligothiophenes with low band gaps. *Phys. Rev. B*, **77**, 085311 (2008). doi: 10.1103/PhysRevB.77.085311.

[41] M. M. Wienk, J. M. Kroon, W. J. H. Verhees, J. Knol, J. C. Hummelen, P. A. van Hal and R. A. J. Janssen. Efficient methano[70]fullerene/MDMO-PPV bulk heterojunction photovoltaic cells. *Angew. Chem. Int. Ed.*, **42**, 3371 (2003). doi: 10.1002/anie.200351647.

[42] S. Cook, R. Katoh and A. Furube. Ultrafast studies of charge generation in PCBM:P3HT blend films following excitation of the fullerene PCBM. *J. Phys. Chem. C*, **113**, 2547 (2009). doi: 10.1021/jp8050774.

[43] X. Wang, E. Perzon, F. Oswald, F. Langa, S. Admassie, M. R. Andersson and O. Inganäs. Enhanced photocurrent spectral response in low-bandgap polyfluorene and C_{70}-derivative-based solar cells. *Adv. Funct. Mater.*, **15**, 1665 (2005). doi: 10.1002/adfm.200500114.

[44] W. J. D. Beenken. Excitons in conjugated polymers: Do we need a paradigma change? *Phys. Status Solidi A*, **206**, 2750 (2009). doi: 10.1002/pssa.200925297.

[45] L. W. Barbour, R. D. Pensack, M. Hegadorn, S. Arzhantsev and J. B. Asbury. Excitation transport and charge separation in an organic photovoltaic material: Watching excitations diffuse to interfaces. *J. Phys. Chem. C*, **112**, 3926 (2008). doi: 10.1021/jp0759628.

[46] E. Collini and G. D. Scholes. Coherent intrachain energy migration in a conjugated polymer at room temperature. *Science*, **323**, 369 (2009). doi: 10.1126/science.1164016.

[47] L. Lüer, H.-J. Egelhaaf, D. Oelkrug, G. Cerullo, G. Lanzani, B.-H. Huisman and D. de Leeuw. Oxygen-induced quenching of photoexcited states in polythiophene films. *Org. Electron.*, **5**, 83 (2004). doi: 10.1016/j.orgel.2003.12.005.

[48] P. E. Shaw, A. Ruseckas and I. D. W. Samuel. Exciton diffusion measurements in poly(3-hexylthiophene). *Adv. Mater.*, **20**, 3516 (2008). doi: 10.1002/adma.200800982.

[49] T. Stübinger and W. Brütting. Exciton diffusion and optical interference in organic donor–acceptor photovoltaic cells. *J. Appl. Phys.*, **90**, 3632 (2001). doi: 10.1063/1.1394920.

[50] A. C. Morteani, R. H. Friend and C. Silva. Exciton trapping at heterojunctions in polymer blends. *J. Chem. Phys.*, **122**, 244906 (2005). doi: 10.1063/1.1924504.

[51] C. Yin, T. Kietzke, D. Neher and H.-H. Hörhold. Photovoltaic properties and exciplex emission of polyphenylenevinylene-based blend solar cells. *Appl. Phys. Lett.*, **90**, 092117 (2007). doi: 10.1063/1.2710474.

[52] C. Deibel, T. Strobel and V. Dyakonov. Role of the charge transfer state in organic donor-acceptor solar cells. *Adv. Mater.*, **22**, 4097 (2010). doi: 10.1002/adma.201000376.

[53] N. S. Sariciftci, L. Smilowitz, A. J. Heeger and F. Wudl. Photoinduced electron transfer from a conducting polymer to buckminsterfullerene. *Science*, **258**, 1474 (1992). doi: 10.1126/science.258.5087.1474.

[54] I.-W. Hwang, D. Moses and A. J. Heeger. Photoinduced carrier generation in P3HT/PCBM bulk heterojunction materials. *J. Phys. Chem. C*, **112**, 4350 (2008). doi: 10.1021/jp075565x.

[55] H. Ohkita, S. Cook, Y. Astuti, W. Duffy, S. Tierney, W. Zhang, M. Heeney, I. McCulloch, J. Nelson, D. D. C. Bradley and J. R. Durrant. Charge carrier formation in polythiophene/fullerene blend films studied by transient absorption spectroscopy. *J. Am. Chem. Soc.*, **130**, 3030 (2008). doi: 10.1021/ja076568q.

[56] D. Veldman, S. C. J. Meskers and R. A. J. Janssen. The energy of charge-transfer states in electron donor-acceptor blends: Insight into the energy losses in organic solar cells. *Adv. Funct. Mater.*, **19**, 1939 (2009). doi: 10.1002/adfm.200900090.

[57] D. Veldman, Ö. Ipek, S. C. J. Meskers, J. Sweelssen, M. M. Koetse, S. C. Veenstra, J. M. Kroon, S. S. van Bavel, J. Loos and R. A. J. Janssen. Compositional and electric field dependence of the dissociation of charge transfer excitons in alternating polyfluorene copolymer/fullerene blends. *J. Am. Chem. Soc.*, **130**, 7721 (2008). doi: 10.1021/ja8012598.

[58] E. L. Frankevich, A. A. Lymarev, I. Sokolik, F. E. Karasz, S. Blumstengel, R. H. Baughman and H. H. Hörhold. Polaron-pair generation in poly(phenylene vinylenes). *Phys. Rev. B*, **46**, 9320 (1992). doi: 10.1103/PhysRevB.46.9320.

[59] T. M. Clarke and J. R. Durrant. Charge photogeneration in organic solar cells. *Chem. Rev.*, **110**, 6736 (2010). doi: 10.1021/cr900271s.

[60] K. Vandewal, A. Gadisa, W. D. Oosterbaan, S. Bertho, F. Banishoeib, I. Van Severen, L. Lutsen, T. J. Cleij, D. Vanderzande and J. V. Manca. The relation between open-circuit voltage and the onset of photocurrent generation by charge-transfer absorption in polymer:fullerene bulk heterojunction solar cells. *Adv. Funct. Mater.*, **18**, 2064 (2008). doi: 10.1002/adfm.200800056.

[61] K. Hasharoni, M. Keshavarz-K., A. Sastre, R. González, C. Bellavia-Lund, Y. Greenwald, T. Swager, F. Wudl and A. J. Heeger. Near IR photoluminescence in mixed films of conjugated polymers and fullerenes. *J. Chem. Phys.*, **107**, 2308 (1997). doi: 10.1063/1.474607.

[62] A. C. Morteani, P. Sreearunothai, L. M. Herz, R. H. Friend and C. Silva. Exciton regeneration at polymeric semiconductor heterojunctions. *Phys. Rev. Lett.*, **92**, 247402 (2004). doi: 10.1103/PhysRevLett.92.247402.

[63] L. Goris, A. Poruba, L. Hod'ákova, M. Vaněček, K. Haenen, M. Nesládek, P. Wagner, D. Vanderzande, L. De Schepper and J. V. Manca. Observation of the subgap optical absorption in polymer-fullerene blend solar cells. *Appl. Phys. Lett.*, **88**, 052113 (2006). doi: 10.1063/1.2171492.

[64] J. J. Benson-Smith, L. Goris, K. Vandewal, K. Haenen, J. V. Manca, D. Vanderzande, D. D. C. Bradley and J. Nelson. Formation of a ground-state charge-transfer complex in polyfluorene/[6,6]-phenyl-C_{61} butyric acid methyl ester (PCBM) blend films and its role in the function of polymer/PCBM solar cells. *Adv. Funct. Mater.*, **17**, 451 (2007). doi: 10.1002/adfm.200600484.

[65] M. A. Loi, S. Toffanin, M. Muccini, M. Forster, U. Scherf and M. Scharber. Charge transfer excitons in bulk heterojunctions of a polyfluorene copolymer and a fullerene derivative. *Adv. Funct. Mater.*, **17**, 2111 (2007). doi: 10.1002/adfm.200601098.

[66] V. Dyakonov, G. Rösler, M. Schwoerer and E. L. Frankevich. Evidence for triplet interchain polaron pairs and their transformations in polyphenylenevinylene. *Phys. Rev. B*, **56**, 3852 (1997). doi: 10.1103/PhysRevB.56.3852.

[67] H. Bässler. Charge transport in disordered organic photoconductors. *Phys. Status Solidi B*, **175**, 15 (1993). doi: 10.1002/pssb.2221750102.

[68] P. W. M. Blom, M. J. M. de Jong and M. G. van Munster. Electric-field and temperature dependence of the hole mobility in poly(*p*-phenylene vinylene). *Phys. Rev. B*, **55**, R656 (1997). doi: 10.1103/PhysRevB.55.R656.

[69] H. Sirringhaus. Device physics of solution-processed organic field-effect transistors. *Adv. Mater.*, **17**, 2411 (2005). doi: 10.1002/adma.200501152.

[70] V. Coropceanu, J. Cornil, D. A. da Silva Filho, Y. Olivier, R. Silbey and J.-L. Brédas. Charge transport in organic semiconductors. *Chem. Rev.*, **107**, 926 (2007). doi: 10.1021/cr050140x.

[71] S. D. Baranovskii, H. Cordes, F. Hensel and G. Leising. Charge-carrier transport in disordered organic solids. *Phys. Rev. B*, **62**, 7934 (2000). doi: 10.1103/PhysRevB.62.7934.

[72] D. Monroe. Hopping in exponential band tails. *Phys. Rev. Lett.*, **54**, 146 (1985). doi: 10.1103/PhysRevLett.54.146.

[73] V. I. Arkhipov, E. V. Emelianova and G. J. Adriaenssens. Effective transport energy versus the energy of most probable jumps in disordered hopping systems. *Phys. Rev. B*, **64**, 125125 (2001). doi: 10.1103/PhysRevB.64.125125.

[74] R. Schmechel and H. von Seggern. Electronic traps in organic transport layers. *Phys. Status Solidi A*, **201**, 1215 (2004). doi: 10.1002/pssa.200404343.

[75] R. J. O. M. Hoofman, M. P. de Haas, L. D. A. Siebbeles and J. M. Warman. Highly mobile electrons and holes on isolated chains of the semiconducting polymer poly(phenylene vinylene). *Nature*, **392**, 54 (1998). doi: 10.1038/32118.

[76] T. J. Savenije, J. E. Kroeze, M. M. Wienk, J. M. Kroon and J. M. Warman. Mobility and decay kinetics of charge carriers in photoexcited PCBM/PPV blends. *Phys. Rev. B*, **69**, 155205 (2004). doi: 10.1103/PhysRevB.69.155205.

[77] J. M. Warman, M. P. de Haas, T. D. Anthopoulos and D. M. de Leeuw. The negative effect of high-temperature annealing on charge-carrier lifetimes in microcrystalline PCBM. *Adv. Mater.*, **18**, 2294 (2006). doi: 10.1002/adma.200600554.

[78] C. Waldauf, M. Morana, P. Denk, P. Schilinsky, K. Coakley, S. A. Choulis and C. J. Brabec. Highly efficient inverted organic photovoltaics using solution based titanium oxide as electron selective contact. *Appl. Phys. Lett.*, **89**, 233517 (2006). doi: 10.1063/1.2402890.

[79] C. Yin, B. Pieper, B. Stiller, T. Kietzke and D. Neher. Charge carrier generation and electron blocking at interlayers in polymer solar cells. *Appl. Phys. Lett.*, **90**, 133502 (2007). doi: 10.1063/1.2715029.

[80] A. W. Hains, J. Liu, A. B. F. Martinson, M. D. Irwin and T. J. Marks. Anode interfacial tuning via electron-blocking/hole-transport layers and indium tin oxide surface treatment in bulk-heterojunction organic photovoltaic cells. *Adv. Funct. Mater.*, **20**, 595 (2010). doi: 10.1002/adfm.200901045.

[81] J. H. Lee, S. Cho, A. Roy, H.-T. Jung and A. J. Heeger. Enhanced diode characteristics of organic solar cells using titanium suboxide electron transport layer. *Appl. Phys. Lett.*, **96**, 163303 (2010). doi: 10.1063/1.3409116.

[82] J. Subbiah, D. Y. Kim, M. Hartel and F. So. MoO_3/poly(9,9-dioctylfluorene-co-N-[4-(3-methylpropyl)]-diphenylamine) double-interlayer effect on polymer solar cells. *Appl. Phys. Lett.*, **96**, 063303 (2010). doi: 10.1063/1.3310013.

[83] M. Mingebach. Photocurrent in organic solar cells. Dissertation, Julius-Maximilians-Universität Würzburg (2012).

[84] M. C. Scharber, D. Mühlbacher, M. Koppe, P. Denk, C. Waldauf, A. J. Heeger and C. J. Brabec. Design rules for donors in bulk-heterojunction solar cells — Towards 10 % energy-conversion efficiency. *Adv. Mater.*, **18**, 789 (2006). doi: 10.1002/adma.200501717.

[85] A. Gadisa, M. Svensson, M. R. Andersson and O. Inganäs. Correlation between oxidation potential and open-circuit voltage of composite solar cells based on blends of polythiophenes/fullerene derivative. *Appl. Phys. Lett.*, **84**, 1609 (2004). doi: 10.1063/1.1650878.

[86] K. Tvingstedt, K. Vandewal, A. Gadisa, F. Zhang, J. Manca and O. Inganäs. Electroluminescence from charge transfer states in polymer solar cells. *J. Am. Chem. Soc.*, **131**, 11819 (2009). doi: 10.1021/ja903100p.

[87] K. Vandewal, K. Tvingstedt, A. Gadisa, O. Inganäs and J. V. Manca. On the origin of the open-circuit voltage of polymer-fullerene solar cells. *Nature Mater.*, **8**, 904 (2009). doi: 10.1038/nmat2548.

[88] K. Vandewal, K. Tvingstedt, A. Gadisa, O. Inganäs and J. V. Manca. Relating the open-circuit voltage to interface molecular properties of donor:acceptor bulk heterojunction solar cells. *Phys. Rev. B*, **81**, 125204 (2010). doi: 10.1103/PhysRevB.81.125204.

[89] V. Shrotriya, G. Li, Y. Yao, T. Moriarty, K. Emery and Y. Yang. Accurate measurement and characterization of organic solar cells. *Adv. Funct. Mater.*, **16**, 2016 (2006). doi: 10.1002/adfm.200600489.

[90] Z. He, C. Zhong, S. Su, M. Xu, H. Wu and Y. Cao. Enhanced power-conversion efficiency in polymer solar cells using an inverted device structure. *Nature Photon.*, **6**, 591 (2012). doi: 10.1038/nphoton.2012.190.

[91] M. Hallermann, I. Kriegel, E. Da Como, J. M. Berger, E. von Hauff and J. Feldmann. Charge transfer excitons in polymer/fullerene blends: The role of morphology and polymer chain conformation. *Adv. Funct. Mater.*, **19**, 3662 (2009). doi: 10.1002/adfm.200901398.

[92] T. Drori, C.-X. Sheng, A. Ndobe, S. Singh, J. Holt and Z. V. Vardeny. Below-gap excitation of π-conjugated polymer-fullerene blends: Implications for bulk organic

heterojunction solar cells. *Phys. Rev. Lett.*, **101**, 037401 (2008). doi: 10.1103/PhysRevLett.101.037401.

[93] C. Deibel, T. Strobel and V. Dyakonov. Origin of the efficient polaron-pair dissociation in polymer-fullerene blends. *Phys. Rev. Lett.*, **103**, 036402 (2009). doi: 10.1103/PhysRevLett.103.036402.

[94] P. Peumans and S. R. Forrest. Separation of geminate charge-pairs at donor–acceptor interfaces in disordered solids. *Chem. Phys. Lett.*, **398**, 27 (2004). doi: 10.1016/j.cplett.2004.09.030.

[95] M. Muntwiler, Q. Yang, W. A. Tisdale and X.-Y. Zhu. Coulomb barrier for charge separation at an organic semiconductor interface. *Phys. Rev. Lett.*, **101**, 196403 (2008). doi: 10.1103/PhysRevLett.101.196403.

[96] J.-L. Brédas, J. E. Norton, J. Cornil and V. Coropceanu. Molecular understanding of organic solar cells: The challenges. *Acc. Chem. Res.*, **42**, 1691 (2009). doi: 10.1021/ar900099h.

[97] S. De, T. Pascher, M. Maiti, K. G. Jespersen, T. Kesti, F. Zhang, O. Inganäs, A. Yartsev and V. Sundström. Geminate charge recombination in alternating polyfluorene copolymer/fullerene blends. *J. Am. Chem. Soc.*, **129**, 8466 (2007). doi: 10.1021/ja068909q.

[98] M. Hallermann, S. Haneder and E. Da Como. Charge-transfer states in conjugated polymer/fullerene blends: Below-gap weakly bound excitons for polymer photovoltaics. *Appl. Phys. Lett.*, **93**, 053307 (2008). doi: 10.1063/1.2969295.

[99] H. Kim, J. Y. Kim, S. H. Park, K. Lee, Y. Jin, J. Kim and H. Suh. Electroluminescence in polymer-fullerene photovoltaic cells. *Appl. Phys. Lett.*, **86**, 183502 (2005). doi: 10.1063/1.1924869.

[100] K. Tvingstedt, K. Vandewal, F. Zhang and O. Inganäs. On the dissociation efficiency of charge transfer excitons and Frenkel excitons in organic solar cells: A luminescence quenching study. *J. Phys. Chem. C*, **114**, 21824 (2010). doi: 10.1021/jp107587h.

[101] T. Offermans, P. A. van Hal, S. C. J. Meskers, M. M. Koetse and R. A. J. Janssen. Exciplex dynamics in a blend of π-conjugated polymers with electron donating and accepting properties: MDMO-PPV and PCNEPV. *Phys. Rev. B*, **72**, 045213 (2005). doi: 10.1103/PhysRevB.72.045213.

[102] D. Moses, A. Dogariu and A. J. Heeger. Ultrafast detection of charged photocarriers in conjugated polymers. *Phys. Rev. B*, **61**, 9373 (2000). doi: 10.1103/PhysRevB.61.9373.

[103] I. A. Howard and F. Laquai. Optical probes of charge generation and recombination in bulk heterojunction organic solar cells. *Macromol. Chem. Phys.*, **211**, 2063 (2010). doi: 10.1002/macp.201000353.

[104] D. Jarzab, F. Cordella, J. Gao, M. Scharber, H.-J. Egelhaaf and M. A. Loi. Low-temperature behaviour of charge transfer excitons in narrow-bandgap polymer-based bulk heterojunctions. *Adv. Energy Mater.*, **1**, 604 (2011). doi: 10.1002/aenm.201100083.

[105] F. Provencher, M. Sakowicz, C.-N. Brosseau, G. Latini, S. Beaupré, M. Leclerc, L. X. Reynolds, S. A. Haque, R. Leonelli and C. Silva. Slow geminate-charge-pair recombination dynamics at polymer:fullerene heterojunctions in efficient organic solar cells. *J. Polym. Sci. Part B: Polym. Phys.*, **50**, 1395 (2012). doi: 10.1002/polb.23139.

[106] H. van Eersel, R. A. J. Janssen and M. Kemerink. Mechanism for efficient photoinduced charge separation at disordered organic heterointerfaces. *Adv. Funct. Mater.*, **22**, 2700 (2012). doi: 10.1002/adfm.201200249.

[107] M. Tong, N. E. Coates, D. Moses, A. J. Heeger, S. Beaupré and M. Leclerc. Charge carrier photogeneration and decay dynamics in the poly(2,7-carbazole) copolymer PCDTBT and in bulk heterojunction composites with $PC_{70}BM$. *Phys. Rev. B*, **81**, 125210 (2010). doi: 10.1103/PhysRevB.81.125210.

[108] J. Lee, K. Vandewal, S. R. Yost, M. E. Bahlke, L. Goris, M. A. Baldo, J. V. Manca and T. Van Voorhis. Charge transfer state versus hot exciton dissociation in polymer-fullerene blended solar cells. *J. Am. Chem. Soc.*, **132**, 11878 (2010). doi: 10.1021/ja1045742.

[109] L. Onsager. Initial recombination of ions. *Phys. Rev.*, **54**, 554 (1938). doi: 10.1103/PhysRev.54.554.

[110] C. L. Braun. Electric field assisted dissociation of charge transfer states as a mechanism of photocarrier production. *J. Chem. Phys.*, **80**, 4157 (1984). doi: 10.1063/1.447243.

[111] C. Deibel, D. Mack, J. Gorenflot, A. Schöll, S. Krause, F. Reinert, D. Rauh and V. Dyakonov. Energetics of excited states in the conjugated polymer

poly(3-hexylthiophene). *Phys. Rev. B*, **81**, 085202 (2010). doi: 10.1103/PhysRevB.81.085202.

[112] V. D. Mihailetchi, L. J. A. Koster, J. C. Hummelen and P. W. M. Blom. Photocurrent generation in polymer-fullerene bulk heterojunctions. *Phys. Rev. Lett.*, **93**, 216601 (2004). doi: 10.1103/PhysRevLett.93.216601.

[113] L. J. A. Koster, E. C. P. Smits, V. D. Mihailetchi and P. W. M. Blom. Device model for the operation of polymer/fullerene bulk heterojunction solar cells. *Phys. Rev. B*, **72**, 085205 (2005). doi: 10.1103/PhysRevB.72.085205.

[114] G. A. Buxton and N. Clarke. Predicting structure and property relations in polymeric photovoltaic devices. *Phys. Rev. B*, **74**, 085207 (2006). doi: 10.1103/PhysRevB.74.085207.

[115] G. Li, V. Shrotriya, J. Huang, Y. Yao, T. Moriarty, K. Emery and Y. Yang. High-efficiency solution processable polymer photovoltaic cells by self-organization of polymer blends. *Nature Mater.*, **4**, 864 (2005). doi: 10.1038/nmat1500.

[116] T. Munters, T. Martens, L. Goris, V. Vrindts, J. Manca, L. Lutsen, W. De Ceuninck, D. Vanderzande, L. De Schepper, J. Gelan, N. S. Sariciftci and C. J. Brabec. A comparison between state-of-the-art 'gilch' and 'sulphinyl' synthesised MDMO-PPV/PCBM bulk hetero-junction solar cells. *Thin Solid Films*, **403-404**, 247 (2002). doi: 10.1016/S0040-6090(01)01562-0.

[117] R. A. Wessling and R. G. Zimmermann. U. S. Pats. 3, 401, 152 (1968).

[118] J. H. Burroughes, D. D. C. Bradley, A. R. Brown, R. N. Marks, K. Mackay, R. H. Friend, P. L. Burns and A. B. Holmes. Light-emitting diodes based on conjugated polymers. *Nature*, **347**, 539 (1990). doi: 10.1038/347539a0.

[119] S. Sensfuss and M. Al-Ibrahim. Optoelectronic properties of conjugated polymer/fullerene binary pairs with variety of LUMO level differences. In S.-S. Sun and N. S. Sariciftci, editors, *Organic Photovoltaics - Mechanisms, Materials, and Devices*. CRC Press, Boca Raton (2005).

[120] E. J. Meijer, D. M. de Leeuw, S. Setayesh, E. Van Veenendaal, B.-H. Huisman, P. W. M. Blom, J. C. Hummelen, U. Scherf and T. M. Klapwijk. Solution-processed ambipolar organic field-effect transistors and inverters. *Nature Mater.*, **2**, 678 (2003). doi: 10.1038/nmat978.

[121] Sigma-Aldrich. Poly[2-methoxy-5-(3',7'-dimethyloctyloxy)-1,4-phenylenevinylene]. URL: http://www.sigmaaldrich.com/catalog/product/aldrich/546461?lang=de&region=DE, date accessed: March 13th, 2013.

[122] B. C. Thompson and J. M. J. Fréchet. Polymer-fullerene composite solar cells. *Angew. Chem. Int. Ed.*, **47**, 58 (2008). doi: 10.1002/anie.200702506.

[123] M. Breselge, I. Van Severen, L. Lutsen, P. Adriaensens, J. Manca, D. Vanderzande and T. Cleij. Comparison of the electrical characteristics of four 2,5-substituted poly(*p*-phenylene vinylene) derivatives with different side chains. *Thin Solid Films*, **511-512**, 328 (2006). doi: 10.1016/j.tsf.2005.12.036.

[124] P. Peumans, A. Yakimov and S. R. Forrest. Small molecular weight organic thin-film photodetectors and solar cells. *J. Appl. Phys.*, **93**, 3693 (2003). doi: 10.1063/1.1534621.

[125] A. F. Hebard, R. C. Haddon, R. M. Fleming and A. R. Kortan. Deposition and characterization of fullerene films. *Appl. Phys. Lett.*, **59**, 2109 (1991). doi: 10.1063/1.106095.

[126] D. F. Kronholm and J. C. Hummelen. Fullerene-based acceptor materials. In C. Brabec, V. Dyakonov and U. Scherf, editors, *Organic Photovoltaics - Materials, Device Physics and Manufacturing Technologies*. Wiley-VCH, Weinheim (2008).

[127] N. Sivaraman, R. Dhamodaran, I. Kaliappan, T. G. Srinivasan, P. R. Vasudeva Rao and C. K. Mathews. Solubility of C_{60} in organic solvents. *J. Org. Chem.*, **57**, 6077 (1992). doi: 10.1021/jo00048a056.

[128] C. J. Brabec, N. S. Sariciftci and J. C. Hummelen. Plastic solar cells. *Adv. Funct. Mater.*, **11**, 15 (2001).

[129] V. D. Mihailetchi, J. K. J. van Duren, P. W. M. Blom, J. C. Hummelen, R. A. J. Janssen, J. M. Kroon, M. T. Rispens, W. J. H. Verhees and M. M. Wienk. Electron transport in a methanofullerene. *Adv. Funct. Mater.*, **13**, 43 (2003). doi: 10.1002/adfm.200390004.

[130] M. Lenes, G.-J. A. H. Wetzelaer, F. B. Kooistra, S. C. Veenstra, J. C. Hummelen and P. W. M. Blom. Fullerene bisadducts for enhanced open-circuit voltages and efficiencies in polymer solar cells. *Adv. Mater.*, **20**, 2116 (2008). doi: 10.1002/adma.200702438.

[131] K. Sugiyama, H. Ishii, Y. Ouchi and K. Seki. Dependence of indium-tin-oxide work function on surface cleaning method as studied by ultraviolet and x-ray photoemission spectroscopies. *J. Appl. Phys.*, **87**, 295 (2000). doi: 10.1063/1.371859.

[132] T. M. Brown, J. S. Kim, R. H. Friend, F. Cacialli, R. Daik and W. J. Feast. Built-in field electroabsorption spectroscopy of polymer light-emitting diodes incorporating a doped poly(3,4-ethylene dioxythiophene) hole injection layer. *Appl. Phys. Lett.*, **75**, 1679 (1999). doi: 10.1063/1.124789.

[133] A. M. Nardes, M. Kemerink, M. M. de Kok, E. Vinken, K. Maturova and R. A. J. Janssen. Conductivity, work function, and environmental stability of PEDOT:PSS thin films treated with sorbitol. *Org. Electron.*, **9**, 727 (2008). doi: 10.1016/j.orgel.2008.05.006.

[134] H. B. Michaelson. The work function of the elements and its periodicity. *J. Appl. Phys.*, **48**, 4729 (1977). doi: 10.1063/1.323539.

[135] R. Kersting, U. Lemmer, M. Deussen, H. J. Bakker, R. F. Mahrt, H. Kurz, V. I. Arkhipov, H. Bässler and E. O. Göbel. Ultrafast field-induced dissociation of excitons in conjugated polymers. *Phys. Rev. Lett.*, **73**, 1440 (1994). doi: 10.1103/PhysRevLett.73.1440.

[136] M. Deussen, M. Scheidler and H. Bässler. Electric field-induced photoluminescence quenching in thin-film light-emitting diodes based on poly(phenyl-*p*-phenylene vinylene). *Synth. Met.*, **73**, 123 (1995). doi: 10.1016/0379-6779(95)03307-6.

[137] D. Hertel, E. Vin Soh, H. Bässler and L. J. Rothberg. Electric field dependent generation of geminate electron-hole pairs in a ladder-type π-conjugated polymer probed by fluorescence quenching and delayed field collection of charge carriers. *Chem. Phys. Lett.*, **361**, 99 (2002). doi: 10.1016/S0009-2614(02)00898-9.

[138] S. Inal, M. Schubert, A. Sellinger and D. Neher. The relationship between the electric field-induced dissociation of charge transfer excitons and the photocurrent in small molecular/polymeric solar cells. *J. Phys. Chem. Lett.*, **1**, 982 (2010). doi: 10.1021/jz100121t.

[139] V. Singh, A. K. Thakur, S. S. Pandey, W. Takashima and K. Kaneto. Evidence of photoluminescence quenching in poly(3-hexylthiophene-2,5-diyl)

due to injected charge carriers. *Synth. Met.*, **158**, 283 (2008). doi: 10.1016/j.synthmet.2008.01.013.

[140] H. S. Majumdar, C. Botta, A. Bolognesi and A. J. Pal. Memory applications of a thiophene-based conjugated polymer by photoluminescence measurements. *Synth. Met.*, **148**, 175 (2005). doi: 10.1016/j.synthmet.2004.09.021.

[141] D. D. C. Bradley and R. H. Friend. Light-induced luminescence quenching in precursor-route poly(p-phenylene vinylene). *J. Phys.: Condens. Matter*, **1**, 3671 (1989). doi: 10.1088/0953-8984/1/23/011.

[142] Z. V. Vardeny and X. Wei. On the excitonic nature of the photoluminescence in polythiophene revealed by ODMR spectroscopy. *Mol. Cryst. Liq. Cryst.*, **256**, 465 (1994). doi: 10.1080/10587259408039277.

[143] J. Shinar. Trapped polarons, free polarons and triplet excitons in π-conjugated polymer films and light-emitting diodes. *Synth. Met.*, **78**, 277 (1996). doi: 10.1016/0379-6779(96)80150-0.

[144] D. K. Rout and S. C. Jain. Dielectric properties of a polymer-dispersed liquid crystal film. *Mol. Cryst. Liq. Cryst.*, **210**, 75 (1992). doi: 10.1080/10587259208030758.

[145] L. M. Clayton, A. K. Sikder, A. Kumar, M. Cinke, M. Meyyappan, T. G. Gerasimov and J. P. Harmon. Transparent poly(methyl methacrylate)/single-walled carbon nanotube (PMMA/SWNT) composite films with increased dielectric constants. *Adv. Funct. Mater.*, **15**, 101 (2005). doi: 10.1002/adfm.200305106.

[146] G. Porter. Flash photolysis and spectroscopy. A new method for the study of free radical reactions. *Proc. R. Soc. Lond. A*, **200**, 284 (1950). doi: 10.1098/rspa.1950.0018.

[147] T. H. Maiman. Stimulated optical radiation in ruby. *Nature*, **187**, 493 (1960). doi: 10.1038/187493a0.

[148] L. E. Hargrove, R. L. Fork and M. A. Pollack. Locking of He-Ne laser modes induced by synchronous intracavity modulation. *Appl. Phys. Lett.*, **5**, 4 (1964). doi: 10.1063/1.1754025.

[149] I. Montanari, A. F. Nogueira, J. Nelson, J. R. Durrant, C. Winder, M. A. Loi, N. S. Sariciftci and C. Brabec. Transient optical studies of charge recombination dynamics in a polymer/fullerene composite at room temperature. *Appl. Phys. Lett.*, **81**, 3001 (2002). doi: 10.1063/1.1512943.

[150] A. Kämpgen. Spectrally and temporally resolved photoinduced absorption in organic solar cells. Master thesis, Julius-Maximilians-Universität Würzburg (2011).

[151] W. Demtröder. *Experimentalphysik 2 - Elektrizität und Optik*. Springer-Verlag, Berlin Heidelberg, 5th edition (2009).

[152] J. R. Lakowicz. *Principles of fluorescence spectroscopy*. Springer Science+Business Media, New York, 3rd edition (2006).

[153] M. N. Liedtke. Spektroskopische Untersuchung neuartiger Fullerenakzeptoren für organische Solarzellen. Dissertation, Julius-Maximilians-Universität Würzburg (2011).

[154] C. Grünewald. Feldabhängige transiente Absorption an Polaronen in organischen Solarzellen. Diploma thesis, Julius-Maximilians-Universität Würzburg (2012).

[155] M. Gunz. Zeitaufgelöste photoinduzierte Absorption in organischen Solarzellen. Diploma thesis, Julius-Maximilians-Universität Würzburg (2010).

[156] S. Väth. Winkelaufgelöste Photolumineszenz detektierte Magnetresonanz an organischen Halbleitern. Diploma thesis, Julius-Maximilians-Universität Würzburg (2011).

[157] A. Sperlich. Electron paramagnetic resonance spectroscopy of fullerenes and conjugated polymers for organic photovoltaics. Dissertation, Julius-Maximilians-Universität Würzburg (2013).

[158] G. Binnig, C. F. Quate and C. Gerber. Atomic force microscope. *Phys. Rev. Lett.*, **56**, 930 (1986). doi: 10.1103/PhysRevLett.56.930.

[159] E. Zavoisky. Spin-magnetic resonance in paramagnetics. *J. Phys. USSR*, **9**, 211 (1945).

[160] Z. Shuai, J. L. Brédas and W. P. Su. Nature of photoexcitations in poly(paraphenylene vinylene) and its oligomers. *Chem. Phys. Lett.*, **228**, 301 (1994). doi: 10.1016/0009-2614(94)00961-9.

[161] R. N. Marks, J. J. M. Halls, D. D. C. Bradley, R. H. Friend and A. B. Holmes. The photovoltaic response in poly(*p*-phenylene vinylene) thin-film devices. *J. Phys.: Condens. Matter*, **6**, 1379 (1994). doi: 10.1088/0953-8984/6/7/009.

[162] J. L. Brédas, J. Cornil and A. J. Heeger. The exciton binding energy in luminescent conjugated polymers. *Adv. Mater.*, **8**, 447 (1996). doi: 10.1002/adma.19960080517.

[163] S. Barth and H. Bässler. Intrinsic photoconduction in PPV-type conjugated polymers. *Phys. Rev. Lett.*, **79**, 4445 (1997). doi: 10.1103/PhysRevLett.79.4445.

[164] G. Dennler, A. J. Mozer, G. Juška, A. Pivrikas, R. Österbacka, A. Fuchsbauer and N. S. Sariciftci. Charge carrier mobility and lifetime versus composition of conjugated polymer/fullerene bulk-heterojunction solar cells. *Org. Electron.*, **7**, 229 (2006). doi: 10.1016/j.orgel.2006.02.004.

[165] J. M. Warman, G. H. Gelinck and M. P. de Haas. The mobility and relaxation kinetics of charge carriers in molecular materials studied by means of pulse-radiolysis time-resolved microwave conductivity: dialkoxy-substituted phenylene-vinylene polymers. *J. Phys.: Condens. Matter*, **14**, 9935 (2002). doi: 10.1088/0953-8984/14/42/308.

[166] A. A. Bakulin, A. Rao, V. G. Pavelyev, P. H. M. van Loosdrecht, M. S. Pshenichnikov, D. Niedzialek, J. Cornil, D. Beljonne and R. H. Friend. The role of driving energy and delocalized states for charge separation in organic semiconductors. *Science*, **335**, 1340 (2012). doi: 10.1126/science.1217745.

[167] T. Martens, J. D'Haen, T. Munters, Z. Beelen, L. Goris, J. Manca, M. D'Olieslaeger, D. Vanderzande, L. De Schepper and R. Andriessen. Disclosure of the nanostructure of MDMO-PPV:PCBM bulk hetero-junction organic solar cells by a combination of SPM and TEM. *Synth. Met.*, **138**, 243 (2003). doi: 10.1016/S0379-6779(02)01311-5.

[168] H. Hoppe, M. Niggemann, C. Winder, J. Kraut, R. Hiesgen, A. Hinsch, D. Meissner and N. S. Sariciftci. Nanoscale morphology of conjugated polymer/fullerene-based bulk-heterojunction solar cells. *Adv. Funct. Mater.*, **14**, 1005 (2004). doi: 10.1002/adfm.200305026.

[169] W. R. Tinga, W. A. G. Voss and D. F. Blossey. Generalized approach to multiphase dielectric mixture theory. *J. Appl. Phys.*, **44**, 3897 (1973). doi: 10.1063/1.1662868.

[170] K. Asami. Characterization of heterogeneous systems by dielectric spectroscopy. *Prog. Polym. Sci.*, **27**, 1617 (2002). doi: 10.1016/S0079-6700(02)00015-1.

[171] O. H. Wiener. Die Theorie des Mischkörpers für das Feld der stationären Strömung. *Abh. Math. Phys. Kl. Akad. Wiss.*, B. G. Teubner, Leipzig (1912).

[172] Y. V. Serdyuk, A. D. Podoltsev and S. M. Gubanski. Numerical simulations of dielectric properties of composite material with periodic structure. *J. Electrostat.*, **63**, 1073 (2005). doi: 10.1016/j.elstat.2005.01.003.

[173] M. C. Scharber, N. A. Schultz, N. S. Sariciftci and C. J. Brabec. Optical- and photocurrent-detected magnetic resonance studies on conjugated polymer/fullerene composites. *Phys. Rev. B*, **67**, 085202 (2003). doi: 10.1103/PhysRevB.67.085202.

[174] L. S. Swanson, P. A. Lane, J. Shinar and F. Wudl. Polarons and triplet polaronic excitons in poly(paraphenylenevinylene) (PPV) and substituted PPV: An optically detected magnetic resonance study. *Phys. Rev. B*, **44**, 10617 (1991). doi: 10.1103/PhysRevB.44.10617.

[175] V. D. Mihailetchi, L. J. A. Koster, P. W. M. Blom, C. Melzer, B. de Boer, J. K. J. van Duren and R. A. J. Janssen. Compositional dependence of the performance of poly(*p*-phenylene vinylene):methanofullerene bulk-heterojunction solar cells. *Adv. Funct. Mater.*, **15**, 795 (2005). doi: 10.1002/adfm.200400345.

[176] A. Guerrero, L. F. Marchesi, P. P. Boix, J. Bisquert and G. Garcia-Belmonte. Recombination in organic bulk heterojunction solar cells: Small dependence of interfacial charge transfer kinetics on fullerene affinity. *J. Phys. Chem. Lett.*, **3**, 1386 (2012). doi: 10.1021/jz3003958.

[177] P. H. Wöbkenberg, D. D. C. Bradley, D. Kronholm, J. C. Hummelen, D. M. de Leeuw, M. Cölle and T. D. Anthopoulos. High mobility n-channel organic field-effect transistors based on soluble C_{60} and C_{70} fullerene derivatives. *Synth. Met.*, **158**, 468 (2008). doi: 10.1016/j.synthmet.2008.03.016.

[178] J. Schafferhans, C. Deibel and V. Dyakonov. Electronic trap states in methanofullerenes. *Adv. Energy Mater.*, **1**, 655 (2011). doi: 10.1002/aenm.201100175.

[179] G.-J. A. H. Wetzelaer, M. Kuik and P. W. M. Blom. Identifying the nature of charge recombination in organic solar cells from charge-transfer state electroluminescence. *Adv. Energy Mater.*, **2**, 1232 (2012). doi: 10.1002/aenm.201200009.

A Nomenclature

Abbreviations

a-Si	amorphous silicon
AFM	atomic force microscopy
BHJ	bulk heterojunction
bisPCBM	bisadduct analogue of $PC_{61}BM$
c-Si	monocrystalline silicon
CIGS	copper indium gallium (di)selenide
CSS	charge separated state
CT	charge transfer
CTE	charge transfer exciton / charge transfer excitons
CTS	charge transfer state / charge transfer states
cw	continuous wave
diPEO-PPV	poly(2,5-bis-(triethoxymethoxy)-1,4-phenylene vinylene)
DOS	density of states
DPSS	diode pumped solid state
EEG	Erneuerbare-Energien-Gesetz
EL	electroluminescence
ESR	electron spin resonance
F	electric field
FWHM	full-width half-maximum
HOMO	highest occupied molecular orbital
ITO	indium tin oxide
IV	current–voltage
LUMO	lowest unoccupied molecular orbital
mc-Si	microcrystalline silicon
MDMO-PPV	poly[2-methoxy-5-(3',7'-dimethyloctyloxy)-1,4-phenylenevinylene]
MPP	maximum power point
nc-Si	nanocrystalline silicon
ND	neutral density

Nd:YAG	neodymium-doped yttrium aluminum garnet
ODMR	optically detected magnetic resonance
OFET	organic field effect transistor
OLED	organic light emitting diode
OPV	organic photovoltaics
P3HT	poly(3-hexylthiophene)
$PC_{61}BM$	[6,6]-phenyl-C61 butyric acid methyl ester
$PC_{71}BM$	[6,6]-phenyl-C71 butyric acid methyl ester
PCBM	referring to different C_{60} based fullerene derivatives without further specification
PCPDTBT	poly[2,1,3-benzothiadiazole-4,7-diyl[4,4-bis(2-ethylhexyl)-4H-cyclopenta[2,1-b:3,4-b']dithiophene-2,6-diyl]]
PEDOT:PSS	poly(3,4-ethylenedioxythiophene):poly(styrenesulfonate)
PEO-PPV	poly[2-methoxy-5-(triethoxymethoxy)-1,4-phenylene vinylene]
photo-CELIV	photoinduced charge extraction by linearly increasing voltage
PIA	photoinduced absorption
PL	photoluminescence
PL(F)	field dependent photoluminescence
PLDMR	photoluminescence detected magnetic resonance
PMMA	poly(methyl methacrylate)
PP	polaron pair
PPV	poly(p-phenylene vinylene)
PV	photovoltaics
S_0	ground state (of the singlet exciton)
S_1	first excited state of the singlet exciton, also used in lieu of the term "singlet exciton"
SMU	source-measure unit
SNR	signal-to-noise-ratio
T_1	first excited state of the triplet exciton
TA	transient absorption
TA(F)	field dependent transient absorption
TCO	transparent conductive oxide
TOF	time-of-flight
TRMC	time-resolved microwave conductivity
TSC	thermally stimulated current

Variables

a	thermalization length, electron–hole distance
α	absorption coefficient
d	optical path length
	also: active layer thickness
D	zero field interaction parameter
e	elementary charge
E_b	binding energy
$E_{g,opt}$	optical bandgap
E_{pot}	potential energy
E_t	trap activation energy
ϵ_0	dielectric constant in vacuum
ϵ_r	relative dielectric constant
η	power conversion efficiency
f	volume fraction
F	electric field
FF	fill factor
γ	Langevin recombination factor
I	intensity
I_{MPP}	current at the MPP
I_{sc}	short circuit current
j_{sc}	short circuit current density
k_{cs}	charge separation rate
$k_d(F)$	field dependent dissociation rate
k_f	recombination rate of the CTS or the singlet exciton
k_r	recombination rate of the CSS or PP
k_{th}	thermalization rate
kT	thermal energy
λ	wavelength
m_s	spin quantum number
μ	mobility
$\mu\tau$	mobility–lifetime product
n	charge carrier density
n_t	trap density
OD	optical density
P_L	power of the incident light
$P(F)$	field dependent dissociation probability

Φ	work function
PL	PL intensity
q	charge
Q	field dependent PL quenching
r_c	Coulomb capture radius
S	spin
σ	absorption cross section
	also: energetic width of the DOS reflecting the disorder
T	temperature
	also: transmittance
τ	lifetime
v	charge carrier drift velocity
V	voltage
V_{MPP}	voltage at the MPP
V_{oc}	open circuit voltage

B Publications and Conference Contributions

Full Papers in Review Journals

1. **J. Kern**, H. Kraus, C. Grünewald, F. Fuchs, C. Deibel and V. Dyakonov. Field dependent charge carrier photogeneration via charge transfer states in organic bulk heterojunction solar cells: The interplay between morphology and dielectric constant. *In preparation* (2013).

2. H. Kraus, S. Väth, **J. Kern**, A. Förtig, A. Sperlich, C. Deibel and V. Dyakonov. Triplet excitons in high-efficiency organic solar cell materials. *In preparation* (2013).

3. **J. Kern**, S. Feldman, I. Kim, G. Dyer, B. I. Cho, A. C. Bernstein and T. Ditmire. Simultaneous imaging of K-α radiation and coherent transition radiation from relativistic-intensity laser-irradiated solid target plasmas. *High Energy Density Phys.*, **8**, 60 (2012). doi: 10.1016/j.hedp.2011.11.009.

4. **J. Kern**, S. Schwab, C. Deibel and V. Dyakonov. Binding energy of singlet excitons and charge transfer complexes in MDMO-PPV:PCBM solar cells. *Phys. Stat. Sol. RRL*, **5**, 364 (2011). doi: 10.1002/pssr.201105430.

5. A. Sperlich, M. Liedtke, **J. Kern**, H. Kraus, C. Deibel, S. Filippone, J. L. Delgado and V. Dyakonov. Photoinduced C70 radical anions in polymer:fullerene blends. *Phys. Stat. Sol. RRL*, **5**, 128 (2011). doi: 10.1002/pssr.201105030.

Contributed Talks

1. **J. Kern**, M. Mingebach, C. Grünewald, C. Deibel and V. Dyakonov. Field dependence of charge carrier generation in conjugated polymer–fullerene solar cells. *International Conference on Science and Technology of Synthetic Metals (ICSM)*, Atlanta (2012).

2. **J. Kern**, J. Rauh, C. Grünewald, C. Deibel and V. Dyakonov. Field dependence of charge carrier generation in MDMO-PPV based organic solar cells. *DPG-Frühjahrstagung*, Berlin (2012).

3. **J. Kern**, S. Schwab, C. Deibel and V. Dyakonov. Investigation of charge transfer states in MDMO-PPV:PCBM solar cells. *DPG-Frühjahrstagung*, Dresden (2011).

Poster Presentations

1. **J. Kern**, H. Kraus, F. Fuchs, C. Grünewald, C. Deibel and V. Dyakonov. Field dependent charge carrier generation via CT states: Escaping the Coulomb potential. *DPG-Frühjahrstagung*, Regensburg (2013).

2. **J. Kern**, C. Grünewald, H. Kraus, F. Fuchs, C. Deibel and V. Dyakonov. Field dependent charge carrier generation via CT states: A blending ratio dependent study. *DFG-Schwerpunktprogramm 1355, Doktorandenworkshop*, Würzburg (2012).

3. M. Mingebach, **J. Kern**, S. Walter, S. Schwab, A. Wagenpfahl, C. Deibel and V. Dyakonov. Pulsed photocurrent and field dependent photoluminescence measurements. *Fundamentale Funktionsweise organischer Solarzellen - Interdisziplinärer Workshop der Bayerischen Akademie der Wissenschaften*, München (2011).

4. **J. Kern**, H. Kraus, C. Deibel and V. Dyakonov. Investigation of charge transfer states in MDMO-PPV:PCBM solar cells. *Plastic Electronics*, Dresden (2010).

5. **J. Kern**, M. Binder, H. Kraus, C. Deibel and V. Dyakonov. Charge transfer state electroluminescence in MDMO-PPV:$PC_{61}BM$ solar cells. *DPG-Frühjahrstagung*, Regensburg (2010).

Supervised Diploma Theses

1. C. Grünewald. Feldabhängige transiente Absorption an Polaronen in organischen Solarzellen. Diploma thesis, Julius-Maximilians-Universität Würzburg (2012).

2. S. Schwab. Exciton and charge transfer complex binding energies of organic systems. Diploma thesis, Julius-Maximilians-Universität Würzburg (2011).

C Acknowledgments

There are many many people who supported me during my time at EPVI and the time afterwards while I was writing this thesis. Without them, this work would not have been possible — or at least not as great an experience and as much fun as it was.

First of all, my utmost thanks go to Prof. Dr. Vladimir Dyakonov for giving me the opportunity of working at his chair and writing the presented thesis. His frequent and often unexpected questions and remarks while discussing conference contributions and publications in preparation helped me to continuously reconsider my results and to gain valuable new insights. Thanks for that!

Also, I am very grateful to PD Dr. Carsten Deibel for supervising my work. With his 24/7-support, his many suggestions and critical reviews, he was an esteemed teacher and mentor to me who contributed greatly to my professional and personal development.

I'd also like to thank Prof. Dr. Jean Geurts for his kind readiness to read and evaluate this thesis.

Coming to speak of my team members at EPVI, I first of all have to say a thousand thanks to Hannes Kraus. He was not only a great partner in the lab who was always willing to give a hand and support me with all kinds of experimental, technical and IT issues, but he has also become one of my closest and most sincere friends. Thank you so much for your help, the nerdy comments and the delicious Hörnchen!

Also, many thanks go to the other members of the photophysics group: Dr. Andreas „Hex" Sperlich, Franziska „Franzi" Fuchs, Stefan „Väthi" Väth, Björn „Börni" Gieseking, Andreas „Fritzi" Fritze, Dr. Moritz Liedtke and all of the current and former diploma and master students of the death star lab. It was a pleasure working with you guys! In particular, I owe a lot to Hex for IT support and for sharing his astonishing expertise with me, and I am happy to have found such a reliable friend in Franzi.

My time outside the lab was greatly improved by my dear office mates and friends Andreas „Zusi" Zusan and Väthi, with short visits from our beloved Jasmin. Thanks for the many professional and nonsense discussions, the fun afterwork activities and the willingness to play Wizard with me again and again. I already miss you and your white-

board messages! Thanks a lot as well to my other former office mates, including my favorite French guy Julien Gorenflot and my fellow student Matthias „Gonzo“ Gunz.
I'd also like to thank my former diploma students Sebastian Schwab and Clemens Grünewald for the great work they did.
Of course, many thanks go to the whole group of EPVI. Just to name some, I'd like to thank Dr. Andreas Baumann, Alexander Förtig, Dr. Markus Mingebach and Dr. Julia Rauh for their support, the inspiring discussions and the great time. Thanks to Christian Weber for the relaxing English tea breaks and the Tischkicker matches. Thanks to the „Pflaumis“ (especially to Andreas Steindamm and Nis Hauke Hansen) for providing us with a Tischkicker table and for the delightful conversations. Thanks to Diep Phan for the help with every non-scientific concern. Thanks to Valentin Baianov for the great optical solutions in the lab, and thanks to André Thiem-Riebe for keeping everything in the labs going.
Apart from my EPVI peers, I want to say thank you to my long-time friends Monika Väth and Johannes Wenz. Thanks for always being there for me when I needed you or just wanted to have a good time; this also contributed to my finishing this thesis!
Finally, I want to express my deepest and heartfelt gratitude to the two most important people in my life – my wonderful parents Rosemarie and Rainer. Danke, dass ihr immer an mich glaubt und mich nach wie vor bei allen meinen Plänen und Aktivitäten auf jede nur denkbare Weise unterstützt!

Funding

The presented work was supported by the Bundesministerium für Bildung und Forschung in the framework of the GREKOS project (contract no. 03SF0356B).

D Curriculum Vitae